

Phase space eigenfunctions with applications to continuum kinetic simulations

Daniel W. Crews^{1,†} and Uri Shumlak^{1,2}

¹Zap Energy Inc., Everett, WA 98203, USA

²Aerospace and Energetics Research Program, University of Washington, Seattle, WA 98195-2400, USA

(Received 23 January 2024; revised 19 June 2024; accepted 10 July 2024)

Continuum kinetic simulations are increasingly capable of resolving high-dimensional phase space with advances in computing. These capabilities can be more fully explored by using linear kinetic theory to initialize the self-consistent field and phase space perturbations of kinetic instabilities. The phase space perturbation of a kinetic eigenfunction in unmagnetized plasma has a simple analytic form, and in magnetized plasma may be well approximated by truncation of a cyclotron-harmonic expansion. We catalogue the most common use cases with a historical discussion of kinetic eigenfunctions and by conducting nonlinear Vlasov–Poisson and Vlasov–Maxwell simulations of singlemode and multimode two-stream, loss-cone and Weibel instabilities in unmagnetized and magnetized plasmas with one- and two-dimensional geometries. Applications to quasilinear kinetic theory are discussed and applied to the bump-on-tail instability. In order to compute eigenvalues we present novel representations of the dielectric function for ring distributions in magnetized plasmas with power series, hypergeometric and trigonometric integral forms. Eigenfunction phase space fluctuations are visualized for prototypical cases such as the Bernstein modes to build intuition. In addition, phase portraits are presented for the magnetic well associated with nonlinear saturation of the Weibel instability, distinguishing current-density-generating trapping structures from charge-density-generating ones.

Key words: plasma instabilities, plasma simulation, plasma waves

1. Introduction

Kinetic equations describe fundamental dynamics in collisionless plasma, so their linear analysis and nonlinear simulation is a perennial topic (Bertrand & Feix 1968; Cheng & Knorr 1976; Birdsall & Langdon 1991; Heath *et al.* 2012; Morrison 2017). Plasma kinetic theory and non-equilibrium thermodynamics are closely connected, and the basic problem in collisionless kinetic theory is to describe the stability of a distribution to collective perturbations (Penrose 1960). In the simplest, spatially homogeneous plasmas instability modes arise from non-thermal distributions due to streaming, anisotropic pressure

† Email address for correspondence: daniel.crews@zap.energy

(Weibel 1959), loss-cones (Rosenbluth & Post 1965), etc. Put simply, these instabilities arise from entropically unfavourable distributions of relative velocity. Historically, kinetic instabilities have been a key part of transport theory in collisionless plasma (Drummond & Rosenbluth 1962; Yoon & Lui 2006), and kinetic simulations of instability have contributed to advances in dynamical sciences (Escande 2016) and modelling for fluid closures (Conner & Wilson 1994). The intrinsic complexity of phase space turbulence arising from kinetic instabilities has made nonlinear simulation key to the construction of more comprehensive models, and a huge potential remains for kinetic simulations to enrich plasma theory as advances in technique and computing power overcome the curse of dimensionality (He *et al.* 2016; Choi, Christlieb & Wang 2021).

We begin by stating the purpose of this work and its context in the existing literature, by clarifying commonly used terms here and by listing which codes may benefit from the described techniques. This work reviews eigenfunction solutions to the linearized plasma kinetic equations, here also referred to as ‘self-consistent plasma-field configurations’ or ‘kinetic eigenfunctions’, and discusses how these kinetic eigenfunctions can be utilized to cleanly initialize kinetic instabilities simulated by the continuum kinetic method. Here ‘continuum kinetic method’ means that the kinetic equation is solved by an Eulerian method in the phase space, for example the finite element method (Heath *et al.* 2012), in contrast to the particle-in-cell method. The phase space configuration corresponding to the kinetic eigenfunction will be referred to as a ‘phase space eigenfunction’. Then, having reviewed the basic theory and discussed the benefits of eigenfunction initialization, the method is illustrated with model problems of streaming, pressure anisotropy and loss-cone cyclotron instabilities. Commentary on the instability physics is made throughout and some novel results are noted. A summary is made of novel results in the conclusion.

Historically, phase space eigenfunctions have been utilized in the space physics community for analysis of collisionless energy transfer, for example in the role played by kinetic slow modes in the solar wind (Verscharen *et al.* 2016; Verscharen, Chen & Wicks 2017) or by phase space perturbations in Alfvénic turbulence (Wu *et al.* 2019; Zhao *et al.* 2022). In the realm of simulation, the major continuum fusion gyrokinetic codes (GENE, GS2, GYRO/CGYRO) all have a kinetic eigenfunction initialization capability regularly employed in studies of astrophysical and laboratory fusion plasmas (Howes *et al.* 2006, 2011; Watanabe *et al.* 2014; Verniero, Howes & Klein 2018). On the other hand, codes solving the unreduced kinetic models (Vlasov–Poisson or Vlasov–Maxwell) with continuum kinetic method appear, to the best of our knowledge, not to utilize kinetic eigenfunctions. The methodology advocated for in this work should be applicable and beneficial for all continuum kinetic codes, such as HVM (Valentini *et al.* 2007), Vlasiator (Kempf *et al.* 2013; Palmroth *et al.* 2018), Gkeyll (Juno *et al.* 2018; Hakim & Juno 2020), ViDA (Pezzi *et al.* 2019), the Lawrence Livermore Vlasov–Poisson code (Vogman, Shumlak & Colella 2018), the Ruhr University Vlasov code (Allmann-Rahn, Lautenbach & Grauer 2022), WARPXM (Shumlak *et al.* 2011; Datta & Shumlak 2023) and the Los Alamos spectral Vlasov solver (Vencels *et al.* 2016; Roytershteyn & Delzanno 2018). Eigenfunctions of the unreduced kinetic equations are analytically tractable in many situations of interest, for example the unmagnetized (streaming) or magnetized (loss-cone) electrostatic instabilities and the electromagnetic unmagnetized (Weibel) or magnetized (field-parallel whistler) pressure anisotropy instabilities. Of these examples, the whistler is not treated in this work.

Kinetic eigenfunctions consist of structure in both the field and the phase space self-consistently. It is fairly common practice to initialize simulations using only the field-part of the eigenfunctions but without the corresponding phase space configuration, with field sources obtained by spatial moments of a Maxwellian distribution

(Vásconez *et al.* 2014; Ng *et al.* 2019). For example, to achieve density perturbations $n_1/n_0 = A \sin(kx)$ the equilibrium distribution function f_0 is perturbed as $f_1(x, v) = A \sin(kx)f_0(v)$. Indeed, linear modes (namely, self-consistent plasma-field configurations) have a phase space structure more like $f_1(x, v) = (\zeta - v)^{-1} \partial_v f_0 e^{ikx}$ with $\zeta = \omega/k$ a complex phase velocity, and so a significant portion of the perturbation energy is channelled into the Landau-damped modes and the model's energy trace begins by a transient energetic reorganization via Landau damping. The consequence is that spatial moment-based perturbations partition perturbation energy in a manner different from what the researcher may have intended. The partition of energy into non-eigenfunction perturbations is not harmful to the intended solution when initial amplitudes are small, but at larger perturbation amplitudes Landau damping may non-physically contribute to nonlinear phenomena as these modes are usually activated by thermal fluctuations. There is an additional numerical consideration of perturbations with both growing and damped components, in which case precise measurement of growth rates is obscured by Landau damping.

To recapitulate, the numerical and theoretical methods and results presented here should be beneficial for those conducting continuum kinetic simulations, including researchers utilizing the major codes listed above, those investigating new numerical methods for kinetic equations (Einkemmer 2019) and for problems considered with smaller targeted codes (Crews & Shumlak 2022; Paul & Sharma 2024). The methods presented here apply most directly to approaches where the perturbed distribution may be functionally specified. This is the case in most continuum kinetic numerical methods, such as in our work where we use a mixed Fourier spectral–finite element method discussed in [Appendix A](#), with some variations noted throughout the applications. However, it seems to the authors that sophisticated particle-in-cell methods (Kraus *et al.* 2017; Glasser & Qin 2020; Barnes & Chacón 2021; Perse, Kormann & Sonnendrücker 2021) can utilize these results as well.

This article is organized as theory followed by simulation, treating progressively the unmagnetized and magnetized electrostatic and unmagnetized electromagnetic problems. Section 2 reviews unmagnetized electrostatic phase space eigenfunctions and Landau modes, including a historical summary, a review of the initial-value problem and an energetic analysis. The difference between kinetic eigenfunctions and Landau damping modes is discussed, with only unstable perturbations resulting in genuine eigenfunctions. Section 2.8 notes the importance of kinetic eigenfunctions in quasilinear theory (QLT). Section 3 then discusses the electrostatic cyclotron modes, making new connections to the theory of special functions through hypergeometric functions and the Laguerre polynomials in the dielectric tensor of loss cones, and explores the helical phase space structure of Bernstein modes. Section 4 considers the vector eigenmodes of the Vlasov–Maxwell system by casting the dielectric tensor as an eigenvalue problem for a system of integral equations and presents a practical method to calculate them. The natural consistency of the plasma-field configuration resulting from this method is observed as a benefit, so that the initial condition automatically satisfies Poisson's equation, for example. The distinction between phase space eigenfunctions and Landau damping modes is generalized to the vector case, and the one-dimensional and two-dimensional Weibel instabilities are explored for the anisotropic Maxwellian distribution.

Illustrative simulations are presented in the relevant sections and include the multidimensional multimode two-stream instability in § 2.7, single-mode Dory–Guest–Harris instability in § 3.6, single-mode Weibel instability in § 4.4 and multidimensional multimode Weibel problem in § 4.5. Commentary is provided throughout on the physics of these problems as nonlinear structures evolve from the initialized linear eigenfunctions. The general numerical method is described in [Appendix A](#) and problem-specific

modifications are noted for each problem prior to initialization specifics. The magnetized electromagnetic problem is not treated here, but we mention that the analytic kinetic eigenfunctions are fairly simple, as parallel-field whistler modes, for example, involve only the first cyclotron harmonic. The linear theory for whistler emission can be found in Gurnett & Bhattacharjee (2017, p. 415), and the eigenfunction is briefly described in Chapter 7 of Crews (2022).

2. Electrostatic plasma modes with zero-order ballistic trajectories

Perhaps the simplest problem in plasma kinetic theory is that of electrostatic modes in unmagnetized homogeneous plasma, meaning that the zero-order orbits are simply free streaming ballistic motions. Here the problem is treated beginning with a historical discussion, followed by analysis of the initial-value problem, and an energetic analysis of response to eigenfunction and non-eigenfunction phase space perturbations. Recall that there are two ways of considering the linearized dynamics: the eigenvalue problem ($t \in (-\infty, \infty)$) and the initial-value problem ($t \in [0, \infty)$). A somewhat subtle theoretical point is the distinction between eigenfunctions and Landau-damped modes; to clarify this distinction requires a review of the Case–van Kampen modes and the theory of linear Landau damping, which can be found in Crews (2022) and is omitted here for brevity. Nevertheless, in the following the distinction is reviewed at a qualitative level.

2.1. Historical summary and context

The study of eigenfunctions of collisionless and collisional plasma kinetic equations has a long history. Vlasov was the first to suggest a method to estimate the plasma oscillation frequencies by prescribing that the principal value be taken at the resonant velocity in the dispersion function. Following this, Bohm & Gross (1949) side-stepped the resonant term by considering high-enough phase velocities that the distribution function was effectively zero at the pole. Famously, Landau (1946) formally solved the linearized initial-value problem for Vlasov–Poisson dynamics using a Laplace transformation, discovering a discrete set of solutions for the Maxwellian plasma, wherein the electric potential damped in time. This collisionless decay phenomenon is called Landau damping. For the collisionless plasma the decaying Landau modes are not eigenfunctions, meaning that such solutions cannot evolve independently. Yet Landau’s analysis also found unstable modes for certain distributions f_0 . Thus, despite both unstable and dissipative modes sharing a similar phase space structure like $(v - \zeta)^{-1} \partial_v f_0 e^{ikx}$, unstable modes evolve as a single analytic function while dissipation spreads across the entire Landau spectrum.

As the eigenvalue problem remained unsolved, Van Kampen (1955) and Case (1959) formally solved the problem and determined the spectrum of the linearized kinetic equation to be continuous with a possibly discrete component. Discrete eigenvalues arise only for unstable modes where $\text{Im}(\omega) > 0$. The continuous part of the spectrum consists of ballistic modes in the form $\varepsilon(k, \zeta) \delta(v - \zeta)$, while the discrete part is in the analytic form $(v - \zeta)^{-1} \partial_v f_0$. Here $\varepsilon(k, \zeta)$ is the dielectric function and $f_0(v)$ the homogeneous equilibrium. The discrete part of the Case–van Kampen spectrum is identical to Landau’s unstable modes. Landau’s damping modes are represented as an integral expansion over the continuous Case–van Kampen spectrum. As a complete orthogonal system the Case–van Kampen modes are a useful though under-utilized tool. An insightful application was accomplished by P.J. Morrison and colleagues in constructing a linear integral transform, termed a ‘G transform’, to reduce the linearized Vlasov equation to an advection problem by utilizing the Case–van Kampen modes as a basis (Morrison & Pfirsch 1992; Morrison 2000; Heninger & Morrison 2018).

As the Landau damping modes are not collisionless eigenfunctions their status has remained somewhat obscure. Light is shed on this problem by considering weak dissipation in the Vlasov equation, such as the collision operator of Lenard & Bernstein (1958). The landmark studies of Ng, Bhattacharjee & Skiff (1999) and Short & Simon (2002) have shown that as dissipation tends to zero the dissipative eigenfunctions converge to the Landau damping modes, with the conclusion that dissipation is a singular perturbation of the collisionless dynamics. Bratanov *et al.* (2013) numerically confirmed this limit for discrete systems and Ng, Bhattacharjee & Skiff (2004) extended and formalized the results for weakly collisional plasma. However, the authors wish to highlight here that the Case–van Kampen modes still play a role in the dissipative picture. Namely, one can show (Bratanov *et al.* 2013; Crews 2022) that the propagator of the linearized kinetic equation with the Lenard–Bernstein operator limits to the Case–van Kampen modes as the dissipation $\nu \rightarrow 0^+$. This fact clarifies the relationship between the continuous Case–van Kampen spectrum and Landau damping modes, as even in the dissipative picture the Landau modes are represented as an integral over the diffusive propagator, and the collisionless Case–van Kampen modes indeed play the role of non-diffusive propagators (Balescu 1997). To understand why Landau modes are easily identified in the initial-value problem, consider that Landau damping originates from phase mixing (Mouhot & Villani 2011) and so the modes possess the peculiar property of decaying in both directions of time. Thus, they arise by propagating initial data, or otherwise must be represented as an interference of free streaming modes unmixing from $t \in (-\infty, 0)$ and remixing from $t \in (0, \infty)$.

In summary, in collisionless plasma kinetic theory unstable modes are normal modes and evolve independently, while dissipative modes either occur as a summation of non-orthogonal transient modes or must be represented in the Case–van Kampen spectrum. The Case–van Kampen spectrum has found fruitful application as the basis of constructing an integral transform theory for linearized dynamics, most recently explored in Heninger & Morrison (2018). In weakly collisional dynamics dissipative modes are also eigenfunctions and limit to the collisionless Landau mode spectrum as dissipation tends to zero. As a consequence, it is possible to excite a single-mode instability by initializing its eigenfunction, but one may not excite a lone Landau-damping plane wave under collisionless dynamics. The following discussion illustrates this point.

2.2. Phase space linear response and the dielectric function

The electric susceptibility χ is the linear response function which relates in the spatiotemporal frequency domain $(\mathbf{x}, t) \rightarrow (\mathbf{k}, \omega)$ the polarization $\tilde{\mathbf{P}}(\mathbf{k}, \omega)$ and electric field $\tilde{\mathbf{E}}(\mathbf{k}, \omega)$ by the constitutive relation $\tilde{\mathbf{P}} = \varepsilon_0 \chi \tilde{\mathbf{E}}$. In the scheme of electrostatic theory one aims to determine the susceptibility and consequently the dielectric permittivity $\varepsilon(\mathbf{k}, \omega) = \varepsilon_0(1 + \chi)$ of a plasma with equilibrium distribution $f_0(\mathbf{v})$. The susceptibility is determined through the self-consistent particle response $f_1(\mathbf{k}, \mathbf{v}, \omega)$ such that $f = f_0 + f_1$, leading to the sought-after modal structures in the charge density. The distribution f_1 encodes a linear response of the charges to the electric potential φ according to the relation $f_1 = h(\mathbf{k}, \mathbf{v}, \omega)\varphi$ for some response function h . For this reason, we mean by ‘phase space linear response function’ the self-consistent particle response f_1 to the potential φ . The permittivity is often referred to as simply the dielectric function because the permittivity tensor reduces to a scalar for isotropic equilibria.

The following review of the initial-value problem is done in detail for the simplest case in order to build intuition for the electromagnetic and magnetized problems where

propagation of the initial data is tedious.¹ Using the results, we then consider the evolution of perturbations in a plasma with Maxwellian f_0 , namely a so-called Maxwellian perturbation (that is, where $f_1(x, v) = A \sin(kx)f_0(v)$) and a special perturbation describing a propagating, damping plane wave. When this plane wave is unstable the special perturbation grows as an eigenmode, i.e. a constant phase space structure with time-dependent amplitude, and when damped its structure evolves in phase space.

Rather than the usual Laplace transform notation, we use a more standard notation for the one-sided temporal Fourier transform pair as

$$f(\omega) = \int_0^\infty f(t)e^{i\omega t} dt, \quad (2.1)$$

$$f(t) = \frac{1}{2\pi} \int_{-\infty+is}^{\infty+is} f(\omega)e^{-i\omega t} d\omega, \quad (2.2)$$

where the factor s keeps the contour above all poles of the integrand in order that (2.1) converges. The contour in (2.2) is closed at infinity around the lower half-plane, and the inverse transform is then given by the residue theorem as

$$f(t) = -i \sum \text{Res}(f(\omega)) \quad (2.3)$$

with the sum over all poles of the response function $f(\omega)$. The spatial Fourier transform $x \rightarrow k$ is defined as usual over all of space by $f(k) = \int dx e^{-ik \cdot x} f(x)$. We consider for simplicity the response of a single species of particle charge q and mass m amidst a uniform neutralizing Maxwellian background, so we do not write a species subscript.

The Vlasov–Poisson system linearized by $f(x, v, t) = f_0 + f_1$ with $f_1 \ll f_0$ is given by

$$\frac{\partial f_1}{\partial t} + \mathbf{v} \cdot \nabla f_1 - \frac{q}{m} (\nabla_x \varphi) \cdot \nabla_v f_0 = 0, \quad (2.4)$$

$$\nabla^2 \varphi = -\frac{qn_0}{\varepsilon_0} \int f_1 dv. \quad (2.5)$$

Fourier transforming for all of space and for time $t \in (0, \infty)$ as described, the phase space linear response is obtained as

$$f_1(\mathbf{k}, \mathbf{v}, \omega) = i \frac{g(\mathbf{k}, v)}{\omega - \mathbf{k} \cdot \mathbf{v}} - \frac{q}{m} \varphi \frac{\mathbf{k} \cdot \nabla_v f_0}{\omega - \mathbf{k} \cdot \mathbf{v}}, \quad (2.6)$$

where $g(\mathbf{k}, v) = f_1(t=0, \mathbf{k}, v)$ is the initial condition.

The following result is as described in Landau (1946) with some change in notation. Define the Cauchy integral $g^*(\mathbf{k}, \zeta) \equiv \int_{\mathcal{C}} (g(\mathbf{k}, v)/(\zeta - v)) dv$, with \mathcal{C} Landau's contour (that is, analytically continued into the lower-half ζ -plane). Choose the coordinates such that one axis aligns with the wavevector \mathbf{k} , so that when computing the zeroth velocity moment of f_1 , two of the velocity coordinates integrate out. The potential is found to be

$$\varphi(\mathbf{k}, \zeta) = i \frac{\sigma}{k^3} \frac{g^*(\mathbf{k}, \zeta)}{\varepsilon(\mathbf{k}, \zeta)}, \quad (2.7)$$

where $\sigma = q/|q|$ and $\varepsilon(\mathbf{k}, \zeta) = 1 + k^{-2} \int_{\mathcal{C}} (1/(\zeta - v)) (\partial f_0 / \partial v) dv$ is the electrostatic dielectric function. Here the wavenumber k is normalized to the Debye length. If each

¹The following analysis applies quasianalysis, which considers the eigenvalue problem and analytically continues the dispersion function from the upper-half to the lower-half complex frequency plane. The analysis does not consider damped modes to be eigenfunctions.

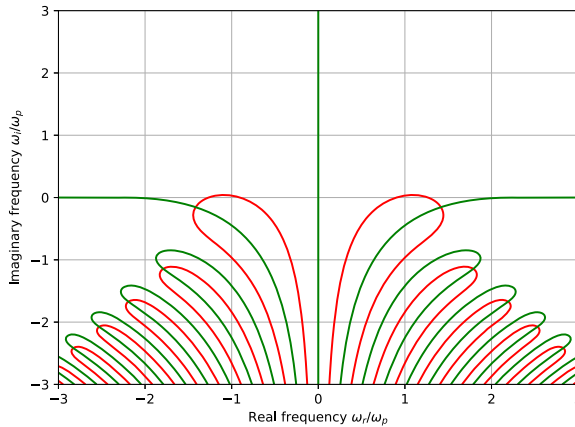


FIGURE 1. Locations of solutions to $\varepsilon(k, \omega) = 0$ showing contours of $\text{Re}(\varepsilon) = 0$ in red and $\text{Im}(\varepsilon) = 0$ in green for a Maxwellian $f_0(v)$ at short wavelength, $k\lambda_D = 0.5$. Solutions to $\varepsilon(k, \omega) = 0$ occur at the intersection of the real and imaginary zero-contours. These damped modes represent the transient Landau spectrum which accompanies any simulation of kinetic instability not initialized with an eigenfunction.

root ζ_j of $\varepsilon(k, \zeta) = 0$ is simple and $g^*(k, \zeta)$ has no poles then inverse transforming in time gives

$$\varphi(k, t) = \frac{\sigma}{k^3} \sum_j \frac{g^*(k, \zeta_j)}{\varepsilon_\omega(k, \zeta_j)} e^{-i\omega_j t} \quad (2.8)$$

with $\varepsilon_\omega \equiv \partial\varepsilon/\partial\omega$. Figure 1 shows the typical locations of the infinite set of zeros $\varepsilon(k, \omega) = 0$ in the lower-half frequency plane making up the Landau damping mode spectrum. The amplitude of each mode ζ_j is given by the Cauchy integral of the initial perturbation weighted by that mode's factor ε_ω^{-1} . For example, a typical perturbation used in numerical simulations is Maxwellian in velocity space, namely $g(v) = (\sqrt{\pi}v_t)^{-1}e^{-v^2/v_t^2}$. In this case our Cauchy integral is $g^*(\zeta) = v_t^{-1}Z(\zeta/v_t)$ with $Z(\zeta)$ the plasma dispersion function defined by Fried & Conte (1961). Normalizing phase velocity to v_t , the self-consistent electric potential response for the Maxwellian perturbation is

$$\varphi(k, t) = -\sigma \sum_j \frac{Z(\zeta_j)}{Z''(\zeta_j)} e^{-i\omega_j t} \quad (2.9)$$

as $\varepsilon(\zeta) = 1 - k^{-2}Z'(\zeta)$ and $\varepsilon'(\zeta) = -k^{-2}Z''(\zeta)$.

In the theory of continuous dielectrics (Landau & Lifshitz 1946; Nicholson 1983), wave energy density consists of electric field energy density multiplied by the so-called Brillouin factor $\partial_\omega(\omega\varepsilon_r)$. The denominator of (2.8) evokes the Brillouin factor because for each root $\omega_n = k\zeta_n$, we have $\partial_\omega(\omega\varepsilon) = \omega_n\varepsilon_\omega(\omega_n)$. This energy factor $\varepsilon_\omega(k, \zeta_j)$ is monotonically increasing towards the higher Landau modes. For this reason we speculate that in Landau damping the lowest-energy state is also the least-damped mode, and that the lower-energy states are also of greater amplitude in general perturbations.

2.3. Electrostatic eigenfunctions and transient responses

Equation (2.8) is the response when the initial data $g^*(k, \zeta)$ is an entire function of ζ . However, the phase space linear response (2.6) itself has a simple pole. Since the initial

data supplied to the kinetic equation is supposed to simulate the self-consistent response of the plasma to some perturbation, it follows that appropriate initial data may also have a pole. Consider the initial condition to be the linear response,

$$g(k, v) = -\frac{q}{m} \frac{1}{k^2} \frac{1}{\zeta_n - v} \frac{\partial f_0}{\partial v}, \tag{2.10}$$

where ζ_n is a root of the dielectric function, $\varepsilon(k, \zeta_n) = 0$. The Cauchy transform of (2.10) is the dielectric function with an added residue for $\text{Im}(\zeta) < 0$,

$$g^*(k, \zeta) = \frac{\sigma}{\zeta - \zeta_n} \left(\varepsilon(k, \zeta) + \begin{cases} 0, & \text{Im}(\zeta_n) > 0, \\ \frac{2\pi i}{k^2} \frac{\partial f_0}{\partial v} \Big|_{v=\zeta_n}, & \text{Im}(\zeta_n) < 0. \end{cases} \right) \tag{2.11}$$

Consider first $\text{Im}(\zeta) > 0$. Combining (2.7) and (2.11) and performing an inverse Fourier transform with (2.2) gives the potential $\varphi = k^{-2} e^{i(kx - \omega_n t)}$. The phase space structure is given by (2.6), and again observing the form of (2.10) and combining with the expression for the potential gives

$$f_1(x, v, t) = g(k, v) e^{i(kx - \omega_n t)}. \tag{2.12}$$

Therefore, (2.12) is a linear eigenfunction of the Vlasov equation. The phase space fluctuation grows in time and there is no phase mixing. On the other hand, in the case of $\text{Im}(\zeta) < 0$ the spectral potential contains a residue,

$$\varphi(k, \zeta) = \frac{i}{k^3} \frac{1}{\zeta - \zeta_n} - \frac{2\pi}{k^3} \frac{1}{(\zeta - \zeta_n)\varepsilon(k, \zeta)} \frac{1}{k^2} \frac{\partial f_0}{\partial v} \Big|_{v=\zeta_n}. \tag{2.13}$$

Equation (2.13) has a double pole at $\zeta = \zeta_n$ in the second term, and a simple pole at all other roots $\varepsilon(k, \zeta_j) = 0$ with $j \neq n$. Inverting the solution obtains the expression

$$\begin{aligned} \varphi(k, t) = & \left\{ 1 + \frac{i\pi}{k^2} \frac{\varepsilon_{\omega\omega}(k, \zeta_n)}{\varepsilon_\omega^2(k, \zeta_n)} \frac{\partial f_0}{\partial v} \Big|_{v=\zeta_n} \right\} \frac{e^{-i\omega_n t}}{k^2} \\ & + \sum_{j \neq n} \left(\frac{1}{(\omega_n - \omega_j)\varepsilon_\omega(k, \zeta_j)} \frac{2\pi}{k^2} \frac{\partial f_0}{\partial v} \Big|_{v=\zeta_n} \right) \frac{e^{-i\omega_j t}}{k^2}. \end{aligned} \tag{2.14}$$

Although the kinetic mode with frequency ω_n is preferentially excited by this perturbation, it is evident that all Landau modes are also necessarily involved. The form of (2.14) demonstrates phase mixing and decay at the Landau damping frequencies. However, at long wavelength the mode propagates decoupled from the others to $O(k^{-2})$.

So far the results are independent of the specific form of $f_0(v)$ other than its spatial uniformity. Now, to illustrate the partition of energy into the damped modes, the relative response amplitudes to (i) a Maxwellian perturbation and (ii) one with a single pole, namely (2.10), are computed for a Maxwellian equilibrium distribution $f_0(v)$. In case (i)

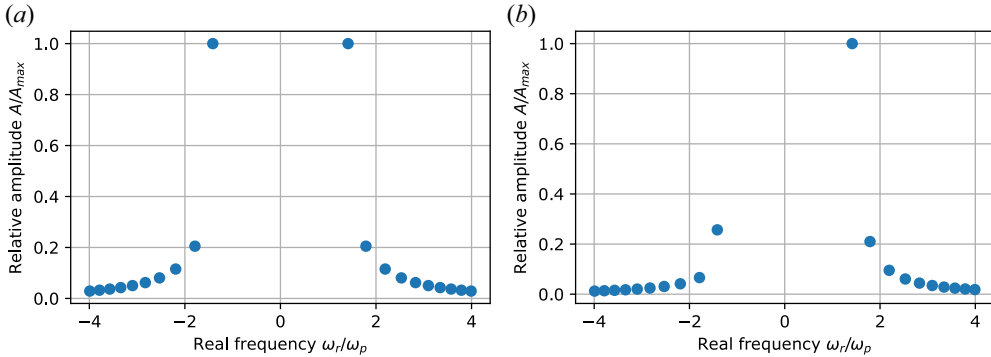


FIGURE 2. Relative potential amplitudes (normalized to the highest magnitude) of the Landau damping spectrum for the first ± 10 frequencies ω_j given a Maxwellian equilibrium distribution $f_0(v)$ at $k\lambda_D = 0.5$ for (a) the Maxwellian perturbation with $g^*(\zeta) = Z(\zeta)$, and (b) initial data as (2.10) with a single complex pole. The modes are ordered by the real part of their frequency. Higher modes are rapidly damped, as seen in figure 1 which is computed for the same equilibrium Maxwellian distribution. Panel (b) shows that while (2.10) can excite a propagating, damping plane wave it is necessarily accompanied by transient oscillations in its phase space structure with initial amplitudes up to 20 % of the primary oscillation.

the Maxwellian perturbation evolves with the potential

$$\varphi(k, t) = -2 \sum_j \frac{Z(\tilde{\zeta}_j)}{Z''(\tilde{\zeta}_j)} e^{-i\omega_j t}, \tag{2.15}$$

where $\tilde{\zeta}_j = \zeta_j/v_i$, while case (ii) evolves with the potential

$$\varphi(k, t) = \frac{1}{k^2} \left\{ \left(1 - 2\pi i \frac{Z'''(\tilde{\zeta}_n)}{(Z''(\tilde{\zeta}_n))^2} \frac{\partial f_0}{\partial v} \right) e^{-i\omega_n t} - 4\sqrt{2}\pi \frac{\partial f_0}{\partial v} \sum_{j \neq n} \frac{e^{-i\omega_j t}}{(\zeta_n - \zeta_j) Z''(\tilde{\zeta}_j)} \right\}. \tag{2.16}$$

Figure 2 compares these relative potential amplitudes for the two cases (i) and (ii), where figure 2(b) represents a rightward-propagating Langmuir wave. While mostly the primary plasma oscillation mode is excited, the higher modes make a substantial contribution.

In summary, Landau damping modes are not eigenfunctions of the Vlasov equation. If they are initialized and time is run either forward or backward they damp through phase mixing in either direction of time. However, their phase space structure is essentially the same as that of the unstable eigenfunctions, namely the plasma part of the plasma-field configuration occurring in a plasma wave. On the other hand, unstable modes are true eigenfunctions whose phase space structures do not change in time.

2.4. Visualizing the electrostatic phase space eigenfunctions

Let us visually explore the phase space structure just discussed mathematically. Given a solution ζ_n to $\varepsilon(\zeta_n, k_n) = 0$ for particular k_n (for instability, $\text{Im}(k_n \zeta_n) > 0$) the perturbed distribution is given by (2.12) in complex-conjugate pair. Examining the real part gives

$$f_1(x, v, t_0) = \alpha \text{Re}(\psi) \frac{\partial f_0}{\partial v}, \tag{2.17}$$

$$\psi(x, v) \equiv \frac{e^{ik_n(x - \zeta_n t_0)}}{\zeta_n - v} \tag{2.18}$$

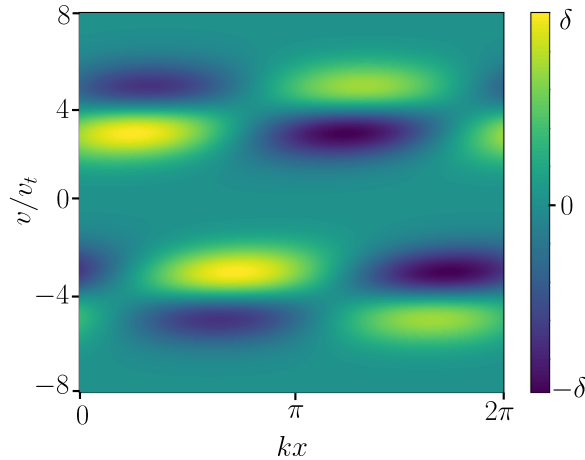


FIGURE 3. Depicted is the phase space eigenfunction of an unstable two-stream mode on two drifting Maxwellians of drift velocities $v_d = \pm 4v_t$, which appears as coupled plasma waves on each drifting distribution in the specific sense that the phase space structure on each beam is visually and mathematically similar to a Landau-damped mode of a thermal Maxwellian (i.e. the phase space structure of (2.10)). However, these plasma wave structures only occur as a normal mode, or eigenfunction, when unstable. The mode has structure in both x and v , but its zeroth velocity moment is a pure sine wave and its first moment is zero.

where α is the perturbation amplitude. Provided that no solution to $\varepsilon(\zeta, k) = 0$ has $\text{Im}(\zeta) = 0$, the denominator of ψ does not vanish and the function is well-defined. The complex function ψ is defined for convenience to account for all phase information in the perturbation. The real part is chosen arbitrarily as the linear modes come in conjugate pairs. Note that one can think of the mode as an instantaneous Cauchy transform of the distribution gradient.

For example, consider the unstable two-stream mode of two drifting Maxwellians of drift velocities $v_d = \pm 4v_t$ with wavenumber $k_0\lambda_D = 0.1$, giving a growth rate $\omega_i \approx 0.28\omega_p$. Figure 3 visualizes the phase space of the corresponding mode given by (2.17)–(2.18). The perturbation is a two-dimensional oscillatory structure in phase space, yet the zeroth moment is a pure sine wave resulting in an initial electric potential $\varphi(x) = \varphi_0 \sin(x)$. The non-separability of the perturbation is evident in figure 3.

2.5. Kinetic eigenfunctions applied to nonlinear initial-value problems

The physically correct initial data is usually discussed in the context of the thermal fluctuation spectrum (Ichimaru 1992). Linear eigenfunctions grow from spontaneous thermal fluctuations until nonlinear saturation at some significant fraction of the thermal energy (Yoon 2007; Crews & Shumlak 2022). The Vlasov model does not resolve thermal fluctuations, but this is acceptable for typical plasmas as the magnitude of such fluctuations is much less than the thermal energy.

The eigenfunction part of a general perturbation amplifies its energy while the non-eigenfunction part decays with the same time scale ω_p^{-1} . Clearly, with sufficiently small initial amplitude the non-eigenfunction part of a general perturbation does not participate in nonlinear saturation, so that sufficiently low-amplitude general perturbations are physically correct. Yet in the same way, an eigenfunction perturbation of initially large amplitude compared with the thermal fluctuation level is also physically correct. For this reason, eigenfunction perturbations yield a physically meaningful computational

Mode	1	2	3	4	5	6
Frequency, ω_r/ω_p	± 1.42	± 0.0157	0	± 1.10	± 1.20	± 1.29
Growth rate, γ/ω_p	-3.2×10^{-7}	-0.341	0.335	-0.228	-0.377	-0.488
Amplitude, $ \varphi_j /\max(\varphi)$	1	0.710	0.335	0.0701	0.0581	0.0466

TABLE 1. Relative amplitudes of electric potential for the first six linear mode pairs in a separable perturbation of two counterstreaming thermal plasmas of drift velocities $v_d = 5v_t$ and at wavenumber $k\lambda_D = 0.126$. In this case, for each non-zero frequency ω there is a pair of solutions. Due to these mode pairs the unstable mode (here of growth rate $\gamma/\omega_p = 0.335$) has only the fifth-largest relative amplitude of electric potential in the initial condition (counting the modes twice, as they come in pairs). The significance is that the unstable mode contains only a small fraction of the initialized energy, as all modes occur at the same wavelength. The amplitude and growth rate matching is here only a coincidence.

cost-savings when initialized with amplitudes just below nonlinear levels, while high-amplitude general perturbations introduce nonlinear Landau damping. Initialization at high amplitude translates to considerable computational savings for high-dimensional, computationally intensive continuum kinetic problems.

We mention an application of eigenfunction perturbations to small-amplitude perturbation problems. Sometimes linear instability growth rates are measured for verification of model implementation (Ho, Datta & Shumlak 2018; Einkemmer 2019). Small-amplitude eigenfunction perturbations allow linear instability growth rates to be deduced from data with basically arbitrary precision because there is a complete absence of Landau damping.

2.5.1. Phase space eigenfunctions applied to the two-stream instability problem

Here we refer to perturbations as ‘separable’ when they factor as $g(x, v) = h(x)f_0(v)$ with $h(x)$ representing the desired density perturbation. Given the preceding discussion, it is illustrative to compare energy traces of fully nonlinear Vlasov–Poisson simulations initialized both with general separable perturbations and eigenfunction perturbations. Consider, for example, the two-stream unstable distribution

$$f_0(v) = \frac{1}{2\sqrt{2\pi}v_t} \left(\exp \left\{ -\frac{(v - v_d)^2}{2v_t^2} \right\} + \exp \left\{ -\frac{(v + v_d)^2}{2v_t^2} \right\} \right). \quad (2.19)$$

Initialization with a separable Maxwellian perturbation, namely $g(x, v) = \alpha f_0(v)e^{ikx}$ with α a scalar amplitude, leads to the linear solution

$$\varphi(k, t) = -2\alpha \sum_j \frac{Z(\zeta_{+,j}) + Z(\zeta_{-,j})}{Z''(\zeta_{+,j}) + Z''(\zeta_{-,j})} e^{-i\omega_j t}, \quad (2.20)$$

where $\zeta_{\pm,j} \equiv (\zeta_j \pm v_d)/\sqrt{2}v_t$ are the beam-shifted phase velocities. Table 1 lists the greatest amplitudes of (2.20) for drifts $v_d = 5v_t$ at wavenumber $k\lambda_D = 0.126$, and shows that the unstable mode is only the fifth-largest amplitude. Langmuir waves influence dynamics by masking the growing mode or through nonlinear Landau damping.

Figure 4 compares the energy traces of nonlinear simulations of the two-stream instability initialized by both separable and eigenfunction perturbations. When initialized at small amplitude the type of perturbation does not make a difference to saturation

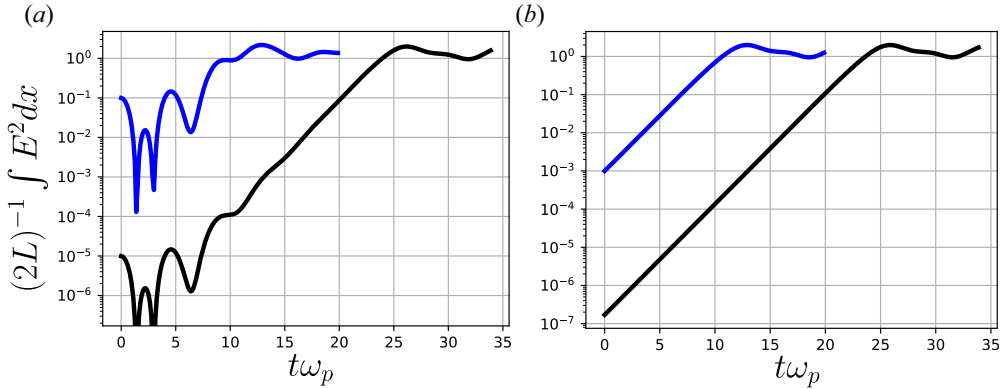


FIGURE 4. Comparison of energy traces for nonlinear simulations of a single wavelength two-stream instability of drift velocities $v_d = 5v_t$ at wavenumber $k\lambda_D = 0.126$ showing (a) separable perturbation and (b) eigenfunction perturbation. Two subcases are shown. The black trace represents a small-amplitude perturbation and the blue trace a large-amplitude one. The large-amplitude Maxwellian perturbation introduces nonlinearity, polluting the solution, while the large-amplitude eigenmode saturates equivalently as if seeded from small amplitude. In any case solutions initialized by eigenfunction perturbations undergo pure growth in the linear phase.

dynamics. On the other hand, a perturbation of large amplitude reaches saturation much faster. The large amplitude Maxwellian perturbation in figure 4(a) introduces nonlinearities and changes the energy trace from the desired evolution. Observe that the simulations initialized with the eigenfunction perturbations undergo a pure growth.

2.6. *Multidimensional dispersion function for the two-stream instability*

Electrostatic turbulence at the Debye length scale generated by streaming instability of electron beams is a ubiquitous plasma phenomenon (Rudakov & Tsytovich 1978; Che 2016), and is inherently three-dimensional. This section considers the two-stream instability in the computationally tractable two-dimensional configuration space as an example of the methodology used to compute electrostatic phase space eigenfunctions in multiple dimensions. Recall that the electrostatic dielectric function is determined by

$$\varepsilon(\omega, \mathbf{k}) = 1 + \frac{\omega_p^2}{k^2} \int \frac{\mathbf{k} \cdot \nabla_v f_0}{\omega - \mathbf{k} \cdot \mathbf{v}} d\mathbf{v} = 0. \tag{2.21}$$

Now consider a thermal two-stream distribution with equal temperatures on each beam,

$$f_0(u, v, w) = \frac{e^{-(v^2+w^2)/(2u_t^2)}}{2(2\pi)^{3/2}u_t^3} \left(\exp\left(-\frac{(u-u_d)^2}{2u_t^2}\right) + \exp\left(-\frac{(u+u_d)^2}{2u_t^2}\right) \right), \tag{2.22}$$

which differs from (2.19) in retaining three components of velocity. Having assumed an isotropic thermal velocity u_t greatly simplifies analysis; otherwise complications arise due to the elliptical level-sets of f_0 . Let the wavevector lie in the (x, y) -plane and consider (2.21). The w -component integrates out immediately, while the (x, y) -directed velocities must be rotated into the frame of the wavevector. Rotating through an angle φ to

coordinates $(v_{\parallel}, v_{\perp})$, the distribution function is $f_0(v_{\parallel}, v_{\perp}) = (f_+ + f_-)/2$ with

$$f_{\pm} \equiv \frac{1}{2\pi u_t^2} \exp\left(-\frac{(v_{\parallel} \mp \cos(\varphi)u_d)^2}{2u_t^2}\right) \exp\left(-\frac{(v_{\perp} \pm \sin(\varphi)u_d)^2}{2u_t^2}\right). \quad (2.23)$$

Evaluating the integral for each drifting component f_{\pm} as $-Z'(\zeta_{\pm})/2u_t^2$ as in Skoutnev *et al.* (2019) with drift velocity-shifted phase velocity $\zeta_{\pm} \equiv (\zeta \mp \cos \varphi u_d)/\sqrt{2}u_t$ gives

$$\varepsilon(k, \zeta, \varphi) = 1 - \frac{1}{(k\lambda_D)^2} \frac{Z'(\zeta_+) + Z'(\zeta_-)}{2} = 0. \quad (2.24)$$

The wavevector having transverse components to the drift axis decreases the effective drift by the cosine of φ , leading to maximum growth rate of longitudinal waves parallel to the streaming velocity. However, the growth of these transverse-axis components seeds a multidimensional turbulence, depending on the configuration space dimensionality.

2.7. Nonlinear simulation of two-stream instability in two spatial dimensions

Although the fastest growing mode of the two-stream problem has a beam-axis-aligned wavevector, eigenmodes with a long-wavelength transverse part $k_{\perp} \ll k_{\parallel}$ grow comparably to the fastest mode, as illustrated in figure 5 by the dielectric function $\varepsilon(k_{\parallel}, k_{\perp})$ computed using (2.24). In this way, streaming in unmagnetized plasma generically produces multidimensional Langmuir turbulence. In practice this is a three-dimensional phenomenon, but for computational tractability a streaming simulation is presented here with two space and two velocity dimensions (2D2V). We speculate that 2D2V nonlinear phase mixing is quite similar to three space and three velocity dimensions (3D3V) because the ‘total dimensionality’ of the phase space turbulence is greater than two. On the other hand, nonlinear spatial dynamics of the saturated state are likely quite different in 2D2V versus full 3D3V. A dedicated study of this issue with sufficient computer capability would be welcome.

2.7.1. Initialization of the two-dimensional two-stream simulations

Our numerical method is summarized in Appendix A. The domain used is periodic and set by fundamental wavenumbers $k_x\lambda_D = 0.05$ and $k_y\lambda_D = 0.02$. The x -axis is divided into 40 evenly spaced collocation nodes and the y -axis into 50 nodes. Velocity space is truncated at $v_{\max} = \pm 11.5v_t$, and each axis divided into 14 finite elements each of a seventh-order Legendre–Gauss–Lobatto polynomial basis. A non-uniform velocity grid is used; 10 elements are linearly clustered between $v \in (-7.5, 7.5)v_t$ and two elements into $v \in \pm(7.5, 11.5)v_t$. The drift velocity in (2.22) is set to $u_d = 3v_t$. Finally, a spatial hyperviscosity $\nu \nabla_x^4 f$ with $\nu = 10$ is added to the kinetic equation to mitigate spectral blocking with this low spatial resolution, as in Crews & Shumlak (2022). Many modes of comparable growth rates are initialized using the eigenfunction perturbations

$$f_1(x, y, u, v) = \frac{\alpha}{k} \operatorname{Re} \left(\frac{k_x \partial_u f + k_y \partial_v f}{\omega(k_x, k_y) - k_x u - k_y v} \exp(i(k_x x + k_y y + \theta)) \right) \quad (2.25)$$

with α an amplitude scalar, $\omega(k_x, k_y)$ solution to the dispersion relation for the mode (k_x, k_y) , and of random phases θ . A total of 33 modes are excited, each with the amplitude $\alpha = 0.01$; for each harmonic of the x -fundamental $k_{n,x} = nk_{1,x}$ with $n = 2, 3$ and 4, 11 harmonics of the y -fundamental are excited with $k_{m,y} = mk_{1,y}$ with $m = 0, \pm 1, \pm 2, \pm 3, \pm 4$ and ± 5 . There is no symmetry in the y -direction as different phases θ are used for the modes $\pm m$. Mode $n = 1$ has small growth rate and is not initialized.

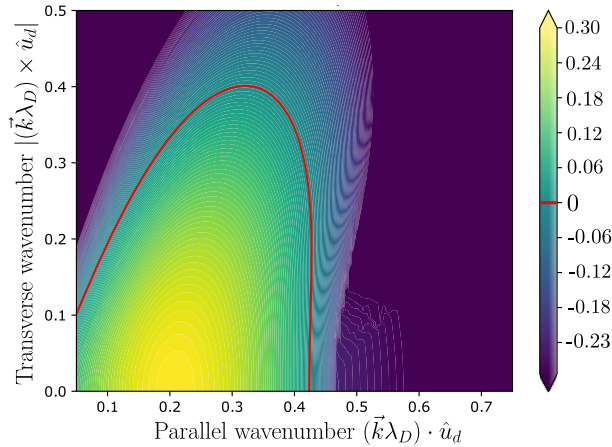


FIGURE 5. Growth rates of the electron two-stream instability as $\text{Im}(\omega)/\omega_{pe}$ for two counter-streaming Maxwellians with drift speeds relative to the thermal speed of $u_d/u_t = \pm 3$, in terms of parallel and perpendicular wavenumbers relative to the beam axis vector \hat{u}_d . The red contour indicates the line of marginal stability where $\text{Im}(\omega) = 0$. While the fastest growing mode is aligned with the beam axis (occurring at $(k\lambda_D) \cdot \hat{u}_d \approx 0.2$), modes of comparable growth rates occur with transverse wavelengths roughly five-to-ten times the unstable wavelength on-axis.

2.7.2. Two-dimensional nonlinear simulations of the streaming instability

The simulation is run to a stop time of $t\omega_p = 30$. Figure 6 shows the simulation's electric field energy trace. Hyperviscosity with this spatial resolution leads to a domain energy loss of $O(10^{-3})$ while electric energy saturates at $O(10^{-1})$. Due to the use of eigenfunction perturbations there are no oscillations in the electric field energy trace. Therefore, the simulation was initialized with a perturbation energy just two orders below saturation. In this case, this saves approximately $10\omega_p^{-1}$ of simulation time compared with, for example, a perturbation of initial energy 10^{-6} .

Figure 7 plots evolution of electric potential. Beam-axis wave energy initially predominates as electron holes form with wavenumber $k_x \gg k_y$, yet the transverse perturbations with comparable growth rates to the maximal beam-axis part lead to two-dimensional structures. Following nonlinear saturation, wave energy significantly increases in the transverse direction as the holes tilt, consolidate and isotropize. Figure 8 visualizes the domain-averaged (coarse-grained) distribution and demonstrates that isotropization associated with beam-driven electrostatic turbulence distributes coarse-grained energy into the beam-transverse directions. That is, beam-transverse temperature increases significantly in the resulting marginally stable double-humped distribution (Penrose 1960), as heat transfers from coarse-grained wave energy to the coarse-grained distribution (Nicholson 1983). These results support the notion that the continuum of electron hole solutions is key to strongly driven plasma transport (Schamel 2023).

2.8. Quasilinear kinetic simulation with phase space eigenfunctions

Quasilinear theory is the name given to the simplest closure in the hierarchy of equations resulting from separating the variables of a turbulent system into fluctuating and mean components (Vedenov 1963). The scheme of the theory is as follows: a suitable method of averaging is defined, typically temporal, spatial or ensemble averaging; the dynamical equation is averaged and the mean subtracted from the original equation to obtain the

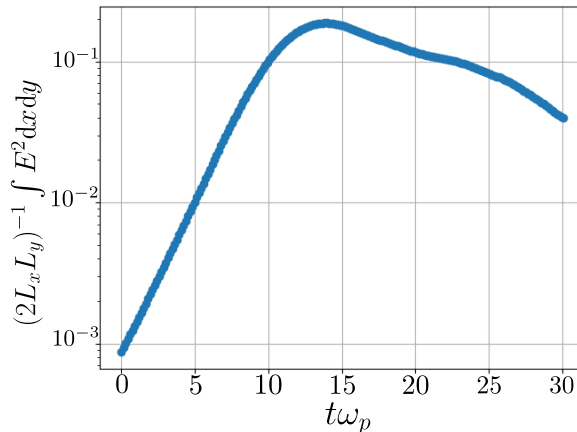


FIGURE 6. Electric energy trace of the 2D2V two-stream instability with thirty-three excited domain modes. Initialization with eigenmodes enables a perturbation just two decades below saturation energy. The aggressive spatial hyperviscosity of $\nu = 10$ leads to an energy loss of $O(10^{-3})$ by the stop time of this simulation. This artificial dissipation would not be necessary with greater spatial resolution, but the loss is well beneath the electric energy at the stop time.

mean and fluctuating components of the system; lastly a closure hypothesis is made by neglecting the ‘second fluctuation’. Under this procedure, known as ‘classic QLT’, the equation for the fluctuation becomes quasilinear and can be solved by spectral methods (Crews & Shumlak 2022). Substitution into the equation for the mean gives a diffusion equation in velocity space. Beyond classic QLT, a formulation more applicable to inhomogeneous plasmas is presented in Dodin (2022).

Diffusion equations are numerically stiff when diffusivity is large. A drawback of QLT posed as a diffusion problem is that the diffusivity is asymptotically singular in the relaxed state of an unstable system. The singularity arises as $\text{Im}(\zeta) \rightarrow 0$ around the purely real frequencies of the relaxed state (Crews & Shumlak 2022). This singularity is side-stepped by solving the equations of QLT as an initial-value problem for a system of first-order equations, resolving the linear kinetic eigenfunctions, linear Landau damping and the asymptotic ($t \rightarrow \infty$) saturation of the distribution function. There is no dimensionality reduction like in the diffusion theory, but significant advantage remains over the fully nonlinear theory because the turbulent nonlinear cascade does not form and only the unstable scales need be resolved. Further, as a first-order system there is no need to solve the dielectric function in a quasilinear simulation. To prevent spurious Landau damping it is wise to utilize kinetic eigenfunction perturbations as in § 2.5.

To demonstrate we consider the kinetic equation for electrons in a neutralizing background. Splitting the distribution function $f = \langle f \rangle_L + \delta f$ where $\langle \cdot \rangle_L$ is a spatial average, the quasilinear system in normalized units is (Crews & Shumlak 2022)

$$\frac{\partial \langle f \rangle_L}{\partial t} = \frac{\partial}{\partial v} (E \delta f)_L, \quad (2.26)$$

$$\frac{d(\delta f)}{dt} = \frac{\partial}{\partial v} E \langle f \rangle_L, \quad (2.27)$$

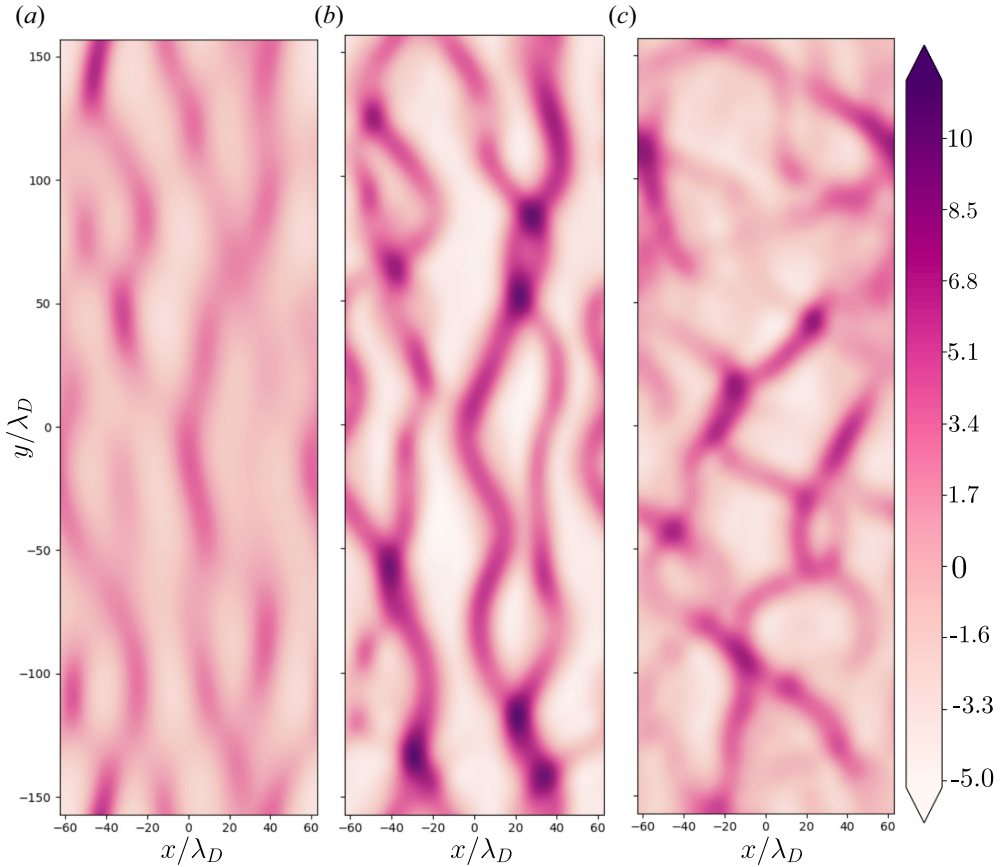


FIGURE 7. Electric potential $\varphi(x, y)$ of the 2D2V electron two-stream instability for three times: (a) $t\omega_p = 8$ (linear phase); (b) $t\omega_p = 18$ (nonlinear phase); (c) $t\omega_p = 27$ (isotropizing). The evolution begins with the formation of one-dimensional electron holes, or phase space vortex lines, transverse to the streaming axis. These vortex lines then break up after saturation into two-dimensional hole structures with more complex orbits which maintain connection to one another by the Vlasov-dynamical conservation of phase space circulation. The lines of potential in this simulation may be understood as a projection of these phase space vortex tubes.

with $d/dt = \partial_t + v\partial_x$ the change along a zero-order trajectory. Consider a finite periodic domain $x \in (0, L)$ and the expansion of the distribution in Fourier series,

$$f(x, v, t) = f_0 + \sum_{n=1}^{\infty} (f_n e^{ik_n x} + f_n^* e^{-ik_n x}). \tag{2.28}$$

The $n = 0$ component of (2.28) is the average distribution, $f_0 = \langle f \rangle_L$, and the remaining Fourier coefficients make up the Fourier spectrum of the fluctuation with $f_n^* = -f_n$. Thus,

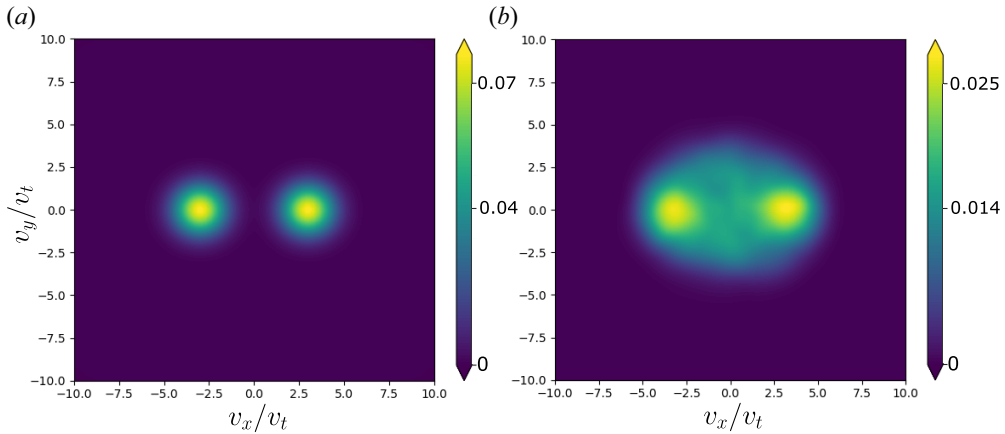


FIGURE 8. Domain-averaged (coarse-grained) distribution $\langle f \rangle_{(x,y)}(v_x, v_y)$ showing relaxation to a Penrose-stable distribution on averaged scales due to multidimensional Langmuir turbulence, for two times: (a) $t\omega_p = 0$, the unstable initial condition; (b) $t\omega_p = 30$, the stop time of the simulation. At the end of the simulation the average distribution is double-humped, having heated significantly in the direction transverse to the beam axis compared with the initial state.

dropping the symbols $\delta(\cdot)$ and $\langle \cdot \rangle_L$, (2.26) and (2.27) are

$$\frac{\partial f_0}{\partial t} = \frac{\partial}{\partial v} \langle Ef \rangle_L, \tag{2.29}$$

$$\frac{\partial f_n}{\partial t} = -ik_n v f_n + \frac{\partial}{\partial v} (E_n f_0), \quad n \geq 1, \tag{2.30}$$

$$E_n = ik_n^{-1} \int_{-\infty}^{\infty} f_n dv, \quad n \geq 1, \tag{2.31}$$

where (2.31) is obtained from Gauss’s law in the Fourier basis.

2.8.1. Numerical method for the initial-value problem for the quasilinear equations

Equations (2.29) and (2.30) are discretized in velocity space and (2.31) is applied as a constraint. First, the Fourier series is truncated at a chosen mode number (Galerkin projection) to resolve the range of instability, with the corresponding spatial grid identified as the evenly spaced collocation nodes of the frequency range in a standard manner through the fast Fourier transform. The velocity axis is to be discretized by the discontinuous Galerkin (DG) method similarly to the method in Appendix A. We consider the two velocity fluxes in (2.29) and (2.30),

$$\mathcal{T}(v) \equiv \langle Ef \rangle_L = L^{-1} \int_0^L E \delta f(x, v) dx, \tag{2.32}$$

$$\mathcal{M}_n(v) \equiv E_n f_0 = \left(ik_n^{-1} \int_{-\infty}^{\infty} f_n(v') dv' \right) f_0(v). \tag{2.33}$$

We evaluate the flux $\mathcal{T}(v)$ by the trapezoidal rule because of its ideal trigonometric quadrature properties (Boyd 2001) using the inverse fast Fourier transform of the spectra E_n and $f_n(v)$. On the other hand, the fluxes $\mathcal{M}_n(v)$ depend only on the local field mode E_n and the mean distribution $f_0(v)$, so this quantity is simply computed by quadrature in v .

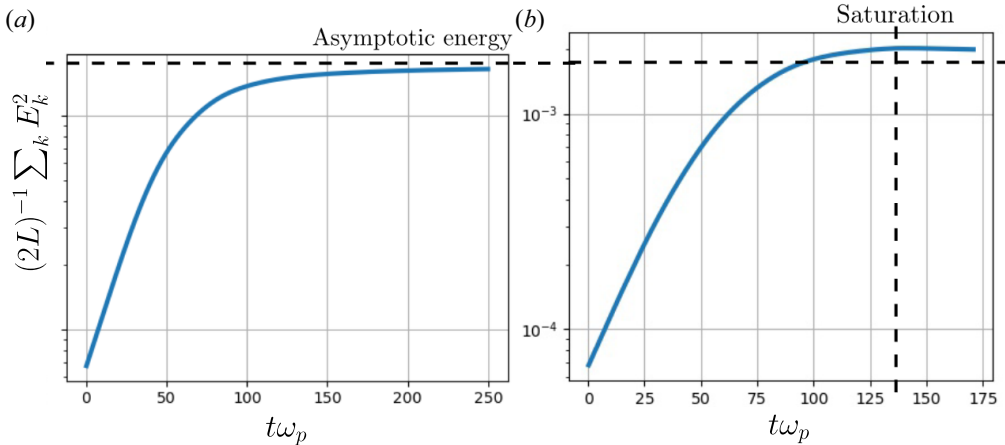


FIGURE 9. Electric energy traces are compared for (a) the quasilinear evolution, and (b) the fully nonlinear Vlasov–Poisson simulation (from the data of Crews & Shumlak (2022)) from identical initial conditions and perturbations. The quasilinear system approaches the marginally stable state asymptotically, while the fully nonlinear system saturates in a finite time due to nonlinear particle trapping. Both simulations are initialized at high though subnonlinear amplitude without subsequent Landau damping oscillations because they utilize kinetic eigenfunction perturbations, while non-eigenfunction perturbations would oscillate significantly.

Both fluxes \mathcal{T} and \mathcal{M}_n are then utilized in the DG method as a nonlinear flux. The linear translation operator $ik_n v f_n$ is discretized by quadrature and the system is integrated in time semi-implicitly by Strang splitting, as outlined in Appendix A.

2.8.2. Simulation of the bump-on-tail instability using phase space eigenfunctions

We repeat the calculation of Crews & Shumlak (2022) for the nonlinear and quasilinear evolutions of the bump-on-tail instability, with the difference that here QLT is solved as an initial-value problem in phase space instead of as a diffusion problem for the reduced distribution, and using the numerical method described in § 2.8.1. See Crews & Shumlak (2022) for the details of initialization including the domain and the zero-order distribution. In Crews & Shumlak (2022) the perturbation is constructed using the phase space eigenfunctions given by (2.10). Figure 9 compares the energy traces of the nonlinear and quasilinear simulations where QLT is solved as an initial-value problem, while figure 10 compares the spectral phase space at saturation and demonstrates the absence of phase space cascade in QLT. In addition, there is an absence of Landau damping as the perturbation is constructed from eigenfunctions.

3. Electrostatic eigenmodes with zero-order cyclotron motion

Here the electrostatic kinetic eigenfunctions of strongly magnetized plasma are illustrated by first reviewing the linearized theory (see Gurnett & Bhattacharjee (2017, p. 382) for step-by-step derivation) and then applying the linearized theory to the particular case of ring distributions of the Dory–Guest–Harris or χ -distribution type (Dory, Guest & Harris 1965) that are of special interest in space plasmas and magnetic traps. By strongly magnetized plasma we mean that the zero-order thermal magnetic force $qv_{th}B_0$ exceeds the first-order perturbation force qE_1 such that the zero-order trajectories are cyclotrons. Strongly magnetized electrostatic modes are longitudinal oscillations

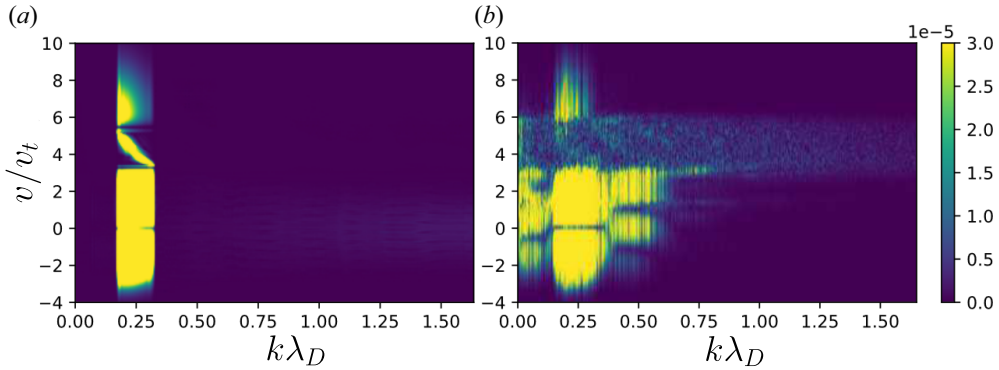


FIGURE 10. Spectral $(k\lambda_D, v/v_t)$ phase space is compared at saturation $t = 150\omega_p^{-1}$ between (a) the quasilinear system, and (b) the corresponding fully nonlinear Vlasov–Poisson simulation. The spectral phase of the quasilinear system is grossly over-resolved in $k\lambda_D$ space only for the purpose of comparison; energy remains spatially localized in QLT because the system is unable to cascade through turbulent mixing of phase space eddies, a fully nonlinear phenomenon. The phase space structures in a simulation of QLT always remain linear eigenfunctions of the form of (2.10). In this way sub-Debye length scales need not be resolved in simulation of QLT.

characterized by two fundamental frequencies, the plasma frequency ω_p and the cyclotron frequency ω_c . Defining the obliquity through $\mathbf{k} \cdot \mathbf{B} = kB \cos(\phi) = k_{\parallel}B$, the wavevector decomposes as $\mathbf{k} = k_{\parallel}\hat{e}_{\parallel} + k_{\perp}\hat{e}_{\perp}$. The spectrum is determined by the dielectric function roots $\varepsilon(\omega, k_{\perp}, k_{\parallel}) = 0$, and depends strongly on the angle between the wavevector \mathbf{k} and magnetic field \mathbf{B} . In contrast to the unmagnetized case there are undamped waves perpendicular to \mathbf{B} , including the well-known Bernstein modes of Maxwellian plasma (Bernstein 1958). We will see that electrostatic kinetic eigenfunctions have helical structure in the perpendicular velocity phase space.

3.1. Review of the Harris dispersion relation

Our treatment here follows Gurnett & Bhattacharjee (2017, § 10.2.1) with a particular focus on the phase space perturbation as a kinetic eigenfunction. Coordinates are chosen such that $\mathbf{B} = B\hat{z}$, $\mathbf{k} = k_{\perp}\hat{x} + k_{\parallel}\hat{z}$ and the velocity space is expressed in cylindrical coordinates as $\mathbf{v} = v_{\perp} \cos(\phi)\hat{v}_x + v_{\perp} \sin(\phi)\hat{v}_y + v_{\parallel}\hat{v}_z$. In these coordinates the Vlasov equation linearizes around $f_0(v_{\perp}, v_{\parallel})$ as, with $\omega_c = qB/m$,

$$\frac{\partial f_1}{\partial t} + v_{\perp} \cos \phi \frac{\partial f_1}{\partial x} + v_{\parallel} \frac{\partial f_1}{\partial z} - \omega_c \frac{\partial f_1}{\partial \phi} = \frac{q}{m} \left(E_x \cos \phi \frac{\partial f_0}{\partial v_{\perp}} + E_z \frac{\partial f_0}{\partial v_{\parallel}} \right). \quad (3.1)$$

The linearized equation is then Fourier transformed $(x, z, t) \rightarrow (k_{\perp}, k_{\parallel}, \omega)$ to yield

$$\frac{df_1}{d\phi} + i \frac{\omega - k_{\perp}v_{\perp} \cos \phi - k_{\parallel}v_{\parallel}}{\omega_c} f_1 = -i \frac{q\varphi}{m} \left(k_{\perp} \cos \phi \frac{\partial f_0}{\partial v_{\perp}} + k_{\parallel} \frac{\partial f_0}{\partial v_{\parallel}} \right). \quad (3.2)$$

Equation (3.2) is a first-order inhomogeneous equation in the cylindrical velocity-space angle ϕ and can be solved by the usual methods. Integrating the inhomogeneous term along the solution of the homogeneous equation yields

$$f_1(v_{\perp}, \phi, v_{\parallel}) = -\frac{q\varphi(k)}{m} \exp(ik_{\perp}v_y/\omega_c) \left[\frac{1}{v_{\perp}} \frac{\partial f_0}{\partial v_{\perp}} \Upsilon_1 + k_{\parallel} \frac{\partial f_0}{\partial v_{\parallel}} \Lambda_1 \right], \quad (3.3)$$

where the terms Υ_1 and Λ_1 are auxiliary wavefunctions defined as the polar Fourier series

$$\Upsilon_1 = \sum_{n=-\infty}^{\infty} \frac{n\omega_c}{\omega - k_{\parallel}v_{\parallel} - n\omega_c} J_n(k_{\perp}v_{\perp}/\omega_c) e^{in\phi}, \tag{3.4}$$

$$\Lambda_1 = \sum_{n=-\infty}^{\infty} \frac{\omega_c}{\omega - k_{\parallel}v_{\parallel} - n\omega_c} J_n(k_{\perp}v_{\perp}/\omega_c) e^{in\phi}, \tag{3.5}$$

with $J_n(z)$ a Bessel function of the first kind. The terms of Υ_1 associated with perpendicular propagation decay one order slower in n than Λ_1 , meaning that high-order resonances are more important for perpendicular propagation. Equation (3.3) is the phase space linear response for electrostatic fluctuations in a strongly magnetized plasma.

The self-consistent spectrum consists of all pairs $(\omega, k_{\perp}, k_{\parallel})$ such that the zeroth moment of $f_1(\omega, k_{\perp}, k_{\parallel}, v_{\perp}, \phi, v_{\parallel})$ results in an electric potential mode of wavenumber $(k_{\perp}, k_{\parallel})$. Integration of the phase space fluctuation gives the density fluctuation as

$$n_1(\omega, k_{\perp}, k_{\parallel}) = -i \frac{q\varphi}{m} \int_{-\infty}^{\infty} \int_0^{\infty} \left[\frac{1}{v_{\perp}} \frac{\partial f_0}{\partial v_{\perp}} \Upsilon_2 + k_{\parallel} \frac{\partial f_0}{\partial v_{\parallel}} \Lambda_2 \right] 2\pi v_{\perp} dv_{\perp} dv_{\parallel} \tag{3.6}$$

where a set of additional series, analogues of (3.4) and (3.5), are defined as

$$\Upsilon_2 = \sum_{n=-\infty}^{\infty} \frac{n\omega_c}{\omega - k_{\parallel}v_{\parallel} - n\omega_c} J_n^2(k_{\perp}v_{\perp}/\omega_c), \tag{3.7}$$

$$\Lambda_2 = \sum_{n=-\infty}^{\infty} \frac{\omega_c}{\omega - k_{\parallel}v_{\parallel} - n\omega_c} J_n^2(k_{\perp}v_{\perp}/\omega_c). \tag{3.8}$$

Substitution of n_1 into Poisson’s equation gives Harris’s dispersion relation

$$\varepsilon(\omega, k_{\perp}, k_{\parallel}) \equiv 1 - \left(\frac{\omega_p}{\omega_c}\right)^2 \frac{1}{(k\lambda_D)^2} \int_{-\infty}^{\infty} \left(\nabla_{\perp} f_{\parallel} + k_{\parallel} \nabla_{\parallel} \frac{\partial f_{\parallel}}{\partial v_{\parallel}} \right) dv_{\parallel} = 0, \tag{3.9}$$

where the integration over perpendicular velocities is broken out into the two quantities

$$\nabla_{\perp} = \int_0^{\infty} \frac{1}{v_{\perp}} \frac{\partial f_{\perp}}{\partial v_{\perp}} \Upsilon_2(v_{\perp}, v_{\parallel}) 2\pi v_{\perp} dv_{\perp}, \tag{3.10}$$

$$\nabla_{\parallel} = \int_0^{\infty} f_{\perp} \Lambda_2(v_{\perp}, v_{\parallel}) 2\pi v_{\perp} dv_{\perp}, \tag{3.11}$$

and separability of the background $f_0(v_{\perp}, v_{\parallel}) = f_{\perp}(v_{\perp})f_{\parallel}(v_{\parallel})$ has been assumed.

3.2. Amplitude limitation of linearization around zero-order cyclotron orbits

Given a zero-order spatially uniform magnetic field $\mathbf{B} = \mathbf{B}_0$ and first-order electric field perturbation $\mathbf{E} = \mathbf{E}_1$, the zero- and first-order kinetic equations are

$$(\mathbf{v} \times \mathbf{B}_0) \cdot \nabla_v f_0 = 0, \tag{3.12}$$

$$\partial_t f_1 + \mathbf{v} \cdot \nabla_v f_1 + \frac{q}{m} (\mathbf{v} \times \mathbf{B}_0) \cdot \nabla_v f_1 + \frac{q}{m} \mathbf{E}_1 \cdot \nabla_v f_0 = 0 \tag{3.13}$$

assuming a homogeneous zero-order distribution $f_0 = f_0(\mathbf{v})$. Equation (3.12) indicates gyrotropy of f_0 . This ordering is valid when the zero-order cyclotron acceleration is much

greater than the electrostatic acceleration of a typical particle. Validity translates to an amplitude restriction on electric potential and the density fluctuation. Assuming $k_{\parallel} = 0$ and comparing terms proportional to $\nabla_{\perp} f_0$ in (3.12) and (3.13) for a thermal particle gives $E_1 \ll v_{th} B_0$. Estimating the field E_1 of wavenumber k by Gauss's law gives $E_1 = e\delta n/k\epsilon_0$ for density fluctuation δn . Combining these estimates results in equivalent conditions on amplitude as measured by δn or φ ,

$$\frac{\delta n}{n_0} \ll \left(\frac{\omega_c}{\omega_p}\right)^2 (kr_L), \quad (3.14)$$

$$\frac{e\varphi}{kT} \ll \frac{1}{kr_L}, \quad (3.15)$$

for Larmor radius $r_L = v_{th}/\omega_c$. Amplitudes which exceed these inequalities are subject to electrostatic Landau damping as the dielectric function of (3.9) is not valid. Typical cyclotron instabilities have $k_{\perp} r_L \approx 1$ which limits the amplitudes of the linear modes considered in this section to amplitudes $\delta n/n_0 \ll (\omega_c/\omega_p)^2$ and $e\varphi \ll kT$.

3.3. The dielectric function for ring (χ -) distributions

The linear mode spectrum depends on the background distribution (the zero-order equilibrium). Plasma theory textbooks consider Maxwellian plasmas by expansion in the cyclotron harmonics (Gurnett & Bhattacharjee 2017, §10.2.3). Of course, in ideal collisionless plasmas with plasma parameter $\Lambda \rightarrow \infty$ distributions are expected to be observed only close enough to Maxwellian such that the Penrose criterion is satisfied.

Recent analytical work on non-Maxwellian distributions focuses on the kappa distributions (Mace & Hellberg 2009) to model observations in space plasma (Pierrard & Lazar 2010). Kappa (κ -) distributions, also called q -Gaussians, are motivated by recent advances in entropy methods (Livadiotis & McComas 2023; Zhdankin 2023). It is thought that such entropy methods may facilitate the extension of maximum entropy principles to the prediction of metastable equilibria such as non-Maxwellian velocity distributions or self-organized equilibria in magnetic confinement including tokamaks (Dyabilin & Razumova 2015) and Z pinches (Crews *et al.* 2024). Ewart *et al.* (2022) is a significant recent advance with a lucid description of collisionless relaxation.

Spatially uniform strongly magnetized plasmas must have zero-order gyrotropy so that non-Maxwellian features in perpendicular velocity space are typically ring-shaped. Ring distributions commonly arise from the loss-cone mechanism of magnetic traps or planetary magnetospheres. Early identifications of velocity-space instability in ring-distributed plasmas were made by Dory *et al.* (1965). Dory's ring distribution, known in the mathematics literature as a χ -distribution, is a type of maximum entropy distribution subject to two constraints on variance. The studies of Tataronis & Crawford (1970a) and Tataronis & Crawford (1970b) extended the theory to oblique propagation, showing maximal growth rates for near-perpendicular propagation, though analytical work was performed only with singular ring distributions. Around the turn of the millennium q -analogues of Dory's analytic ring distributions were introduced by Leubner & Schupfer (2001) and extended in Pokhotelov *et al.* (2002), motivated by the successful use of κ -distributions as q -deformations of Maxwell–Boltzmann statistics. Dory's χ -distribution is the $q \rightarrow 1$ limit of Leubner's κ -like ring distributions in the same way that the Maxwell–Boltzmann distribution is the $q \rightarrow 1$ limit of the q -Gaussian (or κ -) distributions.

For this reason, in this section we focus on Dory’s ring distribution and analyse the dielectric function for such rings assuming separability of the zero-order distribution as

$$f_0(v_{\parallel}, v_{\perp}) = f_{\parallel}(v_{\parallel})f_{\gamma}(v_{\perp}), \tag{3.16}$$

where $f_{\parallel}(v_{\parallel})$ is a Maxwellian of thermal velocity v_t and $f_{\gamma}(v_{\perp})$ is Dory’s ring function

$$f_{\gamma}(v) = \frac{1}{\pi\alpha^2} \frac{1}{\Gamma(\gamma + 1)} \left(\frac{v^2}{\alpha^2}\right)^{\gamma} \exp\left(-\frac{v^2}{\alpha^2}\right) \tag{3.17}$$

of thermal velocity α and parameter γ , where $\Gamma(z)$ is the Gamma function. The function f_{γ} is a polar distribution,

$$\int_0^{\infty} f_{\gamma}(v)2\pi v dv = 1, \quad \text{for } \text{Re}(\gamma) > -1 \tag{3.18}$$

yet is bounded at zero only for $\gamma \geq 0$. Equation (3.17) is also known as a χ -distribution and is ‘two-temperature’. That is, the ring distribution $f_{\gamma}(v_{\perp})$ is the maximum entropy distribution for $v_{\perp} \in [0, \infty)$ subject to the two constraints $\langle v_{\perp}^2 \rangle = (\gamma + 1)\alpha^2$ and $\langle (v_{\perp} - \langle v_{\perp} \rangle)^2 \rangle = \alpha^2(1 + \gamma - (\Gamma(\gamma + 3/2)/\Gamma(\gamma + 1))^2)$ or $\langle (v_{\perp} - \langle v_{\perp} \rangle)^2 \rangle = \frac{1}{4}\alpha^2 + O(\gamma^{-1})$ such that the temperature in the gyrating frame is independent of γ as $\gamma \rightarrow \infty$. Thus, the physical meaning of α is the thermal velocity in the gyrating frame, while γ is the boost to thermal energy in the laboratory frame (and need not be an integer). In this sense the distribution has two temperatures.

The ring distribution satisfies the recurrence (and $f_{-1} = 0$),

$$\frac{1}{v} \frac{df_{\gamma}}{dv} = \frac{1}{\alpha^2} \frac{f_{\gamma-1} - f_{\gamma}}{2}. \tag{3.19}$$

In the case of ring distributions of the form of (3.17), the integrals in both quantities ∇_{\perp} and ∇_{\parallel} involve only f_{γ} due to the recurrence Eq. (3.19), and suggests defining

$$\mathbb{F}_{n,\gamma}(k) \equiv \int_0^{\infty} f_{\gamma}(v)J_n^2(kv)2\pi v dv \tag{3.20}$$

which, as shown in [Appendix B](#), is a type- ${}_2F_2$ hypergeometric function with series representation (Gradshteyn & Ryzhik 2015)

$$\mathbb{F}_{n,\gamma}(x) = \frac{1}{\Gamma(\gamma + 1)} \sum_{\ell=0}^{\infty} \frac{\Gamma(2n + 2\gamma + 2\ell + 1)}{\Gamma^2(n + \ell + 1)\Gamma(2n + \ell + 1)} \frac{(-1)^{\ell}}{\ell!} x^{2(\ell+n)}. \tag{3.21}$$

We now proceed with integrating this power series over the parallel velocities. First, we can make a note on an alternative possibility. Rather than integrating the auxiliaries (3.7) and (3.8) in their summation form, it is possible to first close the summation with the Lerche–Newberger summation theorem (Newberger 1982), and to determine the perpendicular velocity integrals in (3.10) and (3.11) in closed form as hypergeometric functions, as in [Appendix C](#), for arbitrary k_{\parallel} . However, the integration over parallel velocities must then proceed by a series expansion around the poles of these hypergeometric functions, making a power series approach inevitable. On the other hand, the power series developed in this section maintains separability of terms containing the parallel velocity.

Proceeding to the integration over parallel velocities, with the parallel distribution $f_{\parallel}(v_{\parallel})$ taken as a Maxwellian distribution, the two integrals are

$$\int_{-\infty}^{\infty} \frac{n\omega_c}{\omega - k_{\parallel}v_{\parallel} - n\omega_c} f_{\parallel} dv_{\parallel} = -\frac{n}{k_{\parallel}} Z(\zeta_n), \tag{3.22}$$

$$\int_{-\infty}^{\infty} \frac{\omega_c}{\omega - k_{\parallel}v_{\parallel} - n\omega_c} \frac{\partial f_{\parallel}}{\partial v_{\parallel}} dv_{\parallel} = \frac{1}{2k_{\parallel}} Z'(\zeta_n), \tag{3.23}$$

where $Z(\zeta)$ is the plasma dispersion function and the cyclotron harmonic-shifted phase velocity is defined as $\zeta_n \equiv (\omega - n\omega_c)/\sqrt{2}k_{\parallel}v_t$. Thus, the dielectric function for loss-cones is

$$\begin{aligned} \varepsilon(\omega, k) = 1 - \left(\frac{\omega_p}{\omega_c}\right)^2 \frac{1}{(kr_L)^2} \sum_{n=-\infty}^{\infty} \left[Z'(\zeta_n) \mathbb{F}_{n,\gamma}(k_{\perp}r_L) \right. \\ \left. + \frac{n}{k_{\parallel}r_L} Z(\zeta_n) \left\{ \mathbb{F}_{n,\gamma-1}(k_{\perp}r_L) - \mathbb{F}_{n,\gamma}(k_{\perp}r_L) \right\} \right]. \end{aligned} \tag{3.24}$$

Equation (3.24) reduces to the standard series for a Maxwellian ($\gamma = 0$) by the identity $\mathbb{F}_{n,0}(k) = e^{-k^2} I_n(k^2)$ where $I_n(k)$ is the modified Bessel function of the first kind.

3.4. Perpendicular propagation in ring distributions

In the limit of perpendicular propagation, $k_{\parallel} \rightarrow 0$, the series (3.24) in the cyclotron harmonics simplifies as the terms proportional to $Z(\zeta_n)$ vanish. Further, by use of the Lerche–Newberger summation theorem two alternatives to the power series for the perpendicular cyclotron wave dielectric function may be developed which incorporate the contributions from the cyclotron harmonics to all orders. The derivation of these expressions may be found in Appendix C. The first is a closed form, a hypergeometric function with complex poles at the cyclotron resonances,

$$\begin{aligned} \varepsilon(\omega, k_{\perp}) = 1 + \left(\frac{\omega_p}{\omega_c}\right)^2 \frac{1}{(k_{\perp}r_L)^2} \left\{ {}_2F_2 \left[\begin{matrix} \frac{1}{2}, & \gamma + 1 \\ 1 + \omega/\omega_c, & 1 - \omega/\omega_c \end{matrix} \right] (-2(k_{\perp}r_L)^2) \right. \\ \left. - {}_2F_2 \left[\begin{matrix} \frac{1}{2}, & \gamma \\ 1 + \omega/\omega_c, & 1 - \omega/\omega_c \end{matrix} \right] (-2(k_{\perp}r_L)^2) \right\} = 0 \end{aligned} \tag{3.25}$$

and the second form is a representation of (3.25) as a trigonometric integral generalizing that used in Tataronis & Crawford (1970a), Vogman, Colella & Shumlak (2014) and Datta, Crews & Shumlak (2021),

$$\varepsilon(\omega, k) = 1 + \left(\frac{\omega_p}{\omega_c}\right)^2 \csc(\pi\omega/\omega_c) \int_0^{\pi} \sin(\theta) \sin(\theta\omega/\omega_c) L_{\gamma}(\beta) \exp(-\beta) d\theta \tag{3.26}$$

with $\beta \equiv 2 \cos^2(\theta/2)(k_{\perp}r_L)^2$ and $L_{\gamma}(\beta)$ the Laguerre polynomial of order γ . Equation (3.26) is particularly suited to numerical calculation by quadrature. Hypergeometrics similar to (3.25) have been obtained for the Maxwellian plasma and for κ -distributions (Mace 2004; Mace & Hellberg 2009), and reduce to the Maxwellian result for the parameter $\gamma = 0$. Observe that (3.25) and (3.26) are functions of frequency and not of phase velocity as there is no ballistic contribution to the zero-order motion. It is expected that (3.24)–(3.26) will be the basic dispersion functions from which to build the q -analogues for χ -distributions proposed by Leubner & Schupfer (2001).

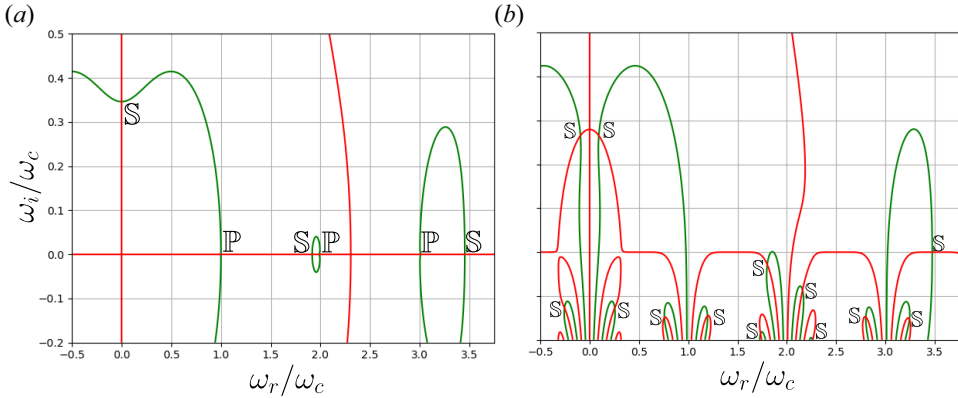


FIGURE 11. Contours of $\text{Re}(\epsilon) = 0$ (green) and $\text{Im}(\epsilon) = 0$ (red) for the electrostatic dispersion function of a loss-cone-distributed plasma with parameters $\omega_p = 10\omega_c$, $\gamma = 6$, and $k_\perp r_L = 0.9$ for case (a) 90° propagation and case (b) 85° propagation. Either a solution or a pole occurs at an intersection of these two curve families. Solutions to the dispersion relation $\epsilon(\omega, k) = 0$ are labelled \mathbb{S} while simple poles are labelled \mathbb{P} . There are no poles for oblique ($< 90^\circ$) propagation. Solutions correspond to the first few electron Bernstein modes. The dispersion function shows Gaussian-like responses in the lower-half plane for the oblique wave, an indicator of dissipative wave–particle resonance near the cyclotron harmonics.

3.5. Visualization of the dispersion function and phase space eigenfunctions

Figure 11 plots the electrostatic dispersion function in the complex frequency plane for a ring distribution of $\gamma = 6$ for magnetization $\omega_c/\omega_p = 0.1$ at wavenumber $kr_L = 0.9$. A plethora of solutions to the complex dispersion function $\epsilon = 0$ is illustrated by the intersection of the zeros of the real and imaginary parts, which take place at both solutions and poles. Complex poles at the cyclotron harmonics occur only for the case $k_\parallel \rightarrow 0$, as evident from the cosecant function $\text{csc}(\pi\omega/\omega_c)$ in (3.26). In this way solutions and simple poles can be clearly distinguished. It is clear that, given zero-order cyclotron orbits, oblique modes are Landau damped but perpendicular modes are not. When wave amplitudes violate the inequality of (3.14) nonlinear phenomena occur, and perpendicular waves are also Landau damped. In this situation one may see streaming instabilities in numerical experiments in the magnetization transition regime $\omega_c \approx \omega_p$.

Therefore, perpendicularly propagating linear modes do not experience Landau resonance so that all such modes are true eigenfunctions. The phase space structure associated with these cyclotron waves (that is, (3.3)) consists of helical modes in the perpendicular velocity space, since the primary phase component is $\exp(i(kx + n\phi - \omega t))$ for a mode with frequency $\omega \approx n\omega_c$, with ϕ the cylindrical velocity space angle. The simplest example of such helical phase space modes are the electron Bernstein modes. Figure 12 visualizes the eigenfunctions of the first and second cyclotron harmonics for a Maxwellian background distribution $f_0(v_\perp)$ in the phase space (x, u, v) with (u, v) the perpendicular velocity space and x the propagation coordinate perpendicular to the background magnetic field. With non-zero real frequency these helical modes propagate through phase space.

3.6. Simulation of perpendicular electron cyclotron loss-cone instability

Here kinetic eigenfunction initialization is illustrated for the instability of an electron loss cone to perpendicular cyclotron waves in a neutralizing background, as studied in Vogman

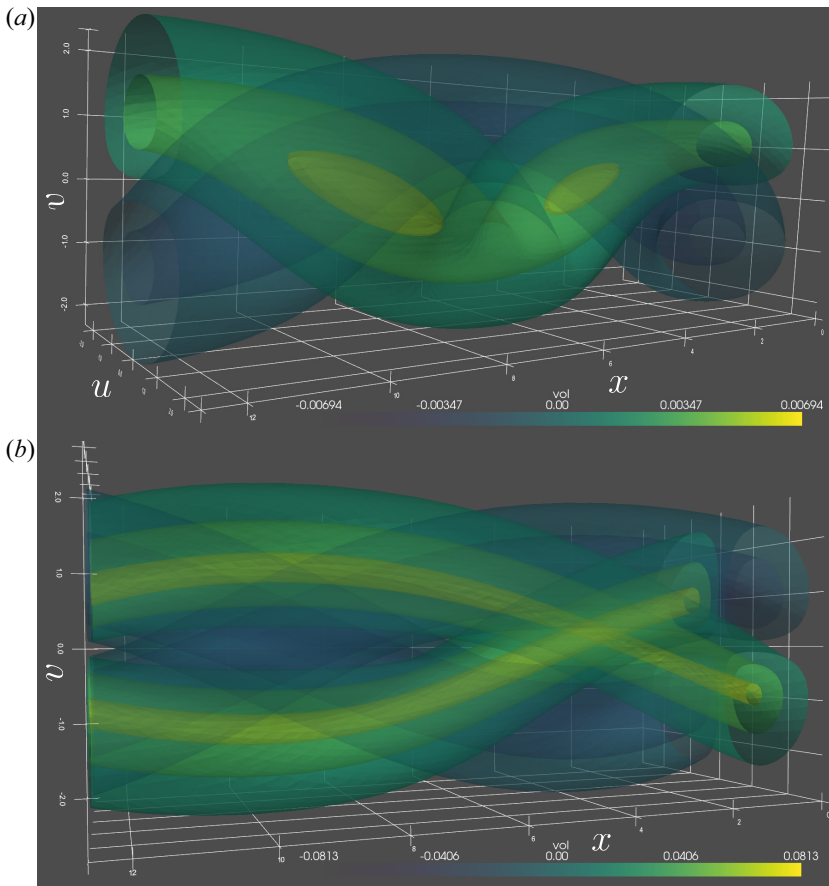


FIGURE 12. Phase space eigenfunctions of (a) the first and (b) the second cyclotron-harmonic electron Bernstein waves propagating orthogonal to \mathbf{B}_0 , visualized in the phase space (x, u, v) . The order of the cyclotron harmonic determines the number of helical strands of a given sign. The phase space eigenfunction propagates in the laboratory frame, but when the velocity space is observed at a fixed spatial coordinate the eigenfunction rigidly rotates in the perpendicular velocity space. Balanced counterpropagating modes produce a stationary wave.

et al. (2014). Normalizing to the Debye length, plasma frequency and thermal velocity, and the fields by $E_0 = v_{th}B_0$, the Vlasov–Poisson equations are

$$\partial_j f + F^j \partial_j f = 0, \tag{3.27}$$

$$\frac{d^2 \varphi}{dx^2} = \int_{-\infty}^{\infty} \int_{-\infty}^{\infty} f(x, u, v) du dv - 1, \tag{3.28}$$

$$F = \left[u, \quad \frac{d\varphi}{dx} - vB_{\text{ext}}, \quad uB_{\text{ext}} \right]^T \tag{3.29}$$

with coordinates (x, u, v) . The external magnetic field B_{ext} is set such that the magnetization parameter $\omega_c/\omega_p = B_{\text{ext}}$ is in normalized units. Two single-mode simulations termed *A* and *B* are performed for (3.27)–(3.29) in the highly unstable over-dense parameter regime $\omega_p = 10\omega_c$ using as eigenvalues two solutions to

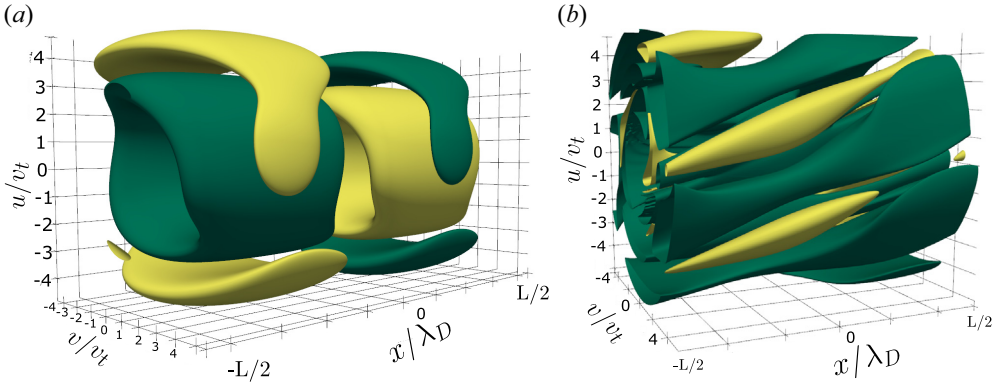


FIGURE 13. Shown here are the perturbations $f_1 \equiv f - f_0$ at time $t = 0$ for (a) simulation A with $\omega_r = 0$ and (b) simulation B with $\omega_r \neq 0$, each with isosurfaces at 30% of the minimum (green) and maximum (yellow). The considered eigenfunctions $f_1(x, u, v)$ consist of twisting islands in the phase space, capturing the combined physics of translation, electric acceleration and magnetic gyration. Translating modes ($\omega_r \neq 0$) are associated with a helical structure.

$\varepsilon(\omega, k) = 0$, namely $(k_A \lambda_D, \omega_A / \omega_c) \approx (0.886, 0.349i)$ and $(k_B \lambda_D, \omega_B / \omega_c) \approx (1.4, 1.182 + 0.131i)$ found using the integral form of (3.26) with 50-point Gauss–Legendre quadrature.

In this situation, case A corresponds to a stationary mode with wavelength long compared with the thermal Larmor radius, similar to the two-stream instability studied in the unmagnetized case, while case B corresponds to a destabilized propagating Bernstein-like mode at the first cyclotron harmonic with more significant finite Larmor radius effect. The spatial domain is set to $L = 2\pi/k$ in each case and the velocity boundaries to $u_{\max}, v_{\max} = \pm 8.5$. We perturb these nonlinear simulations using the phase space eigenfunctions corresponding to the eigenvalue pairs $(k_A, \omega_A), (k_B, \omega_B)$.

Figure 13 shows isocontours of the phase space eigenfunctions used as the initial perturbations. Case A has a phase space structure similar to the basic plasma wave seen in the two-stream instability, while case B has a helical structure as a cyclotron mode with $\omega_r \approx \omega_c$. We reiterate here that the eigenfunction perturbation allows arbitrary perturbation amplitude and still produces the same nonlinear phenomena, namely the saturated state or mode coupling/conversion. However, with zero-order B_0 the initial amplitude must not exceed the limit of (3.14) or nonlinear phenomena will develop as the perturbation electric force is not first order compared with the thermal magnetic force.

3.6.1. Numerical method for loss-cone simulations

The problem is evolved numerically using the DG method described in Appendix A and in Crews & Shumlak (2022), with the difference that the spatial coordinate is not Fourier transformed but also discretized by DG method. We use an element resolution $(N_x, N_u, N_v) = (25, 50, 50)$ and nodal basis of $n = 8$ Legendre–Gauss–Lobatto nodes per dimension, while the Shu–Osher SSPRK3 method is used to integrate the semidiscrete equation in time. These instabilities grow on a slow time scale relative to the plasma frequency; that is, they grow at a fraction of the cyclotron time scale ω_c^{-1} , while time t is normalized to the plasma frequency ω_p^{-1} . Thus, these instabilities take many plasma periods to reach nonlinear saturation beginning from amplitudes below the limit of (3.14). Simulation A reaches saturation around $t = 100$ and runs to $t = 175$ while simulation B saturates at around $t = 175$ and stops at $t = 200$.

Three-dimensional isosurface plots were produced using PyVista, a Python package for VTK (visualization toolkit). To prepare the data, an average is taken of nodal values lying on element boundaries for smoothness, and the eight-nodes per element are resampled to 25 linearly spaced points per axis and per element onto the basis functions of the DG method. These isocontours are shown for simulations *A* and *B* in figures 14 and 15, respectively.

3.6.2. Fully nonlinear single-mode loss-cone simulation results

Figure 16 shows the electric potentials $\varphi(x)$ in simulations *A* and *B*, computed using the numerical method described in § 3.6.1. In simulation *A* the wave potential $\varphi(x)$ is stationary with a weakly fluctuating boundary, so that part of the density $f(x, v)$ within the potential well executes trapped orbits. This results in a trapping structure with orbits tracing a nonlinear potential similar to the characteristic pendulum-like cats-eye separatrix of the single-mode electrostatic two-stream instability. In this case the electrons are magnetized and execute zero-order cyclotron motion so that the trapping separatrix in simulation *A* is instead in the form shown by the isosurfaces. The saturated state of simulation *A* is a lattice of one-dimensional strongly magnetized electron holes. The continuum of such hole solutions is key to strongly driven plasma transport physics (Schamel 2023). Two-dimensional axisymmetric magnetized holes are the focus of analytical work in Hutchinson (2020) and Hutchinson (2021).

The saturated wave potential of simulation *B*, on the other hand, translates with positive phase velocity $\zeta \approx \omega_r/k$. The region of particle interaction translates along with the wave potential and forms a vortex structure in the phase space density $f(x, u, v)$. The centre of this kink continues to tighten as the simulation progresses, leading to progressively finer structures just as in simulation *A*. This effect is in agreement with the filamentation phenomenon and introduces simulation error as the structures lead to large gradients on the grid scale where discreteness produces dispersion error. For this reason the simulation is stopped at $t = 200$. This solution is perhaps somewhat artificial as it is obtained by single-mode initialization via its phase space eigenfunction, thereby not disturbing modes of greater growth rate. This is demonstrated through the energy traces in figure 17, showing that simulation *A* saturates with a greater proportion of the plasma thermal energy than simulation *B*. The solution of simulation *B* has the significance of a propagating train of nonlinear electrostatic cyclotron waves with associated electron holes, driven unstable by the free energy of a ring distribution.

3.6.3. Experimental consequences of cyclotron loss-cone instabilities

Magnetic mirror trapping requires the maintenance of a loss-cone distribution in the confined plasma. Simulations such as these, and QLTs, maintain that kinetic instabilities lead to a relaxation of the distribution function on macroscopic scales towards near-Maxwellian distributions, along with long-lived vortical structures in the phase space. By examination of the dispersion functions one finds that phase space instability may be suppressed when $\omega_p \ll \omega_c$. Assuming equal electron and ion temperatures and densities, we may write for the plasma beta

$$\beta = \left(\frac{v_{ti}}{c}\right)^2 \left(\frac{\omega_{pi}}{\omega_{ci}}\right)^2 = \left(\frac{r_{Li}}{\lambda_i}\right)^2 \quad (3.30)$$

with $\lambda_i = c/\omega_{pi}$ the ion skin depth. Thus, non-Maxwellian features such as ring distributions, as χ -distributions or their κ -analogues (Pokhotelov *et al.* 2002; Leubner 2004), are expected to persist in very low- β plasma, in much the same way in which for weakly magnetized plasma the κ -distributions persist in the collisionless regime when the

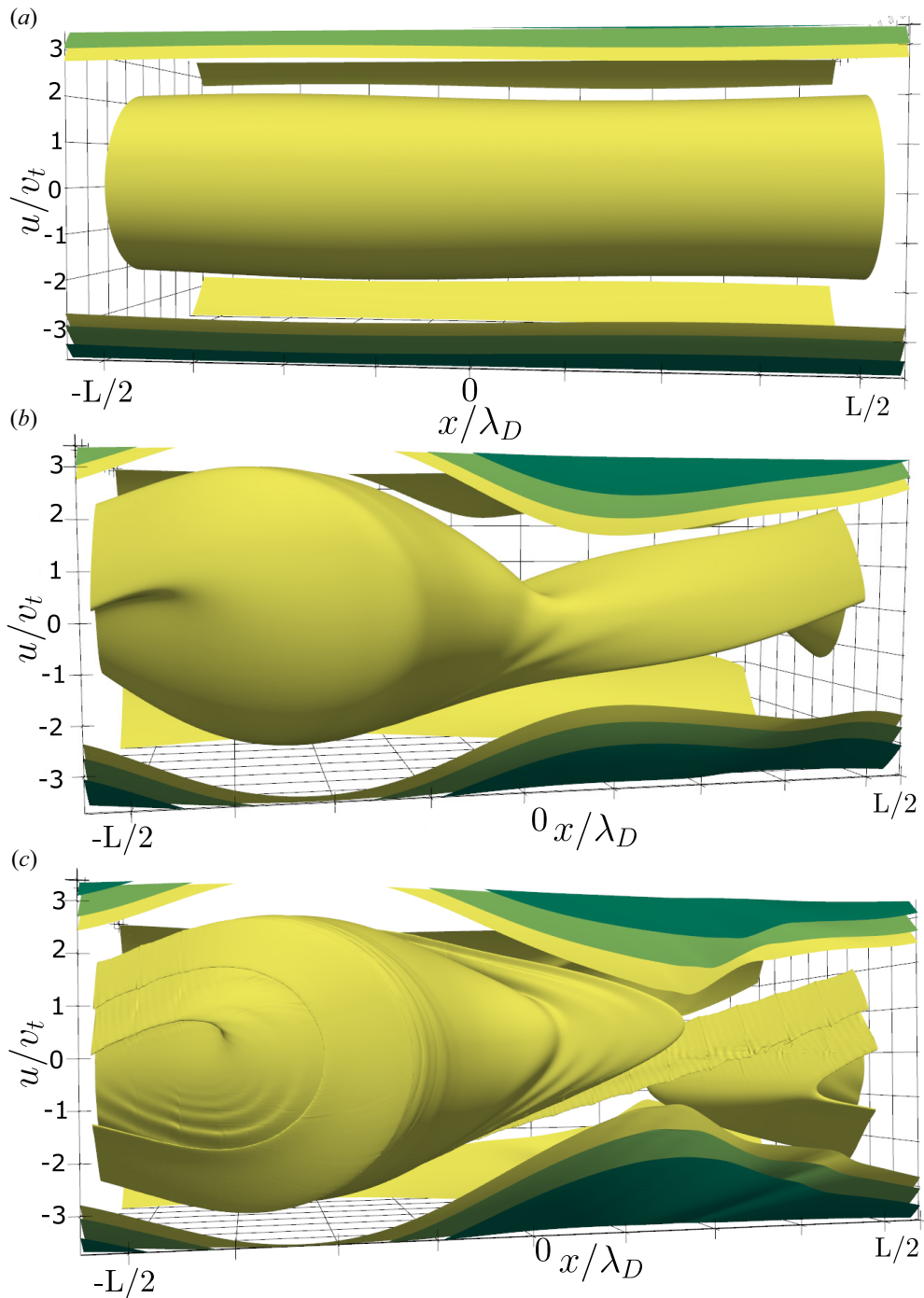


FIGURE 14. Phase space view (x, u, v) of simulation *A* focused on (x, u) -plane as isocontours at 15% of $\max(f)$ shown in yellow, at times (a) $t = 0$, (b) $t = 80$ and (c) $t = 120$. The domain within the original ring is shown with $(u, v) \in (-3.5, 3.5)$ to focus on the trapping dynamics. The trapping structure consists of a ribbon winding around a separatrix, while the outer bulk ring distribution maintains passing trajectories. This saturation geometry is typical for electrostatic potentials in a magnetic field as the magnetic force depends on the sign of the transverse velocity.

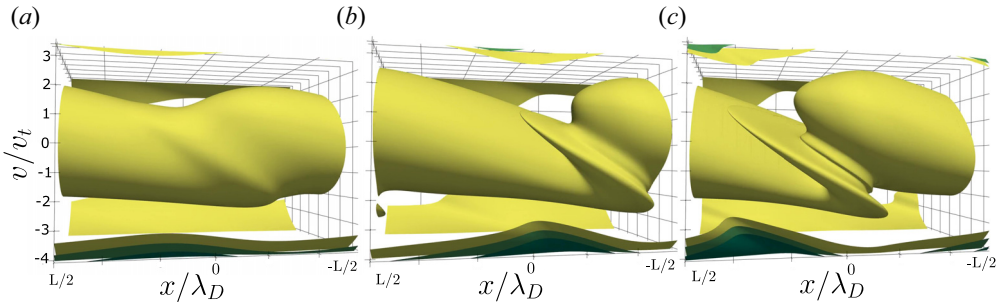


FIGURE 15. Phase space view looking on $(-x, v)$ -plane of simulation *B* at 15% isocontours of $\max(f)$ (yellow), with (a) the nonlinear mode developing at $t = 100$, (b) the developed vortex at $t = 160$ and (c) the saturated vortex translating at $t = 180$. The mode is seen to be a growing, translating electrostatic potential $\varphi(x)$ of positive phase velocity $v_\varphi = \omega_r/k$ with an underlying phase space vortex structure centred at $(u, v) = 0$. The vortex shape is explained by considering the trajectory of a test particle in the wave. That is, particles with a velocity close to that of the wave see a stationary potential and are accelerated to a high u -velocity. They then translate towards positive x while their velocity vector is rotated by the Lorentz force to $-u$ at a rate close to the wave frequency (as $\omega_r \approx 1.2\omega_c$) and repeats the cycle.

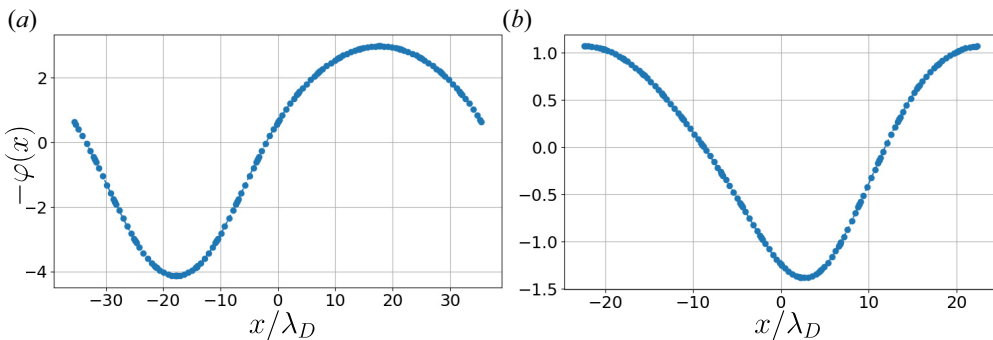


FIGURE 16. Electric potentials $\varphi(x)$ at saturation of the two studied cases, for (a) simulation *A* at $t = 120$ and (b) simulation *B* at $t = 180$. The potential of *A* is stationary while that of *B* is translating to the right. The negative of potential $-\varphi(x)$ is shown in order to account for the electron's negative charge. In both cases electron holes develop in the potential wells of $-\varphi(x)$.

plasma parameter $\Lambda \gg 1$. Further discussion on the consequences of mirror instability in high- β space plasma can be found in Pokhotelov *et al.* (2004).

4. Electromagnetic eigenmodes with zero-order ballistic trajectories

We return to weakly magnetized plasma where the zero-order magnetic field is weak enough compared with perturbations such that zero-order motion is ballistic. We consider the electromagnetic linear response, determine the plasma and field configurations of the kinetic eigenfunctions and utilize them to initialize one- and two-dimensional nonlinear simulations of collisionless electromagnetic instability. We then study the magnetic-trapping electron holes resulting from electromagnetic instability. Purely electromagnetic instability arises from pressure anisotropy, in which case the linear eigenfunctions are known as Weibel instabilities (Weibel 1959), although streaming instability may still be determined as electrostatic theory is contained in the limit $\zeta \ll c$.

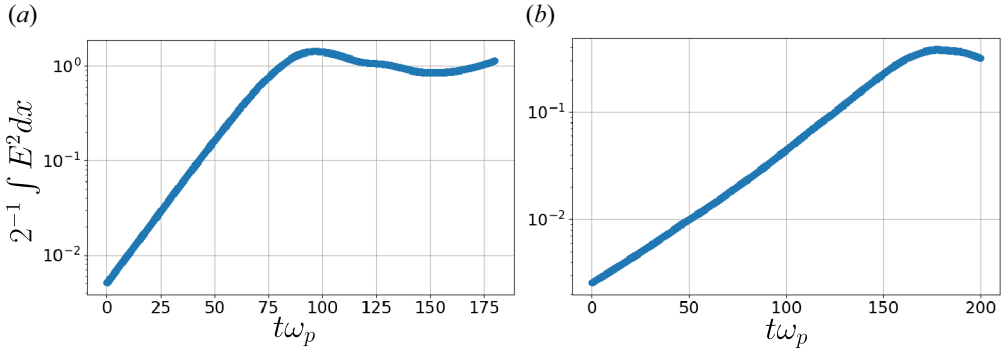


FIGURE 17. Domain-integrated electric field energy traces for simulations (a) *A* and (b) *B*. The thermal energy of the zero-order distribution is 0.25 per unit length with $\gamma = 6$ and $\alpha = 1$. In simulation *A* this corresponds to a domain-integrated thermal energy of $E_A \approx 17.8$ and in simulation *B* to $E_B \approx 11.2$. Therefore, in both cases the instability saturates with an electric energy a few per cent of the thermal energy, approximately 6% in *A* and 2.5% in *B*.

Linearization of the Vlasov–Maxwell system around a weakly magnetized spatially uniform equilibrium $f_0(\mathbf{v})$ with no mean drift yields the system

$$\partial_t f_1 + \mathbf{v} \cdot \nabla_x f_1 + \frac{q}{m} (\mathbf{E} + \mathbf{v} \times \mathbf{B}) \cdot \nabla_v f_0 = 0, \tag{4.1}$$

$$\partial_t \mathbf{B} = -\nabla \times \mathbf{E}, \tag{4.2}$$

$$c^{-2} \partial_t \mathbf{E} = -\mu_0 \mathbf{j}_1 + \nabla \times \mathbf{B}. \tag{4.3}$$

Faraday’s equation gives $\mathbf{B} = \omega^{-1} \mathbf{k} \times \mathbf{E}$ such that the spectral Lorentz force is

$$\mathbf{E} + \mathbf{v} \times \mathbf{B} = \omega^{-1} ((\omega - \mathbf{k} \cdot \mathbf{v}) \mathbf{E} + (\mathbf{v} \cdot \mathbf{E}) \mathbf{k}), \tag{4.4}$$

and a two-sided-in-time quasianalysis produces the Vlasov linear response as

$$i\omega f_1 = \frac{q}{m} \mathbf{E} \cdot \nabla_v f_0 + \frac{q}{m} (\mathbf{v} \cdot \mathbf{E}) \frac{\mathbf{k} \cdot \nabla_v f_0}{\omega - \mathbf{k} \cdot \mathbf{v}}. \tag{4.5}$$

The spectral time-derivative of the perturbed current follows as

$$\mu_0 (-i\omega \mathbf{j}_1) = \frac{\omega_p^2}{c^2} \left(\mathbf{E} - \int \mathbf{v} (\mathbf{v} \cdot \mathbf{E}) \frac{\mathbf{k} \cdot \nabla_v f_0}{\omega - \mathbf{k} \cdot \mathbf{v}} d\mathbf{v} \right). \tag{4.6}$$

The first term of the phase space linear response has no resonant denominator and thus yields a non-thermal perturbed current independent of the zero-order distribution function, while the second term encodes resonance between the plasma and its wave field.

4.1. Tensor components for arbitrary Cartesian coordinates

In Cartesian coordinates (x, y, z) with wavevector $\mathbf{k} = k_x \hat{x} + k_y \hat{y} + k_z \hat{z}$, the dielectric tensor (Skoutnev *et al.* 2019) is obtained from combination of (4.6) and (4.3) as

$$\left. \begin{aligned} \varepsilon_{ij} E_j &= 0, \\ \varepsilon_{ij} &= \delta_{ij} - \frac{c^2 k^2}{\omega^2} \left(\delta_{ij} - \frac{k_i k_j}{k^2} \right) - \frac{\omega_p^2}{\omega^2} \left(\delta_{ij} - \int v_i v_j \frac{\mathbf{k} \cdot \nabla_v f_0}{\omega - \mathbf{k} \cdot \mathbf{v}} d\mathbf{v} \right). \end{aligned} \right\} \tag{4.7}$$

In the formal initial-value problem an initial-value vector results in the system $\varepsilon_{ij}E_j = g_i$. Typically in Cartesian form the moment integrals are inseparable because of the resonant denominator $\omega - \mathbf{k} \cdot \mathbf{v}$, yet are separable when the frame is chosen with one coordinate aligned with the wavevector such that the resonant denominator appears as $\omega - kv_{\parallel}$.

4.2. Electromagnetic susceptibility and the eigenvalue problem

Reformulation of (4.7) as an eigenvalue problem for the phase velocity ζ allows calculation of electric field eigenfunctions \mathbf{E} naturally consistent with the corresponding phase space eigenfunction f_1 given by (4.5). This facilitates construction of initial conditions for simulation of Vlasov–Maxwell instabilities. Multiply by ω^2 and pull out the diagonal tensor $\omega^2\delta_{ij}$. Define the integrals encoding resonant wave–particle interaction into the self-consistent perturbation current as

$$I_{ij} \equiv \int_{\mathcal{C}} v_i v_j \frac{\mathbf{k} \cdot \nabla_{\mathbf{v}} f_0}{\omega - \mathbf{k} \cdot \mathbf{v}} d\mathbf{v}, \quad (4.8)$$

where the integral is evaluated on the Landau contour \mathcal{C} , i.e. analytically continued to the lower-half complex ω -plane. The dielectric tensor system may then be rewritten as

$$\left\{ \delta_{ij} - I_{ij} + (k\lambda_c)^2 \left(\delta_{ij} - \frac{k_i k_j}{k^2} \right) \right\} E_j = \left(\frac{\omega}{\omega_p} \right)^2 E_i, \quad (4.9)$$

where $\lambda_c = c/\omega_p$ is the inertial length. The resonant integrals are naturally functions of the phase velocity $\zeta = \omega/k$, so one can also express the system as

$$\frac{1}{(k\lambda_D)^2} \left\{ \delta_{ij} - I_{ij} + (k\lambda_c)^2 \left(\delta_{ij} - \frac{k_i k_j}{k^2} \right) \right\} E_j = \left(\frac{\zeta}{v_i} \right)^2 E_i. \quad (4.10)$$

Equation (4.10) casts the problem in eigenvalue form as the system of integral equations

$$\chi(k, \zeta)\mathbf{E} = \zeta^2\mathbf{E}. \quad (4.11)$$

As in the scalar Poisson problem there is a spectrum of solutions ζ for a given k , obtained by determining a root of the characteristic function $D(k, \zeta) \equiv \det(\chi - \zeta^2 I) = 0$. As in the scalar problem only unstable solutions satisfying $\text{Im}(\zeta) > 0$ constitute normal modes of oscillation. In unmagnetized spatially uniform plasma these modes are either streaming instabilities (two-stream, Buneman, ion-acoustic) or generalized Weibel instabilities. In either case their effect is thermalizing on coarse-grained scales by reducing relative velocities far from equilibrium. Casting the dielectric tensor for zero-order cyclotron motion (Gurnett & Bhattacharjee 2017, p. 408) into an eigenvalue problem proceeds in the same manner; the main difference is that the integrals I_{ij} are sums over Doppler-shifted cyclotron resonances and their calculation, though methodical, is lengthy.

Having determined a particular eigenvalue ζ_n^2 such that $D(k, \zeta_n) = 0$, the corresponding electric field eigenfunction \mathbf{E}_n is found by solving for the eigenvector of the matrix $\chi_n \equiv \chi(\zeta_n, k)$ with eigenvalue ζ_n^2 . The other two eigenvalues of the matrix χ_n are spurious as they do not correspond to solutions of (4.11). The magnetic field eigenfunction is obtained through $\mathbf{B}_n = \zeta_n^{-1} \hat{\mathbf{k}} \times \mathbf{E}_n$, and the phase space eigenfunction $f_{1,n}$ from (4.5).

4.3. Dielectric tensor components for the anisotropic Maxwellian

In order to illustrate the Weibel instability due to anisotropy in a plasma with zero-order ballistic trajectories it is useful to consider the anisotropic Maxwellian, or

multiple-temperature, zero-order distribution (Davidson *et al.* 1972). Anisotropy is a key element of kinetic equilibrium in flowing magnetized plasmas (Mahajan & Hazeltine 2000), and the anisotropic Maxwellian is the simplest anisotropic model distribution to investigate pure Weibel instability. Let (x, y, z) and (u, v, w) be Cartesian coordinates in configuration space and velocity space, respectively. Consider a three-temperature Maxwellian distribution given by

$$f_0 = \frac{1}{(2\pi)^{3/2}\theta_u\theta_v\theta_w} \exp\left\{-\frac{1}{2}\left(\frac{u^2}{\theta_u^2} + \frac{v^2}{\theta_v^2} + \frac{w^2}{\theta_w^2}\right)\right\}. \tag{4.12}$$

For purpose of illustration we obtain from (4.12) one- and two-dimensional model problems of Weibel instability by letting the wavevector lie in the (x, y) -plane and the \hat{z} -direction be the wave binormal. These model problems have the advantage of zero-order electrostatic stability such that all eigenfunctions are fully electromagnetic.

With the wavevector in the (x, y) -plane the off-diagonal integrals I_{13}, I_{23} vanish as $\langle w \rangle = 0$, so that the \hat{z} -directed perturbation does not contribute to the (x, y) -plane's perturbation current, decoupling the binormal from the longitudinal and transverse components (Sharma & Bhatnagar 1976; Datta *et al.* 2021). A fully general wavevector would couple all three components of the perturbation. Equation (4.7) simplifies to

$$\begin{Bmatrix} \omega^2 - \omega_p^2(1 - I_{11}) & \omega_p^2 I_{12} & 0 \\ \omega_p^2 I_{12} & \omega^2 - c^2 k^2 - \omega_p^2(1 - I_{22}) & 0 \\ 0 & 0 & \omega^2 - c^2 k^2 - \omega_p^2(1 - I_{33}) \end{Bmatrix} \begin{Bmatrix} E_1 \\ E_2 \\ E_3 \end{Bmatrix} = 0. \tag{4.13}$$

Focusing on the (x, y) -plane we consider a reduced distribution, the bi-Maxwellian $f_0(u, v) = \int f_0(u, v, w) dw$ whose level sets form ellipses in the (u, v) velocity plane. Take $\theta_v > \theta_u$ so that the semimajor axis of each ellipse is v -directed and the characteristic eccentricity is $e^2 = 1 - \theta_u^2/\theta_v^2$. To ensure separability of the resonant integrals I_{ij} , the (x, y) -plane is rotated through an angle φ , transforming velocities $(u, v) \rightarrow (v_{\parallel}, v_{\perp})$ such that the resonant denominator is $\omega - kv_{\parallel}$. By completing the square on v_{\perp} , the anisotropic Maxwellian of (4.12) in the reduced coordinates $(u, v) \rightarrow (v_{\parallel}, v_{\perp})$ is

$$f_0(v_{\parallel}, v_{\perp}) = \frac{1}{2\pi\theta_{\parallel}\theta_{\perp}} \exp\left(-\frac{v_{\parallel}^2}{2\theta_{\parallel}^2}\right) \exp\left(-\frac{(v_{\perp} - \alpha v_{\parallel})^2}{2\theta_{\perp}^2}\right), \tag{4.14}$$

where the rotated thermal and mean velocities are defined as

$$\theta_{\parallel}^2 \equiv \frac{(1 - e^2)\theta_u^2}{1 - e^2 \cos^2(\varphi)}, \quad \theta_{\perp}^2 \equiv \frac{\theta_u^2}{1 - e^2 \cos^2(\varphi)}, \quad \alpha \equiv \frac{e^2 \sin(\varphi) \cos(\varphi)}{1 - e^2 \cos^2(\varphi)}. \tag{4.15a-c}$$

Equation (4.14) shows that in the rotated frame the distribution is a shifted Maxwellian. That is, in the frame of a resonant particle the distribution has a mean velocity αv_{\parallel} transverse to the wavevector, as illustrated in figure 18. The off-diagonal integrals are non-zero, $I_{ij} \neq 0$, for anisotropic distributions as the apparent transverse wave current in the resonant particle frame couples the longitudinal and transverse wave components for propagation not aligned with the principal axes, even though there is no net current in the laboratory frame. In general all three components are coupled for non-principal propagation. This coupling is characteristic of anisotropy and contrasts with isotropic distributions for which the longitudinal plasma wave and the two transverse electromagnetic wave components have fully independent dispersion relations.

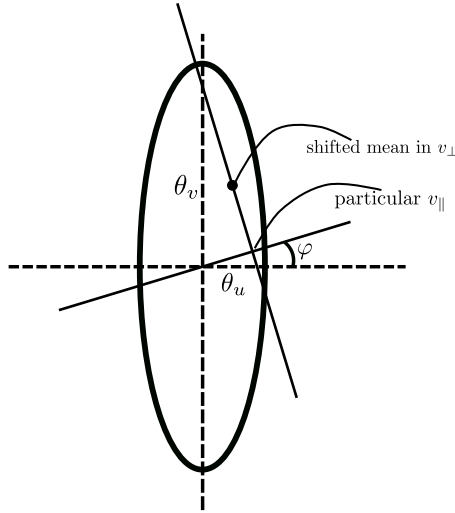


FIGURE 18. In the frame of reference of a particle propagating in a direction not aligned with the principal axes of an anisotropic distribution there is a mean drift velocity in the direction transverse to the particle’s motion which couples together the electromagnetic wave’s longitudinal and transverse components. In other words, in a frame where the velocity coordinates (u, v) are rotated through an angle φ into coordinates $(v_{\parallel}, v_{\perp})$, for a particular value of v_{\parallel} there is a non-zero mean value of v_{\perp} such that the off-diagonal integrals $I_{ij} \neq 0$ of (4.8).

To evaluate the integrals I_{11} , I_{12} and I_{22} for the distribution in (4.14) in the rotated coordinates, note the following integrals related to the plasma dispersion function $Z(\zeta)$:

$$\frac{1}{\sqrt{\pi}} \int_{-\infty}^{\infty} \frac{x}{\zeta - x} e^{-x^2/2a^2} dx = \frac{a}{2} Z'(\tilde{\zeta}), \tag{4.16}$$

$$\frac{1}{\sqrt{\pi}} \int_{-\infty}^{\infty} \frac{x^2}{\zeta - x} e^{-x^2/2a^2} dx = -\frac{a^2}{2} (Z''(\tilde{\zeta}) + 2Z(\tilde{\zeta})), \tag{4.17}$$

$$\frac{1}{\sqrt{\pi}} \int_{-\infty}^{\infty} \frac{x^3}{\zeta - x} e^{-x^2/2a^2} dx = \frac{a^3}{2^{3/2}} (Z'''(\tilde{\zeta}) + 6Z'(\tilde{\zeta})), \tag{4.18}$$

where $\tilde{\zeta} = \zeta/\sqrt{2}a$. These identities are found through integration by parts using the Hermite relation $\psi_n(x) = (d^n/dx^n)e^{-x^2/2}$ and the identity $Z'(\zeta) = -2(1 + \zeta Z(\zeta))$. With the gradient $\partial f/\partial v_{\parallel} = (-v_{\parallel}/\theta_{\parallel}^2 + \alpha(v_{\perp} - \alpha v_{\parallel})/\theta_{\perp}^2)f$ the integrals I_{ij} in (4.13) work out to

$$I_{11} = -\frac{1}{4} (Z'''(\tilde{\zeta}) + 6Z'(\tilde{\zeta})), \tag{4.19}$$

$$I_{12} = -\frac{\alpha}{4} (Z'''(\tilde{\zeta}) + 6Z'(\tilde{\zeta})), \tag{4.20}$$

$$I_{22} = -\frac{\alpha^2}{4} (Z'''(\tilde{\zeta}) + 2Z'(\tilde{\zeta})) - \frac{\theta_{\perp}^2}{\theta_{\parallel}^2} \frac{Z'(\tilde{\zeta})}{2}, \tag{4.21}$$

$$I_{33} = -\frac{\theta_w^2}{\theta_{\parallel}^2} \frac{Z'(\tilde{\zeta})}{2}, \tag{4.22}$$

where $\tilde{\zeta} \equiv \zeta/\sqrt{2}\theta_{\parallel}$. Let the angular eccentricity be $\gamma = \arcsin(e)$. The characteristic anisotropies are then $A_1 \equiv \theta_{\perp}^2/\theta_{\parallel}^2 - 1 = e^2/(1 - e^2) = \tan^2(\gamma)$ for the in-plane anisotropy and $A_2 \equiv \theta_w^2/\theta_{\parallel}^2 - 1$ for the binormal anisotropy. These two anisotropy parameters induce the electromagnetic Weibel instability to relax the anisotropy of their respective dimensions. For propagation along the principal axes, $\varphi \rightarrow 0, \pi/2$ the parameter $\alpha \rightarrow 0$, decoupling the \hat{x} - and \hat{y} -components as $I_{12} \rightarrow 0$ and $I_{22} \rightarrow -(\theta_v^2/\theta_u^2)(Z'(\zeta/\sqrt{2}\theta_u)/2)$ as in (4.22).

4.3.1. Dispersion function for the classic Weibel instability

Focusing on the decoupled component in (4.13), namely $\varepsilon_{33}E_3 = 0$, leads to

$$1 - \left(\frac{\tilde{\zeta}}{c}\right)^2 + \frac{1}{(k\lambda_c)^2} \left(1 + \frac{Z'(\tilde{\zeta})}{2} + A_2 \frac{Z'(\tilde{\zeta})}{2}\right) = 0 \quad (4.23)$$

with A_2 the binormal anisotropy. Equation (4.23) is valid for all propagation angles. For principal propagation at $\varphi = 0$ (the \hat{x} -direction) the principal anisotropies $A_1 = A_2$ such that (4.23) describes both the transverse and binormal components. It is instructive to observe that isotropy reduces (4.23) to the ordinary wave kinetic dispersion relation. The coupled branch of solutions to (4.13) is described by

$$\left(-\left(\frac{\tilde{\zeta}}{c}\right)^2 + \frac{1}{(k\lambda_c)^2}(1 - I_{11})\right) \left(1 - \left(\frac{\tilde{\zeta}}{c}\right)^2 + \frac{1}{(k\lambda_c)^2}(1 - I_{22})\right) - \frac{1}{(k\lambda_c)^4}I_{12}^2 = 0 \quad (4.24)$$

with transverse magnetic field out-of-plane and two components of electric field in-plane.

4.4. Single-mode saturation of Weibel instability in one spatial dimension

Just as electrostatic instability saturates by nonlinear trapping of near-resonant particles in an electric potential energy well, electromagnetic instability saturates by magnetic trapping. As a supplement to this section, Appendix D builds an analytic model of the phase portraits associated with ideal magnetic trapping and a conceptual model of magnetic trapping as a magnetic potential momentum well. Simulation of a single-mode Weibel instability by initialization with kinetic eigenfunctions allows one to self-consistently visualize the saturated phase space structures. The foundational simulations of an electromagnetic instability due to anisotropy considered Weibel instability evolving from the anisotropic Maxwellian using the particle-in-cell method (Davidson *et al.* 1972). Later, Califano, Pegoraro & Bulanov (1997) conducted one- and two-dimensional simulations in an inhomogeneous plasma using anisotropy induced by streaming beams. Building on this, Cagas *et al.* (2017) simulated single-mode Weibel saturation with a continuum-kinetic method using a zero-order counter-streaming electron beam distribution. In Cagas *et al.* (2017) an electrostatic streaming instability was proposed to explain the growth of a beam-axis directed electric field close to nonlinear saturation.

Zero-order beam distributions are often used because Weibel instability is induced in the laboratory by colliding high velocity plasmas (Hill *et al.* 2005; Fox *et al.* 2013; Huntington *et al.* 2015; Shukla *et al.* 2018). While zero-order beam distributions are inherently anisotropic they are also possibly unstable to electrostatic streaming instability. The possible introduction of electrostatic streaming instability can confuse and complicate an attempt to isolate Weibel instability. On the other hand, there is no possibility of streaming instability when the Weibel instability is induced by a zero-order anisotropic Maxwellian distribution. For this reason the anisotropic Maxwellian is considered here

using the continuum kinetic method, as originally considered with particle-in-cell method by Davidson *et al.* (1972).

4.4.1. Numerical method for single-mode Weibel instability simulation

We use the mixed spectral-DG method presented in Appendix A and Crews & Shumlak (2022), where the space coordinate is represented using Fourier modes and the two velocity dimensions are discretized with the DG method. The field equations are chosen as follows: Ampere's law and Faraday's law are used to evolve the transverse electrodynamic field, and Gauss's law is used to constrain the electric field along the axis of the wavevector. When considering only a single spatial coordinate, three field equations can be chosen in this way (one component each of the electrodynamic equations and Gauss's law) as there are only three field components.

The geometry is established by aligning the hot direction of the bi-Maxwellian with the y -coordinate, the growing magnetic field with the z -direction and perturbing the distribution function with wavenumber in the x -direction. This necessitates two dimensions of velocity, v_x in the x -direction and v_y in the y -direction, for a one space and two velocity dimensions (1D2V) phase space geometry. Phase space is discretized using $N_x = 100$ evenly spaced collocation nodes in the x -direction, and $N_{v_x} = N_{v_y} = 22$ finite elements in velocity, each of 11th polynomial order. Fourteen elements are evenly spaced between the velocity intervals $[-7, 7]v_t$, and four elements are evenly spaced within each interval $[-15, -7]v_t$ and $[7, 15]v_t$. A spatial hyperviscosity $10^{-4}\nabla_x^4 f$ is used to prevent spectral blocking by the turbulent cascade saturation. The field equations are discretized by a standard Fourier spectral method.

4.4.2. Initialization with field and phase space eigenfunctions

The characteristic parameters are chosen such that $v_t/c = 0.3$ and anisotropy $A = 3$ (or ratio $\theta_v/\theta_u = 2$) with the zero-order distribution given by (4.12) and the direction of propagation set to $\varphi = 0$. This is equivalent to using (4.23) for the dispersion function. Velocities are normalized to θ_u , time to ω_p^{-1} and lengths to $\lambda_D = \theta_u/\omega_p$. The domain length is then specified by the chosen wavenumber $k_x\lambda_D = 0.1$. Solution of (4.23) gives the eigenvalue of the problem as the phase velocity $\zeta/v_t = 1.23i$. The phase space perturbation is constructed using (4.5) for the phase space eigenfunction in the form

$$f_1(x, v_x, v_y) = \text{Re} \left\{ i \frac{\mathcal{A}}{k} \left(\frac{v_y}{\zeta - v_x} \frac{\partial f_0}{\partial v_x} + \frac{\partial f_0}{\partial v_y} \right) \exp(ikx) \right\}, \quad (4.25)$$

longitudinal field $E_{x1} = 0$ and the initial transverse electrodynamic fields by

$$B_{z1} = \text{Re} (\mathcal{A} \exp(ikx)), \quad (4.26)$$

$$E_{y1} = \text{Re} (\zeta \mathcal{A} \exp(ikx)), \quad (4.27)$$

where the amplitude is set to $\mathcal{A} = 10^{-3}$. This initial condition is consistent in the sense that the charge density is zero and the current density satisfies Ampere's law.

4.4.3. Fully nonlinear simulation results for single-mode Weibel saturation

The simulation is run until $t\omega_p = 100$ using the numerical method of § 4.4.1 with time step $\Delta t = 2.0 \times 10^{-3}$. The change in domain-integrated wave energies is shown in figure 19. Of note is the oscillating transverse electric field at saturation, and how longitudinal electric energy corrects from zero to trend with magnetic energy.

Figure 20 shows the time evolution of magnetic field and electron density in increments of $t\omega_p = 20$. As magnetic energy grows, electrons are progressively magnetically trapped

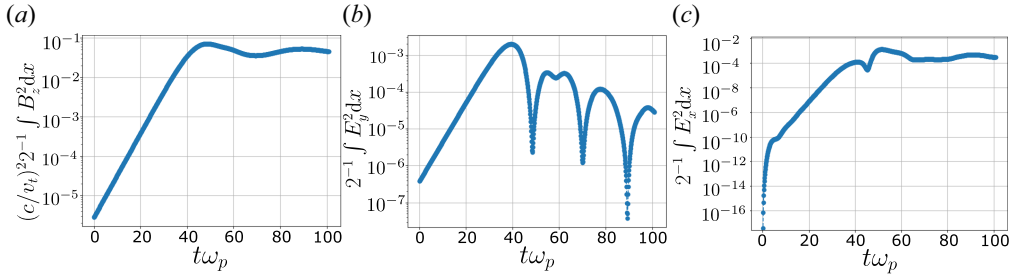


FIGURE 19. Growth of domain-integrated wave energies towards saturation of Weibel instability in one spatial dimension, namely (a) the magnetic energy, (b) the transverse electric energy of E_y and (c) the longitudinal electric energy of E_x , or energy along the axis of the wavevector. A nonlinear phase is reached at $t\omega_p = 40$, with peak magnetic energy around $t\omega_p = 50$. Longitudinal electric energy is observed to grow with a similar trend to the magnetic energy.

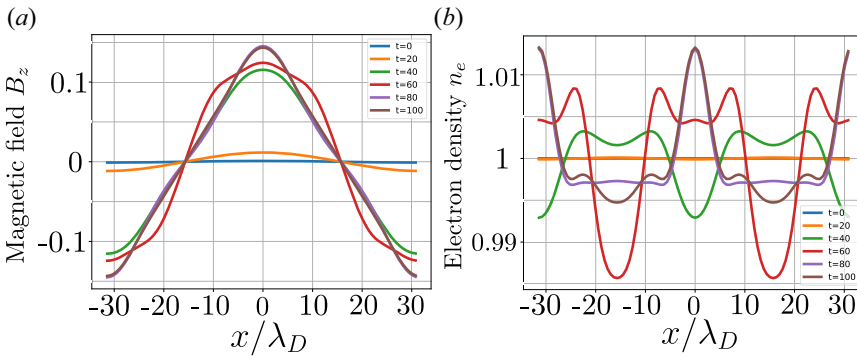


FIGURE 20. Evolution of (a) magnetic field $B_z(x)$ and (b) electron density $n_e(x)$, to nonlinear saturation of a single unstable Weibel mode. The mode saturates around $t\omega_p \approx 45$. Prior to saturation the magnetic field has a spectrum consisting of only even mode numbers with an apparent power law in logarithmic amplitudes. Since the function is clearly analytic this spectrum is consistent with an elliptic cosine function until nonlinear saturation. It is interesting that this higher-order phenomenon arises even from a single-mode eigenfunction perturbation. The electron holes at saturation are bounded by the maxima of magnetic energy $B^2/2\mu_0$, or equivalently bounded by the potential wells $A_y(x)$.

as described analytically in [Appendix D](#). With the initial free energy released, the distribution function attempts to evolve towards a function of the constants of motion, namely the energy $H = \frac{1}{2}m(v_x^2 + v_y^2) - e\Phi(x)$ and canonical momenta $P_y = mv_y - eA_y(x)$, $P_x = mv_x$ where $\Phi(x)$ is the electric potential and $A = A_y(x)\hat{y}$ is the magnetic vector potential. Specifically, trapped and passing phase space trajectories are determined by the equation (Morse & Nielson 1971)

$$mv_x = \sqrt{2m(H + e\varphi(x)) - (P_y + eA_y(x))^2}, \tag{4.28}$$

for a particle's energy $H = \frac{1}{2}m(v_{x0}^2 + v_{y0}^2) - e\varphi(x_0)$ and momentum $P_y = mv_{y0} - eA_{y0}(x_0)$ constants. [Figure 21](#) visualizes the phase space structure at nonlinear saturation by an isocontour of the distribution at 10% of its maximum. Trapped and passing trajectories

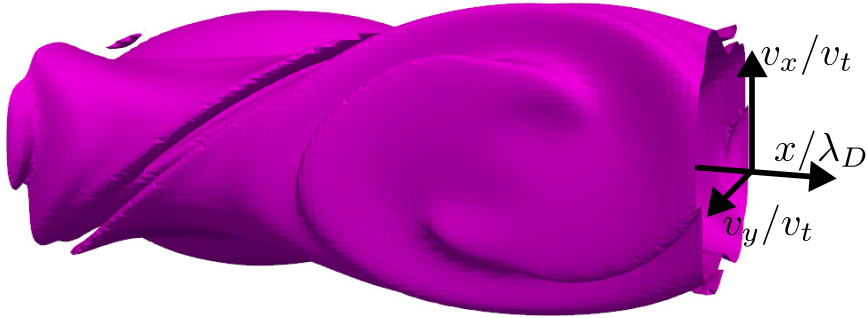


FIGURE 21. Phase space vortex shown by contour at $0.1 \max(f)$ in the coordinates (x, v_x, v_y) at saturation of a single Weibel mode. The mid-domain x -coordinate corresponds to $x = 0$. The magnetic trapping phase space vortex is distinguished from the electrostatic vortex as velocity-dependent since the momentum p_y in (4.28) is linear in v_y . In this way the single-mode phase space vortex is antisymmetric, with trapped and passing orbits swapping under $v_y \rightarrow -v_y$. For this reason there is no magnetic trapping along the $v_y = 0$ plane.

are seen at the right- and left-hand of the figure, respectively, for $v_y > 0$. Trapped trajectories circulate within a phase space vortex while passing trajectories execute motion in the vicinity of the separatrix. Upon inversion of the transverse velocity, $v_y \rightarrow -v_y$, the positions of the trapped trajectories and passing trajectories are inverted, $x \rightarrow -x$.

Linear electrostatic instability is not possible due to the zero-order anisotropic Maxwellian, so here we explain the growth of electrostatic energy observed both here and in Cagas *et al.* (2017) as a second-order phenomenon arising from space-charge-generating filamentation (that is, the magnetic-trapping electron holes of figure 20). While saturated filaments can be understood intuitively as electron holes, the progressive development of longitudinal electric energy in the linear phase can be understood as mode coupling of the longitudinal field to the transverse field at second order in the transverse dynamic field (Taggart *et al.* 1972). Appendix D presents a visual description of the density filamentation phenomenon as resulting from a bifurcation in phase space topology as the thermal trapping parameter mv_{th}/eA_{max} passes through unity. When $eA_{max} \ll mv_{th}$ the primary phase space vortex structures are antisymmetric across the v_y -plane, producing a perturbation in current density without a perturbation in charge density. Once $eA_{max} \approx mv_{th}$ particle orbits with low P_y become more symmetric across the v_y -plane and produce a coherent perturbation in the density.

Thus, both electric and magnetic field trapping are associated with local variations in the electron density which manifests as space charge. In the case of magnetic trapping the charge density is a higher-order effect, and the first-order effect is production of electric currents to sustain the magnetic mode. The development of space charge from magnetic pressure is anticipated in Morse & Nielson (1971), and the longitudinal field is explained in Taggart *et al.* (1972) to arise at second order from the coupling of two magnetic modes. Dynamic space charge, or filamentation, has been observed in modelling to modify growth rates, in both early and more recent studies (Taggart *et al.* 1972; Tzoufras *et al.* 2006), pointing to the importance of higher-order effects prior to saturation. Since the fraction of trapped electrons is proportional to the magnetic energy, with saturation when the characteristic magnetic bounce frequency reaches the growth rate (Davidson *et al.* 1972), it follows that longitudinal electric field should trend nonlinearly with the magnetic field. Finally, the theory of Appendix D interprets the density perturbation as arising from particles with $v_y \approx 0$ and energies $H < (eA_{max})^2/2m$.

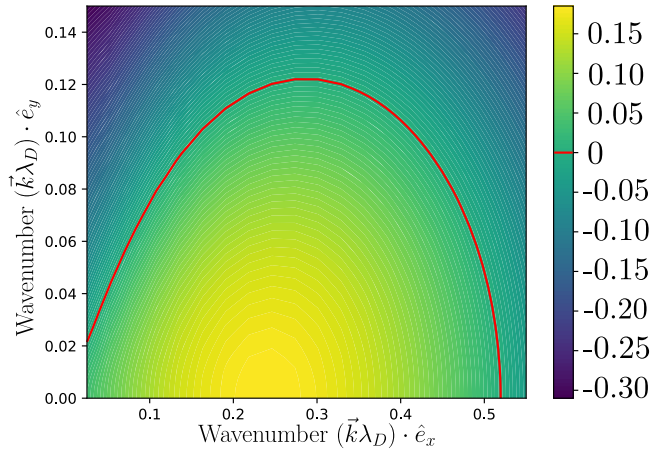


FIGURE 22. Growth rates of multidimensional Weibel instability as $\text{Im}(\omega)/\omega_{pe}$ for an anisotropic bi-Maxwellian of anisotropy $A = 3$ where the electric field is assumed to lie in the (x, y) -plane and the first-order transverse magnetic field to be out-of-plane. The higher-temperature direction is assumed to lie in the \hat{y} -direction assuming $v_t/c = 0.3$. The red line identifies marginal stability.

4.5. Saturation of many unstable Weibel modes in two spatial dimensions

Weibel instability of a homogeneous unmagnetized plasma is inherently multidimensional as wavevectors oblique to the principal anisotropy axes have comparable growth rates to the principal axes (similar to the multidimensional streaming instability studied in § 2.7). We consider for example the branch of the dispersion function for the anisotropic Maxwellian given by (4.24) with transverse magnetic field out-of-plane and the longitudinal and transverse electric fields in-plane. The out-of-plane magnetic field allows a reduced 2D2V phase space geometry for tractable continuum-kinetic simulation (Skoutnev *et al.* 2019). It should be kept in mind that the instability dynamics are truly three-dimensional just as in the multidimensional Langmuir turbulence simulation of § 2.7. Figure 22 plots the growth rate as a function of the wavevector $\mathbf{k} = k_x\hat{x} + k_y\hat{y}$ of the unstable branch of (4.24) for a zero-order bi-Maxwellian of anisotropy $A = 3$ and with $v_t/c = 0.3$. If the destabilized ordinary wave studied in § 4.4 were included in the simulation, the magnetic field would also take in-plane components, necessitating a third velocity dimension. We point out the same caveats for this simulation as for the two-dimensional two-stream simulation; the nonlinear phase space dynamics are likely similar to the three-dimensional problem, but the nonlinear dynamics of the saturated state (that is, the turbulence statistics) will likely be different. The essence of the problem lies in restricting the cylindrical symmetry of the near-maximal-growth-rate modes about the principal anisotropy axis to a plane. Fully three-dimensional simulations are necessary to clarify these issues.

4.5.1. Numerical methods for the two-dimensional multimode Weibel instability

The simulations are conducted with the methods of Appendix A and Crews & Shumlak (2022) with a few key differences. Specifically, Ampere's and Faraday's laws are used for the field equations which are time-integrated in Fourier spectral space with the same third-order Adams–Bashforth method as the kinetic equation. There is also an important difference in initialization of the unstable modes. In the Vlasov–Poisson system the field part of the kinetic eigenfunctions is described by the scalar potential, yet in the

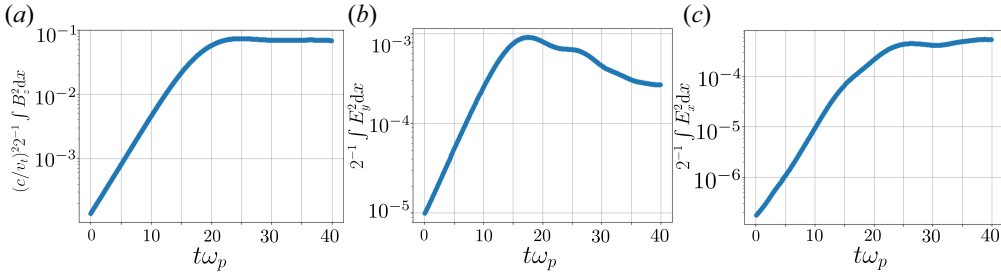


FIGURE 23. Evolution of domain-integrated energy for (a) the out-of-plane magnetic field B_z , (b) the electric field transverse to the maximum growth-rate axis and (c) the electric field parallel to that axis (formerly the longitudinal field of the one-dimensional simulation). A difference from the one-dimensional simulation is a steadily decreasing transverse electric energy rather than a coherent oscillation after saturation time. The \hat{x} -directed electric energy increases at a rate faster than the growth of the linear modes due to the same space charge effects as in the single-mode simulation discussed in § 4.4.

multidimensional Vlasov–Maxwell system the kinetic eigenfunctions consist of a vector self-consistent field-plasma configuration. Initialization with kinetic eigenfunctions in an electrodynamic problem necessitates solving the eigenvalue problem $\chi \mathbf{E} = \zeta^2 \mathbf{E}$ in the wavevector frame, as discussed in § 4.2. In our implementation, the eigenfunctions are computed in the rotated wavevector frame and then antirotated back into the (x, y) -plane with components $\mathbf{E} = E_x \hat{x} + E_y \hat{y}$. Thus, for each desired pair of wavenumbers (k_x, k_y) a perturbation is applied as

$$f_1 = \mathcal{A} \text{Re} \left[\frac{q}{i\omega} \left\{ E_x \left(\frac{\partial f_0}{\partial u} + \frac{v_x (\mathbf{k} \cdot \nabla_u f_0)}{\omega - \mathbf{k} \cdot \mathbf{v}} \right) + E_y \left(\frac{\partial f_0}{\partial v} + \frac{v_y (\mathbf{k} \cdot \nabla_u f_0)}{\omega - \mathbf{k} \cdot \mathbf{v}} \right) \right\} e^{i(\mathbf{k} \cdot \mathbf{x} + \tilde{\varphi})} \right] \quad (4.29)$$

with $\tilde{\varphi}$ a randomly chosen phase shift per wavevector and the amplitude $\mathcal{A} = 2 \times 10^{-3}$. The magnetic field is then initialized as $B_z = \zeta^{-1} \hat{k} \times \mathbf{E}$ where ζ is the eigenvalue. A higher amplitude than the one-dimensional problem is chosen to reduce time to saturation.

4.5.2. Initial conditions for the two-dimensional Weibel instability simulations

The domain is specified by fundamental wavenumbers $k_x \lambda_D = 0.125$ and $k_y \lambda_D = 0.01$. Physical space is represented with $N_x = 32$ and $N_y = 128$ evenly spaced collocation points, while velocity space is represented as a Cartesian tensor product of linear finite elements with 11 finite elements per velocity axis, each linear element of seventh-order polynomial basis for $(v_x, v_y) \in [-11, 11] \theta_u$. As in § 2.7 many modes are excited; for each of the first two harmonics of the fundamental wavenumber, namely $n k_x \lambda_D$ with $n = 1, 2$, five transverse wavenumbers $\pm m k_y \lambda_D$ are excited with $m = 0, 1, 2$. The normalized thermal velocity $v_t/c = 0.3$ and the anisotropy is $A = 3$, as in the one-dimensional problem. The simulation is run to $t\omega_p = 40$ using a time step of $\Delta t = 8 \times 10^{-3}$ with an added hyperviscosity $\nu \nabla_x^4 f$ with $\nu = 1$ to prevent spectral blocking. Due to the hyperviscosity total energy is conserved only to $O(10^{-4})$ by the simulation stop time.

4.5.3. Nonlinear simulations of the two-dimensional Weibel instability

The problem described in § 4.5.2 was simulated using the methods of § 4.5.1. Figure 23 shows the energy traces of the electrodynamic field during the linear phase and beyond instability saturation. Nonlinear saturation occurs around $t\omega_p = 17$, as gauged by the

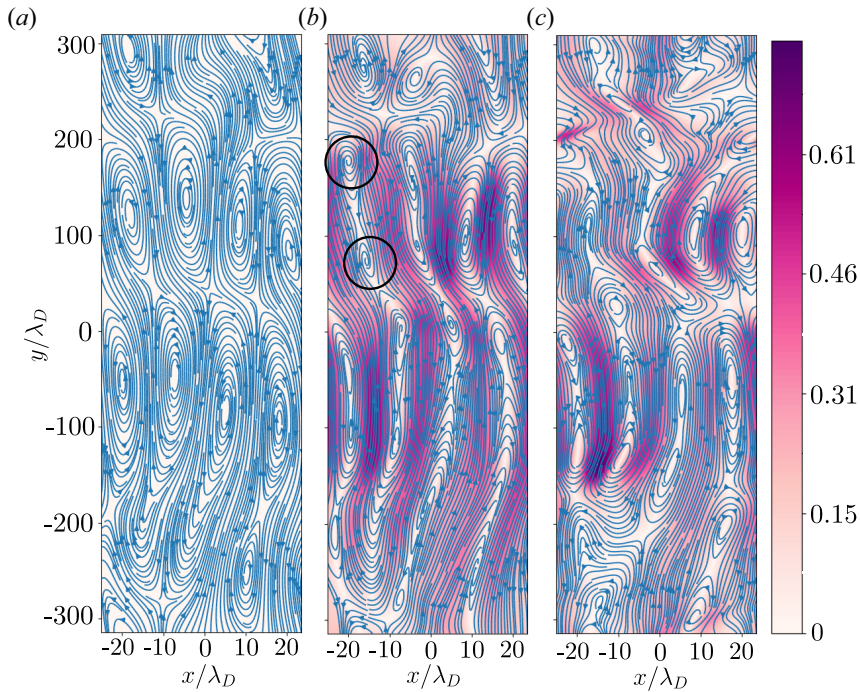


FIGURE 24. Evolution of current at times (a) $t\omega_p = 0$, (b) $t\omega_p = 25$ and (c) $t\omega_p = 39.5$. Plotted are streamlines of \mathbf{j} and its magnitude $|\mathbf{j}|$ as filled contours. Current tends to form closed paths at long wavelength in y . The indicated spiral vortices in the streamlines demonstrate rapid local space charge production ($\nabla \cdot \mathbf{j} \neq 0$) as expected from the filamentation and trapping dynamics of the one-dimensional problem. The large circulating configuration space electron current vortices manifest on small scales as counter-propagating electron streams which sustain a train of magnetic-trapping electron phase space vortices. In this unmagnetized model problem, these structures isotropize from four-dimensional phase space dynamics.

\hat{y} -directed transverse electric field. The \hat{x} -directed electric field energy follows a similar trend as the one-dimensional problem, its growth composed of two effects: to first-order from the initialized oblique modes, and to second-order in the magnetic field as discussed in § 4.4. At nonlinear saturation, magnetic-trapping electron holes form between the counter-streaming mean flows.

Figure 24 illustrates the dynamics of the multidimensional instability through streamlines of the current density $\mathbf{j}(x, y)$ and filled contours of its magnitude for three times in the simulation output. Trigonometric interpolation is used to visualize the current density by zero-padding the spectrum and inverse Fourier transformation, as the spectrum is properly resolved up to the chosen spectral cutoff. In figure 24(b) one can observe spiral current streamlines indicating the local production of space charge as the electron density filaments into two-dimensional analogues of the magnetic-trapping electron holes studied in the single-mode problem, also observed in Califano *et al.* (1997). By the simulation's end, nonlinear mixing has caused some of the filaments to rotate, as in the multidimensional electrostatic problem considered in § 2.7, indicating a similar isotropization on averaged scales. Inspection of figure 25, which plots the spatially averaged distribution function $(f)_{(x,y)}(v_x, v_y)$ at $t\omega_p = 0$ and $t\omega_p = 40$ in figure 25(a,b) and in figure 25(c) the trace of the anisotropy parameter A , shows the anisotropic

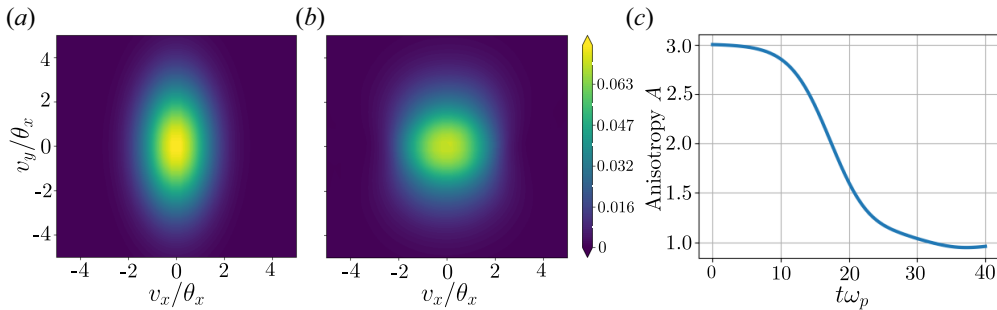


FIGURE 25. The relaxing spatially averaged distribution function $\langle f \rangle_{(x,y)}(v_x, v_y)$ shown at two times: (a) the initial condition $t\omega_p = 0$, (b) the stop-time $t\omega_p = 40$ and in addition (c) the time evolution of the anisotropy parameter $A = \langle v_y^2 \rangle / \langle v_x^2 \rangle - 1$. The turbulence of magnetic trapping phase space vortices in the turbulent currents of the saturated instability isotropizes the distribution function. Note that $A = 0$ would indicate isotropy, so that the saturated state consists of persistent anisotropy coexisting with the wave field (Davidson *et al.* 1972).

Maxwellian to relax towards isotropy through Weibel-induced turbulence. The initial anisotropy $A = 3$ is observed to decrease monotonically until at saturation $A \approx 1$, meaning that the saturated state is weakly anisotropic. This persistent anisotropy coexists with the fluctuating filamentation currents, consistent with the observations of Davidson *et al.* (1972). Indeed, persistent anisotropy accompanying sheared flows in the saturated state is expected for collisionless dynamics (Del Sarto & Pegoraro 2017).

5. General discussion and summary

This work advocates for the application of kinetic eigenfunctions to initialize Vlasov–Poisson, Vlasov–Maxwell and quasilinear kinetic simulations. It reviews linearized kinetic theory and presents example simulations of the most commonly treated model problems. The historical discussion of § 2 reviews the kinetic eigenvalue and initial-value problems, and highlights that the instabilities identified by Landau’s initial-value analysis are indeed true eigenfunctions which may be utilized as simulation perturbations. Perturbation of a kinetic problem using its eigenfunctions provides several benefits, such as a controlled partition of perturbation energy, initialization of perturbations at close-to-nonlinear amplitudes and measurement of linear instability growth rates up to machine precision unpolluted by linear Landau damping activity.

Notable findings for researchers utilizing kinetic theory and simulation include the following.

- (i) A historical overview of eigenfunctions for the Vlasov–Poisson system (§ 2.1).
- (ii) Worked examples of eigenfunction initialization for the Vlasov–Poisson and Vlasov–Maxwell systems to illustrate the method’s advantages (§ 2.5.1, single-mode two-stream; § 2.7, two-dimensional multimode two-stream; § 3.6, single-mode loss-cone; § 4.4, single-mode Weibel; § 4.5, two-dimensional multimode Weibel).
- (iii) Eigenfunction initialization of quasilinear kinetic simulations (§ 2.8 as applied to quasilinear bump-on-tail dynamics) for which the phase space fluctuation is always an eigenfunction of the instantaneous state.
- (iv) Power series representations of the dielectric function for ring distributions in strongly magnetized plasmas at arbitrary propagation angles (§ 3.3 and Appendix B).

- (v) Closed form hypergeometric and trigonometric integral representations of the dielectric for ring distributions in strongly magnetized plasmas (§ 3.4 and Appendix C.1).
- (vi) Helical geometry of phase space fluctuations in magnetized plasmas (§ 3.5).
- (vii) Description of the generation of electron density holes by magnetic trapping in the saturating Weibel instability (§ 4.4.3 and Appendix D) occurring without invoking electrostatic streaming effects as hypothesized in Cagas *et al.* (2017).

This work is by no means an exhaustive overview of the possible applications of kinetic eigenfunctions. Indeed, many other applications are noted in § 1. Nevertheless, a few notable problems are demonstrated here to significantly benefit from eigenfunction initialization. Namely, the electrostatic problem in a static magnetic field is treated in detail for ring distributions, and new analytic results for the ring dielectric function are presented. Nonlinear saturation of the multidimensional Weibel instability of an anisotropic Maxwellian, originally treated by Davidson *et al.* (1972) with the particle-in-cell method, is revisited and new light shed with a phase portrait analysis and nonlinear continuum-kinetic simulations. However, a simple and important model problem is left for future work, namely anisotropy-induced field-parallel whistler emission.

A few further notes are in order regarding the importance of phase space eigenfunctions in numerical plasma theory. In this work the emphasis is on observing the evolution of strongly unstable linear eigenfunctions into nonlinear structures. Another important class of problems are the weakly unstable distributions that are commonly treated by QLT. In numerical solutions of QLT there is no transition to nonlinear structures and the phase space dynamics of the obtained spectra are necessarily linear eigenfunctions. As another way of phrasing this, one can say that in weak turbulence the linear eigenfunctions contain most of the fluctuation energy. The application of kinetic phase space eigenfunctions to numerically study QLT potentially offers a multitude of interesting and valuable avenues of further exploration.

Acknowledgements

The authors would like to thank J.B. Coughlin, I.A.M. Datta, A. Ho, E.T. Meier, A.D. Stepanov, Y. Takagaki, W.H. Thomas and G.V. Vogman for helpful discussions. The authors would also like to thank the anonymous peer-reviewers for their extensive and essential assistance with revision of the manuscript.

Editor F. Califano thanks the referees for their advice in evaluating this article.

Funding

The information, data, or work presented herein was funded in part by the Air Force Office of Scientific Research under award no. FA9550-15-1-0271. This material is based upon work supported by the National Science Foundation under grant no. PHY-2108419.

Declaration of interests

The authors report no conflict of interest.

Appendix A. General description of our numerical methods

Our numerical method is a combination of the pseudospectral method for spatial fluxes (Boyd 2001) with high-order DG method for velocity space (Crews & Shumlak 2022). The Vlasov–Poisson system is discretized in configuration space by Galerkin projection onto a truncated multidimensional Fourier basis, for example $(x, y) \rightarrow (k_n, k_m)$. That is, if the

original kinetic equation is

$$\partial_t f + \mathbf{v} \cdot \nabla_x f + \mathbf{F} \cdot \nabla_v f = 0 \quad (\text{A1})$$

with \mathbf{F} the vector of momentum fluxes, then the Galerkin-projected kinetic equation is

$$\frac{\partial f_{nm}}{\partial t} + ik_n u f_{nm} + ik_m v f_{nm} + \nabla_v \cdot (\mathcal{F}_{nm}) = 0 \quad (\text{A2})$$

with \mathcal{F}_{nm} the vector of spectral momentum fluxes. Equation (A2) is discretized by truncating the velocity domain and applying the DG method $(u, v) \rightarrow (u_{jk}, v_{pq})$, with (j, p) the element indices and (k, q) the subelement indices (that is, the collocation nodes) and a set of basis functions ψ_k are chosen. We use the Legendre–Gauss–Lobatto basis (Hesthaven & Warburton 2007). The semidiscrete equation obtained is

$$\frac{df_{nmjpkq}}{dt} = \mathcal{N}_{nmjpkq}[f] + \mathcal{L}_{nmjpkq}^{\ell r} f_{nmj\ell pr}, \quad (\text{A3})$$

where \mathcal{N} is a nonlinear operator representing the discretized velocity flux divergences, while \mathcal{L} is the advective part of the semidiscrete operator and is linear in f . Advection is not linear in \mathbf{v} , but is integrated over the basis functions ψ_k to form a linear operator

$$\mathbb{T}_{nj k}^{\ell} \equiv -ik_n (\bar{v}_j I_k^{\ell} + \mathbf{J}_m \langle \psi_k | \psi^s \rangle^{-1} \langle \xi \psi_s | \psi^{\ell} \rangle), \quad (\text{A4})$$

with $\langle \cdot | \cdot \rangle$ an inner product over the reference element with coordinate $\xi \in [-1, 1]$, and \bar{v}_j the velocity in the midpoint of element j with transformation $v_j(\xi) = \bar{v}_j + (\Delta v)_j \xi / 2$ with $(\Delta v)_j$ the element width. Then advection is represented by a linear operator

$$\mathcal{L}_{nmjpkq}^{\ell r} f_{nmj\ell pr} \equiv \mathbb{T}_{nj k}^{\ell} f_{nmj\ell pq} + \mathbb{T}_{mp q}^r f_{nmj k pr}. \quad (\text{A5})$$

Poisson's equation is solved algebraically in Fourier space, and the velocity fluxes \mathcal{N} are computed by the pseudospectral method. That is, the spectral field and distribution are both zero-padded using Orszag's two-thirds rule and transformed to nodal values on the spatial collocation points where the fluxes are calculated. The velocity element boundary fluxes are then calculated in (\mathbf{x}, \mathbf{v}) space by an upwind method and transformed back to spectral space for time integration. However, element-internal fluxes are calculated in (\mathbf{k}, \mathbf{v}) space by inverse transformation as the spectral symmetry from $\text{Im}(f(\mathbf{x}, \mathbf{v})) = 0$ reduces the operations by a factor of two. Finally, the semidiscrete equation is advanced through $\Delta t = h$ using second-order Strang splitting of linear \mathcal{L} and nonlinear \mathcal{N} fluxes,

$$f^{n+1} = \mathcal{S}[\mathcal{L}]^{h/2} \mathcal{S}[\mathcal{N}]^h \mathcal{S}[\mathcal{L}]^{h/2} f^n, \quad (\text{A6})$$

where $\mathcal{S}[\cdot]$ represents evaluation of the separated operator by any method of approximation. In this simulation the explicit third-order Adams–Bashforth method is used for the nonlinear flux $\mathcal{S}[\mathcal{N}]^h$ while advection is advanced implicitly by Crank–Nicholson stepping,

$$(\mathcal{S}[\mathcal{L}]^h)^{\ell r}_{nmjpkq} = \left(I_{nj k}^{\ell} - \frac{h}{2} \mathbb{T}_{nj k}^{\ell} \right)^{-1} \left(I_{nj k}^{\ell} + \frac{h}{2} \mathbb{T}_{nj k}^{\ell} \right) \left(I_{mp q}^r - \frac{h}{2} \mathbb{T}_{mp q}^r \right)^{-1} \left(I_{mp q}^r + \frac{h}{2} \mathbb{T}_{mp q}^r \right) \quad (\text{A7})$$

with I_{mpq}^r the identity matrix I_q^r for each (m, n) . Fractional stepping for advection is advantageous as it reduces the $O(N^2)$ operations per cell into two $O(N)$ operations. The

calculation of the nonlinear momentum flux operator \mathcal{N} is treated in Crews (2022), and we briefly recapitulate this here. In this work, the quadratically nonlinear fluxes are not integrated consistently as described in Crews (2022, §2.5) and Hakim & Juno (2020), and instead an alias error is incurred. Consistent integration of the quadratically nonlinear fluxes in discretization of the Vlasov equation greatly improves the conservation of Casimirs (nonlinear functionals) such as phase space entropy density. However, in this work an alias error is accepted because the smoothing spatial hyperviscosity used here breaks the Casimirs near the aliased grid scales. Thus, inaccuracy in conservation of nonlinear functionals is accepted in exchange for less computational effort.

Appendix B. Polar Fourier integrals of ring distributions

This appendix integrates the ring distribution of (3.17) over perpendicular velocities,

$$\mathbb{F}_{n,m,\gamma}(k) \equiv \int_0^\infty f_\gamma(v) J_n(kv) J_m(kv) 2\pi v \, dv, \tag{B1}$$

for integer n, m . By this formula one can also determine the integral of products, $J_n(v) J'_n(v)$, etc., by recursion of the derivatives $J'_n(z)$. The result is that (B1) is a type- ${}_3F_3$ hypergeometric function,

$$\begin{aligned} \mathbb{F}_{n,m,\gamma}(k) &= \frac{\Gamma\left(\gamma + \frac{n+m}{2} + 1\right) (k\alpha)^{n+m}}{\Gamma(n+1)\Gamma(m+1)\Gamma(\gamma+1)} \\ &\times {}_3F_3\left[\begin{matrix} \frac{n+m}{2} + \frac{1}{2}, \frac{n+m}{2} + 1, \gamma + \frac{n+m}{2} + 1 \\ n+1, m+1, n+m+1 \end{matrix} \middle| -(2k\alpha)^2\right] \end{aligned} \tag{B2}$$

which is equivalently written as a power series with Gamma function coefficients,

$$\mathbb{F}_{n,m,\gamma}(k) = \frac{1}{\Gamma(\gamma+1)} \sum_{\ell=0}^\infty \frac{\Gamma(n+m+2\gamma+2\ell+1)}{\Gamma(n+\ell+1)\Gamma(m+\ell+1)\Gamma(n+m+\ell+1)} \frac{(-1)^\ell}{\ell!} (k\alpha)^{2\ell+n+m}. \tag{B3}$$

Setting $n = m$ as in electrostatic theory reduces to a more manageable ${}_2F_2$ function,

$$\mathbb{F}_{n,\gamma}(k) = \frac{\Gamma(\gamma+n+1)(k\alpha)^{2n}}{\Gamma^2(n+1)\Gamma(\gamma+1)} {}_2F_2\left[\begin{matrix} n + \frac{1}{2}, \gamma + n + 1 \\ n + 1, 2n + 1 \end{matrix} \middle| -(2k\alpha)^2\right] \tag{B4}$$

with the power series for practical computation given in (3.21).

B.1. The product of integer-order Bessel functions

The product of integer-order Bessel functions is a generalized ${}_2F_3$ -type hypergeometric,

$$J_n(z) J_m(z) = \frac{1}{n!m!} \left(\frac{z}{2}\right)^{n+m} {}_2F_3\left[\begin{matrix} \frac{n+m}{2} + \frac{1}{2}, \frac{n+m}{2} + 1 \\ n+1, m+1, n+m+1 \end{matrix} \middle| -z^2\right] \tag{B5}$$

which for $n = m$ reduces to a type ${}_1F_2$ function,

$$J_n^2(z) = \frac{1}{(n!)^2} \left(\frac{z}{2}\right)^{2n} {}_1F_2\left[\begin{matrix} n + \frac{1}{2} \\ n+1, 2n+1 \end{matrix} \middle| -z^2\right]. \tag{B6}$$

B.1.1. *Demonstration of (B5)*

Multiplying term-by-term the power series of J_n , J_m and diagonalizing by $\ell = j + k$,

$$\begin{aligned} J_n(z)J_m(z) &= \left(\frac{z}{2}\right)^{n+m} \sum_{j,k=0}^{\infty} \frac{1}{\Gamma(n+k+1)\Gamma(m+j+1)} \frac{(-z^2/4)^{j+k}}{j!k!} \\ &= \left(\frac{z}{2}\right)^{n+m} \sum_{\ell=0}^{\infty} \left[\sum_{k=0}^{\ell} \frac{1}{\Gamma(k+n+1)\Gamma(\ell-k+m+1)\Gamma(\ell-k+1)\Gamma(k+1)} \right] \left(\frac{-z^2}{4}\right)^{\ell}. \end{aligned} \tag{B7}$$

Using properties of Pochhammer symbols and Gauss’s hypergeometric theorem,

$$\begin{aligned} &\sum_{k=0}^{\ell} \frac{1}{\Gamma(k+n+1)\Gamma(\ell-k+m+1)\Gamma(\ell-k+1)\Gamma(k+1)} \\ &= \frac{1}{\Gamma(n+1)\Gamma(\ell+1)\Gamma(\ell+m+1)} {}_2F_1 \left[\begin{matrix} -\ell, -\ell-m \\ n+1 \end{matrix} \right] (1) \\ &= \frac{\Gamma(n+m+2\ell+1)}{\Gamma(\ell+1)\Gamma(m+\ell+1)\Gamma(n+\ell+1)\Gamma(n+m+\ell+1)} \end{aligned} \tag{B8}$$

one obtains a single summation for $J_n(z)J_m(z)$,

$$J_n(z)J_m(z) = \left(\frac{z}{2}\right)^{n+m} \sum_{\ell=0}^{\infty} \frac{\Gamma(n+m+2\ell+1)}{\Gamma(m+\ell+1)\Gamma(n+\ell+1)\Gamma(n+m+\ell+1)} \frac{(-z^2/4)^{\ell}}{\ell!}. \tag{B9}$$

The numerator factorial is then written in Pochhammer symbols by the formulae

$$(x+\ell)_{\ell} = \frac{(x)_{2\ell}}{(x)_{\ell}}, \tag{B10}$$

$$(x)_{2\ell} = 2^{2\ell} \left(\frac{x}{2}\right)_{\ell} \left(\frac{1+x}{2}\right)_{\ell}, \tag{B11}$$

yielding a series identical to (B5) and proving the identity,

$$J_n(z)J_m(z) = \frac{1}{n!m!} \left(\frac{z}{2}\right)^{n+m} \sum_{\ell=0}^{\infty} \frac{\left(\frac{n+m}{2} + \frac{1}{2}\right)_{\ell} \left(\frac{n+m}{2} + 1\right)_{\ell}}{(m+1)_{\ell}(n+1)_{\ell}(n+m+1)_{\ell}} \frac{(-z^2)^{\ell}}{\ell!}. \tag{B12}$$

B.2. *Integration of (B5) with a loss-cone distribution*

Having developed the product of two Bessel functions in terms of a single entire function the integration over perpendicular velocities is now shown to be (B2).

B.2.1. Demonstration of (B2)

The ring distribution $f_\gamma(v)$ is combined with (B12) and integrated term-by-term,

$$\mathbb{F}_{n,m,\gamma}(k) = \frac{k^{n+m}}{n!m!\gamma!(\alpha^2)^{\gamma+1}} \left(\frac{k}{2}\right)^{n+m} \sum_{\ell=0}^{\infty} \frac{\left(\frac{n+m}{2} + \frac{1}{2}\right)_\ell \left(\frac{n+m}{2} + 1\right)_\ell}{(m+1)_\ell(n+1)_\ell(n+m+1)_\ell} \frac{(-k^2)^\ell}{\ell!} \times \int_0^\infty v^{2(\ell+\gamma+(n+m)/2)} e^{-v^2/\alpha^2} 2v \, dv. \tag{B13}$$

The interior integral is Euler’s form of the Gamma function upon substitution $u = v^2/\alpha^2$,

$$\mathbb{F}_{n,m,\gamma} = \frac{\Gamma\left(\gamma + \frac{n+m}{2} + 1\right)}{\Gamma(n+1)\Gamma(m+1)\Gamma(\gamma+1)} (k\alpha)^{n+m} \times \sum_{\ell=0}^{\infty} \frac{\left(\frac{n+m}{2} + \frac{1}{2}\right)_\ell \left(\frac{n+m}{2} + 1\right)_\ell \left(\gamma + \frac{n+m}{2} + 1\right)_\ell}{(m+1)_\ell(n+1)_\ell(n+m+1)_\ell} \frac{(-4\alpha^2 k^2)^\ell}{\ell!}. \tag{B14}$$

The series is a hypergeometric function of type- ${}_3F_3$, demonstrating (B2). While the form of the integral as a type- ${}_3F_3$ function reveals connections to the theory of special functions, in a practical computation it is more practical to use the Gamma function form of the series as in (B3).

Appendix C. The Harris dispersion function for ring distributions

This appendix demonstrates (3.25) and (3.26) for electrostatic modes in a plasma with zero-order cyclotron orbits distributed as a loss-cone, beginning from (3.9) known as the Harris dispersion function. We begin by constructing the function in closed form as a hypergeometric function, and then consider a convenient trigonometric integral form by calculation of the loss-cone’s Hankel transform. These forms of the dielectric function $\varepsilon(\omega, k_\perp)$, which sum the contribution of the cyclotron resonances to all orders, enable precise numerics to determine eigenvalues in continuum kinetic simulations.

C.1. The perpendicular wave dielectric function in closed form

We demonstrate (3.25) for the closed form of the dielectric function for perpendicular cyclotron waves in a loss-cone distributed plasma using the Lerche–Newberger summation theorem (Lerche 1974; Newberger 1982), which sums the Bessel series in (3.7) and (3.8) to all orders in the cyclotron harmonics,

$$\mathcal{Y}_2 = \sum_{n=-\infty}^{\infty} \frac{n}{\omega' - n} J_n^2(\beta) = \frac{\pi\omega'}{\sin(\pi\omega')} J_{\omega'}(\beta) J_{-\omega'}(\beta) - 1, \tag{C1}$$

$$\mathcal{A}_2 = \sum_{n=-\infty}^{\infty} \frac{1}{\omega' - n} J_n^2(\beta) = \frac{\pi}{\sin(\pi\omega')} J_{\omega'}(\beta) J_{-\omega'}(\beta), \tag{C2}$$

with each sum limiting to a product of Bessel functions $J_z(\beta)J_{-z}(\beta)$ of complex order. Here the auxiliary quantities are $\omega' = (\omega - k_\parallel v_\parallel)/\omega_c$ and $\beta = k_\perp v_\perp/\omega_c$. The polar

velocity-space integrals over v_{\perp} , when considering the closed forms of (C1) and (C2), result in a generalized hypergeometric function (see the following for a demonstration),

$$\frac{1}{2^{\gamma} \alpha^{2\gamma+2} \Gamma(\gamma+1)} \int_0^{\infty} v^{2j+1} e^{-v^2/2\alpha^2} \frac{\pi\omega}{\sin(\pi\omega)} J_{\omega}(qv) J_{-\omega}(qv) dv = {}_2F_2 \left[\begin{matrix} \frac{1}{2}, & \gamma+1 \\ 1+\omega, & 1-\omega \end{matrix} \right] (-2(\alpha q)^2). \tag{C3}$$

First note that with $k_{\parallel} = 0$ the Harris dispersion function is

$$\varepsilon(\omega, k_{\perp}) = 1 + \left(\frac{\omega_p}{\omega_c} \right)^2 \frac{1}{(k\lambda_D)^2} \int_0^{\infty} \frac{\mathcal{Y}_2}{v_{\perp}} \frac{\partial f_0}{\partial v_{\perp}} 2\pi v_{\perp} dv_{\perp}. \tag{C4}$$

Using the identity (C3), and the recurrence relation for $f_{\gamma}(v_{\perp})$ of (3.19), one obtains

$$\int_0^{\infty} \frac{\mathcal{Y}_2}{v_{\perp}} \frac{\partial f_0}{\partial v_{\perp}} 2\pi v_{\perp} dv_{\perp} = {}_2F_2 \left[\begin{matrix} \frac{1}{2}, & \gamma+1 \\ 1+\omega', & 1-\omega' \end{matrix} \right] (-2(k_{\perp}r_L)^2) - {}_2F_2 \left[\begin{matrix} \frac{1}{2}, & \gamma \\ 1+\omega', & 1-\omega' \end{matrix} \right] (-2(k_{\perp}r_L)^2) \tag{C5}$$

which was to be shown.

C.1.1. *Demonstration of (C3)*

Observe that term-by-term multiplication of the power series for both J_{ω} and $J_{-\omega}$, and diagonalization of the double sum with $\ell = m + k$, leads to the expression

$$\frac{\pi\omega}{\sin(\pi\omega)} J_{\omega}(z) J_{-\omega}(z) = \sum_{m=0}^{\infty} \sum_{k=0}^{\infty} \frac{\Gamma(1+\omega)\Gamma(1-\omega)}{\Gamma(m+\omega+1)\Gamma(k-\omega+1)} \frac{(-1)^{m+k}}{m!k!} \left(\frac{z}{2}\right)^{2(m+k)} \tag{C6}$$

$$= \sum_{\ell=0}^{\infty} \left[\sum_{m=0}^{\ell} \frac{\Gamma(1+\omega)\Gamma(1-\omega)}{\Gamma(m+\omega+1)\Gamma(\ell-m-\omega+1)} \frac{1}{m!(\ell-m)!} \right] (-1)^{\ell} \left(\frac{z}{2}\right)^{2\ell} \tag{C7}$$

having used Euler’s reflection formula $\pi z \csc(\pi z) = \Gamma(1+z)\Gamma(1-z)$ with $\Gamma(z)$ the Gamma function. Recall an identity for the rising factorial $(z)_n$ (or Pochhammer symbol),

$$(z)_n = \frac{\Gamma(z+n)}{\Gamma(z)} = (-1)^n \frac{\Gamma(z+1)}{\Gamma(z-n+1)} \tag{C8}$$

as well as Gauss’s hypergeometric summation theorem,

$${}_2F_1 \left[\begin{matrix} a, & b \\ c \end{matrix} \right] (1) = \frac{\Gamma(c)\Gamma(c-a-b)}{\Gamma(c-a)\Gamma(c-b)}, \quad \text{Re}(c) > \text{Re}(a+b). \tag{C9}$$

Application of (C8) and (C9) to (C7) shows that the inner summation becomes

$$\sum_{m=0}^{\ell} \frac{\Gamma(1+\omega)\Gamma(1-\omega)}{\Gamma(m+\omega+1)\Gamma(\ell-m-\omega+1)} \frac{1}{m!(\ell-m)!} = 2^{2\ell} \frac{\left(\frac{1}{2}\right)_{\ell}}{(1+\omega)_{\ell}(1-\omega)_{\ell}} \frac{1}{\ell!}. \tag{C10}$$

Therefore, the function expressed by the Lerche–Newberger theorem is a hypergeometric,

$$\frac{\pi\omega}{\sin(\pi\omega)} J_{\omega}(z) J_{-\omega}(z) = \sum_{\ell=0}^{\infty} \frac{(-1)^{\ell} \left(\frac{1}{2}\right)_{\ell}}{(1+\omega)_{\ell}(1-\omega)_{\ell}} \frac{z^{2\ell}}{\ell!} = {}_1F_2 \left[\begin{matrix} \frac{1}{2} \\ 1+\omega, & 1-\omega \end{matrix} \right] (-z^2). \tag{C11}$$

Now to compute the integral, the power series in (C11) is integrated term-by-term,

$$\begin{aligned} & \frac{1}{2^\gamma \alpha^{2\gamma+2} \Gamma(\gamma + 1)} \int_0^\infty v^{2j+1} e^{-v^2/2\alpha^2} \frac{\pi\omega}{\sin(\pi\omega)} J_\omega(qv) J_{-\omega}(qv) dv \\ &= \frac{1}{2^\gamma \alpha^{2\gamma+2} \Gamma(\gamma + 1)} \int_0^\infty v^{2\gamma+1} e^{-v^2/2\alpha^2} {}_1F_2 \left[1 + \omega, 1 - \omega \right] (-qv)^2 dv \\ &= \sum_{\ell=0}^\infty \frac{(\frac{1}{2})_\ell (\gamma + 1)_\ell}{(1 + \omega)_\ell (1 - \omega)_\ell} \frac{(-2(\alpha q)^2)^\ell}{\ell!} \end{aligned} \tag{C12}$$

as the coefficients reduce to Euler’s integral $\Gamma(1 + z) = \int_0^\infty x^z e^{-x} dx$, establishing (C3).

C.2. The trigonometric form of the dielectric function

The closed form of complex order connects the characteristic frequencies to the theory of special functions. However, presently there are limited practical options to calculate with complex index. For this reason $\varepsilon(\omega, k)$ represented as a trigonometric integral (Tataronis & Crawford 1970a; Vogman *et al.* 2014; Datta *et al.* 2021),

$$\varepsilon(\omega, k) = 1 + \frac{\omega_p^2}{\omega_c^2} \int_0^\pi \frac{\sin(\theta) \sin(\theta\omega)}{\sin(\pi\omega)} \left[\int_0^\infty f_\perp(v) J_0(\lambda(\theta)v) 2\pi v dv \right] d\theta \tag{C13}$$

with $\lambda = 2k \cos(\theta/2)/\omega_c$. The inner integration is a zero-order Hankel transform $\mathcal{H}_0[f(r); k] = \int_0^\infty f(r) J_0(kr) r dr$. The Hankel transform has a Fourier-multiplier property,

$$\mathcal{H}_0[r^{2n} f(r); k] = (-\nabla_k^2)^n \mathcal{H}_0[f(r); k]. \tag{C14}$$

Further, the radial Laplacians of the Gaussian are precisely the Laguerre functions,

$$(\nabla_k^2)^n [\exp(-\alpha^2 k^2/2)] = (-2\alpha^2)^n L_n(\alpha^2 k^2/2) \exp(-\alpha^2 k^2/2). \tag{C15}$$

Therefore, the Hankel transform of $f_\gamma(v)$ is the family of polar Hermite functions

$$\mathcal{H}_0[f_\gamma(v); q] = L_\gamma \left(\frac{\alpha^2 q^2}{2} \right) \exp \left(-\frac{\alpha^2 q^2}{2} \right). \tag{C16}$$

Substitution of (C16) into (C13) gives (3.26), as was to be shown.

Appendix D. Magnetic potential well of the Weibel instability

The concept of a potential energy well is familiar to every physicist, and essential, among other things, to understanding nonlinear phase space dynamics. Unfortunately, the companion concept of potential momentum has been neglected historically due to confusing issues which arose in the development of electromagnetic and relativistic theory, and this has hindered an analogous understanding of magnetic trapping as a potential momentum well. The conceptual consistency of potential momentum is reviewed positively in Griffiths (2012, § III). Fortunately, simple magnetic trapping in a potential momentum well is reducible to an effective potential energy in a lower-dimensional phase space. This effective potential is useful to model the collisionless trajectories of any magnetic trap, and is commonly utilized to analyse particle beams in magnetic fields (Davidson & Chen 1998; Dodin & Fisch 2006). Here the effective potential method is applied to describe the saturation of Weibel instability.

Ideal magnetic trapping occurs when only magnetic potential \mathcal{A} is present in the laboratory frame. For example, consider the one-dimensional chain of electron holes

formed by magnetic trapping at nonlinear saturation of the Weibel instability of § 4.4. The motion is periodic in the x -direction with a transverse vector potential $\mathbf{A} = A_y(x)\hat{y}$. The two constants of motion for a particle of mass m and charge q are the energy H and the momentum P_y (both of which are fixed by the particle's initial conditions),

$$H = \frac{1}{2}mv_x^2 + \frac{1}{2}mv_y^2, \quad (\text{D1})$$

$$P_y = mv_y + qA_y, \quad (\text{D2})$$

where for simplicity we neglect the second-order electric potential energy associated with the charge density of magnetic trapping in a fixed neutralizing background. The energy consists of only kinetic energy and is constant because the Lorentz force $q\mathbf{v} \times \mathbf{B}$ does no work on the particle. On the other hand, constancy of momentum P_y implies an exchange between kinetic momentum and potential momentum with a change in position. Eliminating v_y between (D1) and (D2) results in

$$H = \frac{1}{2}mv_x^2 + U(x), \quad (\text{D3})$$

representing one-dimensional motion in an effective potential

$$U(x) \equiv \frac{1}{2m}(P_y - qA_y)^2. \quad (\text{D4})$$

In stark contrast to trapping in a potential energy well (for example, $\varphi(x) = \varphi_0 \sin(kx)$), the magnetic well depends on the initial position x_0 and velocity v_{y0} of the charge because the integrable dynamics are characterized by two constants of motion. Indeed, motion is perturbed but not trapped in the direction associated with \mathbf{A} .

To model Weibel instability saturation, take $q = -e$ and $A_y = A_0 \cos(kx)$ of amplitude A_0 and wavenumber k . As a quadratic, the potential $U(x)$ has harmonics at k and $2k$, the self-consistent currents of which generate the harmonic cascade of the saturating instability. The potential takes its extremum when $A_y = A_0$ for any initial position x_0 . Thus, in terms of the parameter $\alpha \equiv mv_{y0}/(eA_0)$ measuring the ratio of kinetic-to-potential momentum, the normalized form of the potential is

$$\frac{U(x)}{U_{\max}} = \frac{(\alpha + \cos(kx))^2}{(|\alpha| + 1)^2} \quad (\text{D5})$$

with $U_{\max} = (m/2)(eA_0/m)^2(|\alpha| + 1)^2$. Around $\alpha = 0$ the second harmonic dominates as $U = U_{\max} \cos^2(kx)$, while with $\alpha \gg 1$ the first harmonic k dominates. Figure 26 illustrates this effect by plotting phase portraits using the normalized Hamiltonian

$$\frac{H}{U_{\max}} = \frac{1}{2} \left(\frac{v_x}{v_0} \right)^2 + \frac{(\alpha + \cos(kx))^2}{(|\alpha| + 1)^2}, \quad (\text{D6})$$

where $v_0 \equiv P_{y,\max}/\sqrt{2}m$ measures the particle's momentum. Equation (D6) bifurcates from a double-well around $\alpha = 0$ to a single-well through $\alpha = 1$, physically indicating trapped trajectories transitioning from closed cyclotron orbits into magnetic bounce orbits. Passing orbits have $H > U_{\max}$, which at approximately $v_y = 0$ occurs for $H > (m/2)(eA_0/m)^2$. In plain words, cyclotron orbits fill the inner well, magnetic bounce orbits fill the outer well, and purely passing trajectories exceed the well barrier altogether. In a

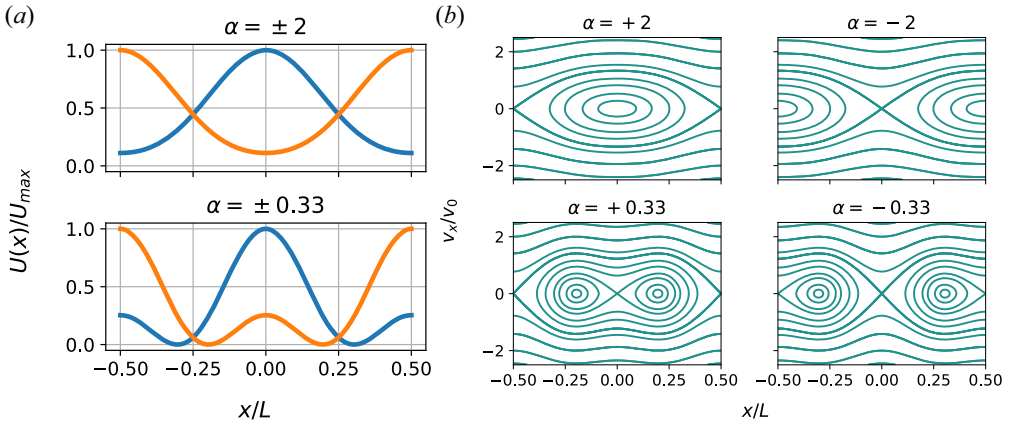


FIGURE 26. (a) Effective potentials of (D5) and (b) phase portraits of trajectories in reduced phase space (x, v_x) associated with motion in the unreduced phase space (x, v_x, v_y) from magnetic trapping in a transverse magnetic vector potential $A_y(x) = A_0 \cos(kx)$. The parameter $\alpha \equiv mv_{y0}/(eA_0)$ measures the ratio of kinetic-to-potential momentum and the v_x -axis is scaled to the transverse momentum P_y of the particle by $v_0 \equiv (1 + |\alpha|)(eA_0/m)/\sqrt{2}$. The opposite side of the phase space across the plane $v_y = 0$ is observed through the inversion $v_{y0} \rightarrow -v_{y0}$ taking $\alpha \rightarrow -\alpha$. The trapping potential bifurcates through $|\alpha| = 1$ from a single-well around $\alpha \rightarrow \infty$ into a double-well around $\alpha = 0$, as trajectories transition from bounce orbits to cyclotron orbits. This transition accomplishes the density filamentation associated with nonlinear magnetic trapping. That is, for $|\alpha| > 1$ inversion exchanges the elliptic and hyperbolic fixed points, but for $|\alpha| < 1$ the elliptic fixed points and their reflection nearly coincide. Thus, for $eA_0 \ll mv_{th}$ the decrease of particles by trapping is exactly balanced by an increase of passing particles of opposite transverse momentum. For this reason the low-amplitude bounce trapping has no associated density perturbation and instead produces a velocity perturbation. However, for $eA_0 \approx mv_{th}$ the near coincidence of the elliptic fixed points with their reflections produces a coherent density perturbation and filamentation. The electron density evolution shown in figure 20 can be understood through this bifurcation in the phase space topology.

fully three-dimensional model, the third component of kinetic energy associated with the z -direction shifts the energy level in the well by an amount $\frac{1}{2}mv_z^2$. Equation (D4) is the main result of this appendix as a conceptual tool to understand the nonlinear phase space dynamics in the saturating Weibel instability.

REFERENCES

- ALLMANN-RAHN, F., LAUTENBACH, S. & GRAUER, R. 2022 An energy conserving Vlasov solver that tolerates coarse velocity space resolutions: simulation of MMS reconnection events. *J. Geophys. Res.* **127** (2), e2021JA029976.
- BALESCU, R. 1997 *Statistical Dynamics: Matter Out of Equilibrium*. World Scientific.
- BARNES, D.C. & CHACÓN, L. 2021 Finite spatial-grid effects in energy-conserving particle-in-cell algorithms. *Comput. Phys. Commun.* **258**, 107560.
- BERNSTEIN, I.B. 1958 Waves in a plasma in a magnetic field. *Phys. Rev.* **109**, 10–21.
- BERTRAND, P. & FEIX, M.R. 1968 Nonlinear electron plasma oscillation: the “water bag model”. *Phys. Lett. A* **28** (1), 68–69.
- BIRDSALL, C.K. & LANGDON, A.B. 1991 *Plasma Physics via Computer Simulation*. Plasma Physics and Fluid Dynamics. Taylor & Francis.
- BOHM, D. & GROSS, E.P. 1949 Theory of plasma oscillations. A. Origin of medium-like behavior. *Phys. Rev.* **75**, 1851–1864.
- BOYD, J.P. 2001 *Chebyshev and Fourier Spectral Methods*. Courier Corporation.

- BRATANOV, V., JENKO, F., HATCH, D. & BRUNNER, S. 2013 Aspects of linear Landau damping in discretized systems. *Phys. Plasmas* **20** (2), 022108.
- CAGAS, P., HAKIM, A., SCALES, W. & SRINIVASAN, B. 2017 Nonlinear saturation of the Weibel instability. *Phys. Plasmas* **24** (11), 112116.
- CALIFANO, F., PEGORARO, F. & BULANOV, S.V. 1997 Spatial structure and time evolution of the Weibel instability in collisionless inhomogeneous plasmas. *Phys. Rev. E* **56**, 963–969.
- CASE, K. 1959 Plasma oscillations. *Ann. Phys.* **7** (3), 349–364.
- CHE, H. 2016 Electron two-stream instability and its application in solar and heliophysics. *Mod. Phys. Lett. A* **31** (19), 1630018.
- CHENG, C.Z. & KNORR, G. 1976 The integration of the Vlasov equation in configuration space. *J. Comput. Phys.* **22** (3), 330–351.
- CHOI, B., CHRISTLIEB, A. & WANG, Y. 2021 High-dimensional sparse Fourier algorithms. *Numer. Algorithms* **87**, 161–186.
- CONNER, J.W. & WILSON, H.R. 1994 Survey of theories of anomalous transport. *Plasma Phys. Control. Fusion* **36** (5), 719.
- CREWS, D.W. 2022 Numerical simulation of collisionless kinetic plasma turbulence. PhD thesis, University of Washington.
- CREWS, D.W., DATTA, I.A.M., MEIER, E.T. & SHUMLAK, U. 2024 The Kadomtsev pinch revisited for sheared-flow-stabilized Z-pinch modeling. *IEEE Trans. Plasma Sci.*, 1–13. doi:10.1109/TPS.2024.3383312
- CREWS, D.W. & SHUMLAK, U. 2022 On the validity of quasilinear theory applied to the electron bump-on-tail instability. *Phys. Plasmas* **29** (4), 043902.
- DATTA, I.A.M., CREWS, D.W. & SHUMLAK, U. 2021 Electromagnetic extension of the Dory–Guest–Harris instability as a benchmark for Vlasov–Maxwell continuum kinetic simulations of magnetized plasmas. *Phys. Plasmas* **28** (7), 072112.
- DATTA, I.A.M. & SHUMLAK, U. 2023 Computationally efficient high-fidelity plasma simulations by coupling multi-species kinetic and multi-fluid models on decomposed domains. *J. Comput. Phys.* **483**, 112073.
- DAVIDSON, R.C. & CHEN, C. 1998 Kinetic description of high intensity beam propagation through a periodic focusing field based on the nonlinear Vlasov–Maxwell equations. *Part. Accel.* **59**, 175–250.
- DAVIDSON, R.C., HAMMER, D.A., HABER, I. & WAGNER, C.E. 1972 Nonlinear development of electromagnetic instabilities in anisotropic plasmas. *Phys. Fluids* **15** (2), 317–333.
- DEL SARTO, D. & PEGORARO, F. 2017 Shear-induced pressure anisotropization and correlation with fluid vorticity in a low collisionality plasma. *Mon. Not. R. Astron. Soc.* **475** (1), 181–192.
- DODIN, I.Y. 2022 Quasilinear theory for inhomogeneous plasma. *J. Plasma Phys.* **88** (4), 905880407.
- DODIN, I.Y. & FISCH, N.J. 2006 Correction to the Alfvén–Lawson criterion for relativistic electron beams. *Phys. Plasmas* **13** (10), 103104.
- DORY, R.A., GUEST, G.E. & HARRIS, E.G. 1965 Unstable electrostatic plasma waves propagating perpendicular to a magnetic field. *Phys. Rev. Lett.* **14**, 131–133.
- DRUMMOND, W.E. & ROSENBLUTH, M.N. 1962 Anomalous diffusion arising from microinstabilities in a plasma. *Phys. Fluids* **5** (12), 1507–1513.
- DYABILIN, K.S. & RAZUMOVA, K.A. 2015 Thermodynamic approach to the interpretation of self-consistent pressure profiles in a tokamak. *Plasma Phys. Rep.* **41** (9), 685–695.
- EINKEMMER, L. 2019 A performance comparison of semi-Lagrangian discontinuous Galerkin and spline based Vlasov solvers in four dimensions. *J. Comput. Phys.* **376**, 937–951.
- ESCANDE, D.F. 2016 Contributions of plasma physics to chaos and nonlinear dynamics. *Plasma Phys. Control. Fusion* **58** (11), 113001.
- EWART, R.J., BROWN, A., ADKINS, T. & SCHEKOCIHIN, A.A. 2022 Collisionless relaxation of a Lynden-Bell plasma. *J. Plasma Phys.* **88** (5), 925880501.
- FOX, W., FIKSEL, G., BHATTACHARJEE, A., CHANG, P.-Y., GERMASCHEWSKI, K., HU, S.X. & NILSON, P.M. 2013 Filamentation instability of counterstreaming laser-driven plasmas. *Phys. Rev. Lett.* **111**, 225002.
- FRIED, B.D. & CONTE, S.D. 1961 *The Plasma Dispersion Function: The Hilbert Transform of the Gaussian*. Academic Press.

- GLASSER, A.S. & QIN, H. 2020 The geometric theory of charge conservation in particle-in-cell simulations. *J. Plasma Phys.* **86** (3), 835860303.
- GRADSHTEYN, I.S. & RYZHIK, I.M. 2015 *Table of Integrals, Series, and Products*, 6th edn. Academic Press.
- GRIFFITHS, D.J. 2012 Resource letter EM-1: electromagnetic momentum. *Am. J. Phys.* **80** (1), 7–18.
- GURNETT, D.A. & BHATTACHARJEE, A. 2017 *Introduction to Plasma Physics: With Space, Laboratory and Astrophysical Applications*. Cambridge University Press.
- HAKIM, A. & JUNO, J. 2020 Alias-free, matrix-free, and quadrature-free discontinuous galerkin algorithms for (plasma) kinetic equations. In *SC20: International Conference for High Performance Computing, Networking, Storage and Analysis*, pp. 1–15. IEEE.
- HEATH, R.E., GAMBA, I.M., MORRISON, P.J. & MICHLER, C. 2012 A discontinuous Galerkin method for the Vlasov–Poisson system. *J. Comput. Phys.* **231** (4), 1140–1174.
- HENINGER, J.M. & MORRISON, P.J. 2018 An integral transform technique for kinetic systems with collisions. *Phys. Plasmas* **25** (8), 082118.
- HESTHAVEN, J.S. & WARBURTON, T. 2007 *Nodal Discontinuous Galerkin Methods: Algorithms, Analysis, and Applications*. Springer Science & Business Media.
- HE, Y., SUN, Y., QIN, H. & LIU, J. 2016 Hamiltonian particle-in-cell methods for Vlasov–Maxwell equations. *Phys. Plasmas* **23** (9), 092108.
- HILL, J.M., KEY, M.H., HATCHETT, S.P. & FREEMAN, R.R. 2005 Beam-Weibel filamentation instability in near-term and fast-ignition experiments. *Phys. Plasmas* **12** (8), 082304.
- HO, A., DATTA, I.A.M. & SHUMLAK, U. 2018 Physics-based-adaptive plasma model for high-fidelity numerical simulations. *Front. Phys.* **6**.
- HOWES, G.G., COWLEY, S.C., DORLAND, W., HAMMETT, G.W., QUATAERT, E. & SCHEKOCIHIN, A.A. 2006 Astrophysical gyrokinetics: basic equations and linear theory. *Astrophys. J.* **651** (1), 590.
- HOWES, G.G., TENBARGE, J.M., DORLAND, W., QUATAERT, E., SCHEKOCIHIN, A.A., NUMATA, R. & TATSUNO, T. 2011 Gyrokinetic simulations of solar wind turbulence from ion to electron scales. *Phys. Rev. Lett.* **107**, 035004.
- HUNTINGTON, C.M., *et al.* 2015 Observation of magnetic field generation via the Weibel instability in interpenetrating plasma flows. *Nat. Phys.* **11** (2), 173–176.
- HUTCHINSON, I.H. 2020 Particle trapping in axisymmetric electron holes. *J. Geophys. Res.* **125** (8), e2020JA028093.
- HUTCHINSON, I.H. 2021 Synthetic multidimensional plasma electron hole equilibria. *Phys. Plasmas* **28** (6), 062306.
- ICHIMARU, S. 1992 *Statistical Plasma Physics, Volume I: Basic Principles*. CRC Press.
- JUNO, J., HAKIM, A., TENBARGE, J., SHI, E. & DORLAND, W. 2018 Discontinuous Galerkin algorithms for fully kinetic plasmas. *J. Comput. Phys.* **353**, 110–147.
- KEMPF, Y., POKHOTILOV, D., VON ALFTHAN, S., VAIVADS, A., PALMROTH, M. & KOSKINEN, H.E.J. 2013 Wave dispersion in the hybrid-Vlasov model: verification of vlsiator. *Phys. Plasmas* **20** (11), 112114.
- KRAUS, M., KORMANN, K., MORRISON, P. & SONNENDRÜCKER, E. 2017 GEMPIC: geometric electromagnetic particle-in-cell methods. *J. Plasma Phys.* **83** (4), 905830401.
- LANDAU, L.D. 1946 On the vibrations of the electronic plasma. *J. Phys. USSR* **10** (26), 574–586.
- LANDAU, L.D. & LIFSHITZ, E.M. 1946 *Electrodynamics of Continuous Media*. Pergamon Press.
- LENARD, A. & BERNSTEIN, I.B. 1958 Plasma oscillations with diffusion in velocity space. *Phys. Rev.* **112**, 1456–1459.
- LERCHE, I. 1974 A note on summing series of Bessel functions occurring in certain plasma astrophysical situations. *Astrophys. J.* **190**, 165–166.
- LEUBNER, M.P. 2004 Fundamental issues on kappa-distributions in space plasmas and interplanetary proton distributions. *Phys. Plasmas* **11** (4), 1308–1316.
- LEUBNER, M.P. & SCHUPFER, N. 2001 A general kinetic mirror instability criterion for space applications. *J. Geophys. Res.* **106** (A7), 12993–12998.
- LIVADIOTIS, G. & MCCOMAS, D.J. 2023 Entropy defect in thermodynamics. *Sci. Rep.* **13** (1), 9033.
- MACE, R.L. 2004 Generalized electron Bernstein modes in a plasma with a kappa velocity distribution. *Phys. Plasmas* **11** (2), 507–522.

- MACE, R.L. & HELLBERG, M.A. 2009 A new formulation and simplified derivation of the dispersion function for a plasma with a kappa velocity distribution. *Phys. Plasmas* **16** (7), 072113.
- MAHAJAN, S.M. & HAZELTINE, R.D. 2000 Sheared-flow generalization of the Harris sheet. *Phys. Plasmas* **7** (4), 1287–1293.
- MORRISON, P.J. 2000 Hamiltonian description of Vlasov dynamics: action-angle variables for the continuous spectrum. *Transp. Theory Stat. Phys.* **29** (3–5), 397–414.
- MORRISON, P.J. 2017 Structure and structure-preserving algorithms for plasma physics. *Phys. Plasmas* **24** (5), 055502.
- MORRISON, P.J. & PFIRSCH, D. 1992 Dielectric energy versus plasma energy, and Hamiltonian action-angle variables for the Vlasov equation. *Phys. Fluids B* **4** (10), 3038–3057.
- MORSE, R.L. & NIELSON, C.W. 1971 Numerical simulation of the Weibel instability in one and two dimensions. *Phys. Fluids* **14** (4), 830–840.
- MOUHOT, C. & VILLANI, C. 2011 On Landau damping. *Acta Mathematica* **207** (1), 29–201.
- NEWBERGER, B.S. 1982 New sum rule for products of Bessel functions with application to plasma physics. *J. Math. Phys.* **23** (7), 1278–1281.
- NG, C.S., BHATTACHARJEE, A. & SKIFF, F. 1999 Kinetic eigenmodes and discrete spectrum of plasma oscillations in a weakly collisional plasma. *Phys. Rev. Lett.* **83**, 1974–1977.
- NG, C.S., BHATTACHARJEE, A. & SKIFF, F. 2004 Complete spectrum of kinetic eigenmodes for plasma oscillations in a weakly collisional plasma. *Phys. Rev. Lett.* **92**, 065002.
- NG, J., HAKIM, A., JUNO, J. & BHATTACHARJEE, A. 2019 Drift instabilities in thin current sheets using a two-fluid model with pressure tensor effects. *J. Geophys. Res.* **124** (5), 3331–3346.
- NICHOLSON, D.R. 1983 *Introduction to Plasma Theory*. Wiley.
- PALMROTH, M., GANSE, U., PFAU-KEMPF, Y., BATTARBEE, M., TURC, L., BRITO, T., GRANDIN, M., HOILJOKI, S., SANDROOS, A. & VON ALFTHAN, S. 2018 Vlasov methods in space physics and astrophysics. *Liv. Rev. Comput. Astrophys.* **4** (1), 1.
- PAUL, A. & SHARMA, D. 2024 Kinetic instability of whistlers in electron beam-plasma systems. *Phys. Plasmas* **31** (3), 032117.
- PENROSE, O. 1960 Electrostatic instabilities of a uniform non-Maxwellian plasma. *Phys. Fluids* **3** (2), 258–265.
- PERSE, B., KORMANN, K. & SONNENDRÜCKER, E. 2021 Geometric particle-in-cell simulations of the Vlasov–Maxwell system in curvilinear coordinates. *SIAM J. Sci. Comput.* **43** (1), B194–B218.
- PEZZI, O., COZZANI, G., CALIFANO, F., VALENTINI, F., GUARRASI, M., CAMPOREALE, E., BRUNETTI, G., RETINÒ, A. & VELTRI, P. 2019 ViDA: a Vlasov–Darwin solver for plasma physics at electron scales. *J. Plasma Phys.* **85** (5), 905850506.
- PIERRARD, V. & LAZAR, M. 2010 Kappa distributions: theory and applications in space plasmas. *Sol. Phys.* **267** (1), 153–174.
- POKHOTILOV, O.A., SAGDEEV, R.Z., BALIKHIN, M.A. & TREUMANN, R.A. 2004 Mirror instability at finite ion-Larmor radius wavelengths. *J. Geophys. Res.* **109** (A9)..
- POKHOTILOV, O.A., TREUMANN, R.A., SAGDEEV, R.Z., BALIKHIN, M.A., ONISHCHENKO, O.G., PAVLENKO, V.P. & SANDBERG, I. 2002 Linear theory of the mirror instability in non-Maxwellian space plasmas. *J. Geophys. Res.* **107** (A10), SMP 18-1–SMP 18-11.
- ROSENBLUTH, M.N. & POST, R.F. 1965 High-frequency electrostatic plasma instability inherent to “loss-cone” particle distributions. *Phys. Fluids* **8** (3), 547–550.
- ROYTERSHEYN, V. & DELZANNO, G.L. 2018 Spectral approach to plasma kinetic simulations based on hermite decomposition in the velocity space. *Front. Astron. Space Sci.* **5**.
- RUDAKOV, L. & TSYTOVICH, V. 1978 Strong Langmuir turbulence. *Phys. Rep.* **40** (1), 1–73.
- SCHAMEL, H. 2023 Pattern formation in Vlasov–Poisson plasmas beyond Landau caused by the continuous spectra of electron and ion hole equilibria. *Rev. Mod. Plasma Phys.* **7** (1), 11.
- SHARMA, S.R. & BHATNAGAR, T.N. 1976 Wave propagation along an arbitrary direction in a bi-Maxwellian plasma. *Plasma Phys.* **18** (2), 95.
- SHORT, R.W. & SIMON, A. 2002 Damping of perturbations in weakly collisional plasmas. *Phys. Plasmas* **9** (8), 3245–3253.
- SHUKLA, N., VIEIRA, J., MUGGLI, P., SARRI, G., FONSECA, R. & SILVA, L.O. 2018 Conditions for the onset of the current filamentation instability in the laboratory. *J. Plasma Phys.* **84** (3), 905840302.

- SHUMLAK, U., LILLY, R., REDDELL, N., SOUSA, E. & SRINIVASAN, B. 2011 Advanced physics calculations using a multi-fluid plasma model. *Comput. Phys. Commun.* **182** (9), 1767–1770.
- SKOUTNEV, V., HAKIM, A., JUNO, J. & TENBARGE, J.M. 2019 Temperature-dependent saturation of Weibel-type instabilities in counter-streaming plasmas. *Astrophys. J. Lett.* **872** (2), L28.
- TAGGART, K.A., GODREY, B.B., RHOADES, C.E. & IVES, H.C. 1972 Second-order effects in the Weibel instability. *Phys. Rev. Lett.* **29**, 1729–1731.
- TATARONIS, J.A. & CRAWFORD, F.W. 1970a Cyclotron harmonic wave propagation and instabilities. I. Perpendicular propagation. *J. Plasma Phys.* **4** (2), 231–248.
- TATARONIS, J.A. & CRAWFORD, F.W. 1970b Cyclotron harmonic wave propagation and instabilities. II. Oblique propagation. *J. Plasma Phys.* **4** (2), 249–264.
- TZOUFRAS, M., REN, C., TSUNG, F.S., TONGE, J.W., MORI, W.B., FIORE, M., FONSECA, R.A. & SILVA, L.O. 2006 Space-charge effects in the current-filamentation or Weibel instability. *Phys. Rev. Lett.* **96**, 105002.
- VALENTINI, F., TRÁVNÍČEK, P., CALIFANO, F., HELLINGER, P. & MANGENEY, A. 2007 A hybrid-Vlasov model based on the current advance method for the simulation of collisionless magnetized plasma. *J. Comput. Phys.* **225** (1), 753–770.
- VAN KAMPEN, N. 1955 On the theory of stationary waves in plasmas. *Physica* **21** (6), 949–963.
- VASCONEZ, C.L., VALENTINI, F., CAMPOREALE, E. & VELTRI, P. 2014 Vlasov simulations of kinetic Alfvén waves at proton kinetic scales. *Phys. Plasmas* **21** (11), 112107.
- VEDENOV, A.A. 1963 Quasi-linear plasma theory (theory of a weakly turbulent plasma). *J. Nucl. Energy C* **5** (3), 169.
- VENCELS, J., DELZANNO, G.L., MANZINI, G., MARKIDIS, S., PENG, I.B. & ROYTERSHTEYN, V. 2016 SpectralPlasmaSolver: a spectral code for multiscale simulations of collisionless, magnetized plasmas. *J. Phys.: Conf. Ser.* **719** (1), 012022.
- VERNIERO, J.L., HOWES, G.G. & KLEIN, K.G. 2018 Nonlinear energy transfer and current sheet development in localized Alfvén wavepacket collisions in the strong turbulence limit. *J. Plasma Phys.* **84** (1), 905840103.
- VERSCHAREN, D., CHANDRAN, B.D.G., KLEIN, K.G. & QUATAERT, E. 2016 Collisionless isotropization of the solar-wind protons by compressive fluctuations and plasma instabilities. *Astrophys. J.* **831** (2), 128.
- VERSCHAREN, D., CHEN, C.H.K. & WICKS, R.T. 2017 On kinetic slow modes, fluid slow modes, and pressure-balanced structures in the solar wind. *Astrophys. J.* **840** (2), 106.
- VOGMAN, G., SHUMLAK, U. & COLELLA, P. 2018 Conservative fourth-order finite-volume Vlasov–Poisson solver for axisymmetric plasmas in cylindrical phase space coordinates. *J. Comput. Phys.* **373**, 877–899.
- VOGMAN, G.V., COLELLA, P. & SHUMLAK, U. 2014 Dory–Guest–Harris instability as a benchmark for continuum kinetic Vlasov–Poisson simulations of magnetized plasmas. *J. Comput. Phys.* **277**, 101–120.
- WATANABE, T.-H., IDOMURA, Y., MAEYAMA, S., NAKATA, M., SUGAMA, H., NUNAMI, M. & ISHIZAWA, A. 2014 Exploring phase space turbulence in magnetic fusion plasmas. *J. Phys.: Conf. Ser.* **510** (1), 012045.
- WEIBEL, E.S. 1959 Spontaneously growing transverse waves in a plasma due to an anisotropic velocity distribution. *Phys. Rev. Lett.* **2**, 83–84.
- WU, H., VERSCHAREN, D., WICKS, R.T., CHEN, C.H.K., HE, J. & NICOLAOU, G. 2019 The fluid-like and kinetic behavior of kinetic Alfvén turbulence in space plasma. *Astrophys. J.* **870** (2), 106.
- YOON, P.H. 2007 Spontaneous thermal magnetic field fluctuation. *Phys. Plasmas* **14** (6), 064504.
- YOON, P.H. & LUI, A.T.Y. 2006 Quasi-linear theory of anomalous resistivity. *J. Geophys. Res.* **111** (A2).
- ZHAO, J., LEE, L., XIE, H., YAO, Y., WU, D., VOITENKO, Y. & VIVIANE, P. 2022 Quantifying wave–particle interactions in collisionless plasmas: theory and its application to the Alfvén-mode wave. *Astrophys. J.* **930** (1), 95.
- ZHDANKIN, V. 2023 Dimensional measures of generalized entropy. *J. Phys. A* **56** (38), 385002.